LAND AND WATER
www.csiro.au

Environmental Tracers in the Beetaloo Basin

Aquifer and groundwater characterization

Alec Deslandes, Christoph Gerber, Sebastien Lamontagne, Cornelia Wilske, Axel Suckow

November 2019

Cover Photo: Landholder bore with mechanically driven pump and diesel motor – typical setting at landholder sampling sites.

ISBN 978-1-4863-1409-6 (Print)

ISBN 978-1-4863-1410-2 (Online)

Citation

Deslandes, Alec, Gerber, Christoph, Lamontagne, Sebastien, Wilske, Cornelia, Suckow, Axel (2019): Environmental Tracers in the Beetaloo Basin. Aquifer and groundwater characterization. CSIRO, Australia.

Copyright

Important disclaimer

Contents

Figures

Tables

Acknowledgments

This report was supported by the Gas Industry Social and Environmental Research Alliance (GISERA). GISERA is a collaboration between CSIRO, Commonwealth and state governments and industry established to undertake publicly-reported independent research. The purpose of GISERA is to provide quality assured scientific research and information to communities living in gas development regions focusing on social and environmental topics including: groundwater and surface water, biodiversity, land management, the marine environment, and socio-economic impacts. The governance structure for GISERA is designed to provide for and protect research independence and transparency of research. Visit gisera.csiro.au for more information about GISERA's governance structure, projects and research findings.

We gratefully acknowledge Dave Armstrong on behalf of Pangaea Resources, Robert Wear on behalf of Origin Energy and Simon Fulton on behalf of Santos who provided logistical and field support for the CSIRO field researchers. We also acknowledge the NT Department of Primary Industry and Resources for help with organisation and guidance for the survey.

The authors would like to acknowledge Alf Larcher, Praveen Rachakonda and Paul Wilkes for organization of the field work. Phil Davies assisted with desktop identification, mapping and down-selection of bores from different databases. Alf Larcher and Charles Heath were the field team sampling for geochemical compounds, including hydrocarbons.

We also thank Dirk Mallants, Punjehl Crane and Rohan Glover who provided very valuable and constructive internal reviews.

Executive summary

The Cambrian Limestone Aquifer (CLA) in the Beetaloo Sub-basin (NT) is the main water supply for domestic use and pastoral agriculture and provides baseflow to unique environmental assets at headwaters of local rivers. The CLA, whose recharge has not been quantified to date, is a complex system and highly at risk because it is karstic and only partially confined. A preliminary groundwater study was conducted by CSIRO in 2017, sampling 8 bores for a range of environmental tracers. The results provided valuable insight into the groundwater flow system but highlighted some system complexities and raised important questions about recharge mechanisms, recharge location and possible flow from deeper aquifers along fractures that could not be answered within the limited sample size (Suckow *et al.* 2018).

- New environmental tracer data for the Cambrian Limestone Aquifer (CLA) in the Beetaloo Sub-basin (NT) were obtained and existing data re-evaluated.
- Several combinations of tracer data from the present and earlier studies show anomalous behaviour, some contradicting each other, requiring a revisit of traditional hydrogeological concepts.
- Tracer data can be reconciled with a complex conceptual model of local recharge through sinkholes and simultaneous gas exchange over the entire area caused by groundwater level fluctuations.
- Only tritium is a reliable indicator of groundwater recharge through sinkholes.
- The entire area of the CLA must be regarded as having potential recharge features such as sinkholes and thus is at risk to surface contamination.
- It is recommended to test this conceptualisation by measuring a gas tracer sensitive to time scales of centuries that is not affected by excess air (^{39}Ar).

Field work for the present study was conducted by CSIRO's Gas Industry Social and Environmental Alliance (GISERA) from 18/10/2018 to 03/11/2018 and collected samples from 25 bores within the CLA. Bores were located on transects from the latitude of Daly Waters, towards the latitude of Mataranka, both west and east of the Stuart Highway. Environmental tracer sampling was conducted alongside the sampling for chemical baselining (Wilkes *et al.* 2019). Sampling could not occur along the ideal hypothesised flow paths due to lack of accessibility and suitability of bores for tracer sampling (known screens needed to be in the target formations) and other challenges related to undertaking such studies in remote locations. The tracers sampled included major ions, Rare Earth Elements (REE), the stable isotopes of water, tritium (^{3}H), chlorofluorocarbons (CFC-11, CFC-12, CFC-113), sulphur-hexafluoride (SF_6), halon-1301 (H1301), radiocarbon (^{14}C & ^{13}C), and noble gases (He, Ne, Ar, Kr, Xe, ^{222}Rn).

This study confirmed and emphasized the counter-intuitive tracer patterns and internal contradictions between different tracer types, which were encountered during the first study, however now with a much larger sample set across a larger study area. Examples of these patterns are:

- ^{14}C increased along the flow path, instead of decreasing due to radioactive decay. This indicates groundwater recharge along the flow path.
- Presence of gas tracers like CFCs, SF_6 and H1301 in all samples indicates a significant contribution of modern water (infiltrated after 1950, i.e. during the last 60-70 years) whereas presence of tritium indicates infiltration after 1963 occurred only a small fraction of samples (9 out of 33).

- Heavy noble gases show high infiltration temperatures (30°C-42°C) but with unusual patterns of the noble gases such as excess in argon and dissolved nitrogen.
- Helium is elevated in nearly all samples in some samples up to 500 times above solubility equilibrium; excess helium, if it were produced in situ, is detectable only after a few centuries and is therefore in contradiction to the results from the anthropogenic gas tracers, indicating an influx of old water from deeper formations.

It was possible to reconcile many of the face value contradictions of the tracer patterns with a new conceptual model for the infiltration mechanism. According to this model:

- Significant infiltration and recharge is highly localized through sinkholes and happens only during the heavy rain events of the monsoon season.
- This localized recharge transports tritium only locally to the groundwater, since tritium is part of the water molecule (HTO).
- This local infiltration raises the water table in the entire area by several meters, which entraps gas bubbles in the unsaturated zone creating comparably large excess air and "pumps" the gas tracers into groundwater. This explains the observed pattern of modern gas tracers (CFCs, SF_6, H1301) while tritium is mostly absent.
- Between the recharge events, gas tracer species with high diffusivity (such as helium and neon) can partly re-equilibrate, whereas gas tracers with low diffusivity (such as SF_6, H1301, Kr and Xe) stay enriched above solubility equilibrium.

While this new conceptual model explains the tracer results in a qualitative way, a quantitative (numerical) model of these processes is beyond the scope of the present study. The conceptual model also suggests that the conventional gas tracers (CFCs, SF_6, H1301) are not reliable indicators of recharge in this area, since they are overprinted by excess air and gas exchange processes. A future study is needed to clarify whether gas tracers that are not sensitive to excess air, such as ^{85}Kr and ^{39}Ar, can further constrain the timing of recharge and gas exchange. The present study is the first attempt to quantify recharge in those areas where it is confirmed, using tritium.

A consequence of this conceptualisation is that the whole area of the CLA must be regarded as potential recharge area. Together with the very high flow velocities typical for a karst aquifer this implies that the whole area of the CLA is at potential risk to possible contamination from surface spills from any source. The magnitude of this risk is dependent on a range of factors including probability of a spill occurring, containment, removal and rehabilitation at the spill site; degradation/adsorption of residual chemicals in the soil by microflora; dilution of residual chemicals by large flow volumes during the monsoon; and further degradation of chemicals in the aquifer itself.

Open questions from this study are:

- What exactly is the source of elevated helium in the CLA (localized fractures or a general flux of helium from underlying formations)? How much water flow does this helium flux represent? This question can only be answered once the helium concentration in pore water and groundwater of deeper formations is measured. This requires new drilling of monitoring wells to greater depth than what is currently available.

- Is the increasing ^{14}C concentration along the flow path only due to increasing gas exchange, assuming modern CO_2 from root respiration is “pumped” into the groundwater as dissolved total inorganic carbon (TDIC)? Or is a significant fraction of the modern ^{14}C the result of infiltration on a larger time scale than represented by tritium (centuries)? To answer this question, measurements of a tracer in the intermediate time scale (^{39}Ar) are necessary.

1 Introduction

Shale gas is a considerable opportunity to secure a vast energy resource for Australia into the future. The Beetaloo Sub-Basin, southeast of Darwin, hosts the Velkerri Shale, which is considered to be one of the largest shale gas reservoirs in Australia (Cox and Collins 2017). Unlike coal seam gas production where only 6% of the nearly 10,000 CSG wells (3000 exploration/pilot/ appraisal wells and 7000 production wells) drilled in the Bowen and Surat basins in Queensland have received hydraulic fracturing (Mallants *et al.* 2018), the process of extracting gas from shale and tight gas reservoirs necessitates hydraulic stimulation of the low permeability, gas-bearing strata by hydraulic fracturing ("fracking") (Cook *et al.* 2013). Experience in shale and tight gas extraction in other countries, particularly in North America, has shown that the process of fracking needs large amounts of water and that it is one of the most critical parts for the companies involved in obtaining the social licence to operate their business (Smith and Richards 2015). The discussion in public, academia and industry ranges from the competition for water, over possible surface spills of either fracking fluids or other industry fluids that could potentially contaminate shallow aquifers, up to fracturing-induced earthquakes which could reactivate geological faults able to migrate fluids from deep groundwater into shallow groundwater systems. The issues described in "The Scientific Inquiry into Hydraulic Fracturing in the Northern Territory" (NT 2018) capture many of these concerns shared by Australian communities. The Scientific Inquiry also formulates many recommendations for governments, regulators and resource companies on how to manage the risks related to shale gas development. Specifically, Recommendation 7.5, "The regional assessment should focus on surface and groundwater quality and quantity (recharge and flow)", is about collecting baseline information to assess post-development impacts and to generate new knowledge to inform regional planning (NT 2018).

In the Beetaloo Basin, the companies Origin, Santos and Pangaea hold leases for the exploration of the Velkerri Shale. Origin has developed a comprehensive groundwater monitoring programme to understand the baseline groundwater conditions in their permit areas; they have also undertaken a comprehensive desktop study of the hydrogeology (Fulton and Knapton 2015). Understanding both the possible groundwater impacts from using large amounts of water for drilling and fracking needs a thorough understanding of the source aquifer. Assessing the risks and possible impacts from surface contamination needs a thorough understanding of the characteristics of aquifers closest to the surface. In the Beetaloo Sub-Basin, the Cambrian Limestone Aquifer (CLA) is both a water source for drilling and fracturing fluids and a receptor in case of surface contamination. The CLA can be subdivided into the Gum Ridge Formation and the Anthony Lagoon Beds; it forms the principal water resource in the Beetaloo Sub-Basin (Tickell 2003, 2004; Fulton and Knapton 2015; Tickell 2016). The CLA is a karst aquifer, consisting of fractured and cavernous limestones (Fulton and Knapton 2015). Recharge mechanisms are poorly characterised but in karst aquifers are likely to be dominated by recharge through sinkholes and preferential recharge through macro-pores (Stevanović 2015). Very preliminary recharge estimates indicated that the water needed for hydraulic fracturing on the Origin tenements represents 1% of the available water resource, with another 6% from existing groundwater use (Fulton and Knapton 2015). Little is known about the flow velocity of groundwater in the CLA and although there are indications that vertical groundwater gradients point upwards, and therefore may enable a flux from the underlying Roper Group into the CLA (Fulton and Knapton 2015), observational evidence for such a flux is lacking.

The present report builds on a first preliminary assessment (Suckow *et al.* 2018) which had evaluated the existing environmental tracer measurements (Tickell 2003, 2004, 2016) and complemented them with new measurements, including for the first time tracers for "young" water. This included tracers such as tritium, SF_6, Halon 1301 and the noble gases, which allow to assess travel times in the range of decades. The present report presents the most detailed environmental tracer data to date, with 25 new samples that, for the first time, also include CFCs, Rare Earth elements and the isotopes of Sulphate $^{34}S(SO_4)$ & $^{18}O(SO_4)$.

1.1 Objectives

In the framework of the Beetaloo baseline assessment, the investigation of the geohydrological system is focused on the following aspects (Suckow *et al.* 2018):

- Quantification of the recharge entering the CLA.
- Quantification of the vertical and horizontal flow velocity to assess the effect of any possible contamination of the CLA, and the impact of additional water abstraction for hydraulic fracturing on groundwater dependent ecosystems or other users.
- Improved characterisation of the Tindall limestone aquifer including groundwater flow and aquifer interconnectivity.

The 2018 CSIRO Environmental Tracers report (Suckow *et al.* 2018) investigated the historical data and studied eight new samples taken during the targeted tracer sampling campaign of 2017. The findings highlighted the complexity of the hydrogeological system, and resulted in a range of unresolved issues requiring further investigation with a more data-dense campaign, including:

- Possible systematic variation in recharge rates, increasing from south to north
- Flow system characterisation was limited by data sparsity in the karstic system, and the heterogeneities therein
- Gas tracers indicating 'modern' source of water everywhere in the aquifer, in addition to an older source
- Very large excess air concentrations, for the relatively novel tracers that have to-date limited application in such environments, the extra samplings on this campaign will aid conceptualisation from their results.
- Helium occurrence in wells possibly representing input of "old" groundwater from underlying systems.

Further to these issues, it is important to determine whether tracers can help distinguish whether groundwater is from the Gum Ridge Formation or the Anthony Lagoon Beds. The bores sampled in 2017 were mostly from the Daly and northern-Georgina Basin and did not include the Anthony Lagoon Beds that elsewhere overlay the Gum Ridge Formation/Tindall Limestone. Therefore, the previous data did not provide relevant information to resolve this question and needs further corroboration.

With respect to localised effects upon existing groundwater users, the *Scientific Inquiry into Hydraulic Fracturing in the Northern Territory* in their final report (2018) requires in Recommendation 7.8 that:

'Measures to be mandated to ensure any onshore shale gas development does not cause unacceptable local drawdown of aquifers… relevant water allocation plans (WAPs) include provisions that adequately control both the rate and volume of water extraction and that gas companies be required to monitor drawdown in local water supply bores and immediately rectify any problems if the drawdown is found to be excessive.'

This tracer investigation contributes both to regional groundwater assessments and to a better understanding of drawdown at specific locations by using tracer analysis to parametrise models for likely drawdown or recovery. Specific information derived from tracers that can be very useful in such models, include recharge and mechanisms thereof, and flow velocities.

The companies Origin, Santos and Pangaea hold leases for the exploration of the Velkerri Shale. The characterisation of the CLA provides key information on a possible water source for fracking operations in the shale gas reservoir, and baseline chemical information of this water source as a reference point for future comparisons.

2 Beetaloo Sub-Basin

The Beetaloo Sub-Basin includes the Daly Basin in the North, and the Wiso and Georgina Basins in the South-West and South-East respectively (Figure 2.1). Its vast geographical area and the geological, hydrological and meteorological heterogeneities therein makes targeting, collecting and determining characteristics for a suitable distribution of tracer samples a challenge. Previous geological and hydrological studies have provided important information on the current sampling area; the information that was key to help design the sampling campaign and analyse the new tracer information is summarised below.

- The Cambrian Limestone Aquifer (CLA), extending far beyond the area of the Beetaloo Sub-Basin, is the shallowest aquifer of the area and supplies water for the pastoral industry.
- As a karst aquifer the CLA shows dissolution cavities with very high groundwater flow velocities and probably must be regarded as a dual permeability and dual porosity system.
- Faults and fractures exist in the area and their effect on vertical connectivity is unknown.
- There is a strong north-south gradient in precipitation and vegetation over the extend of the CLA, which points towards much higher recharge in the north.

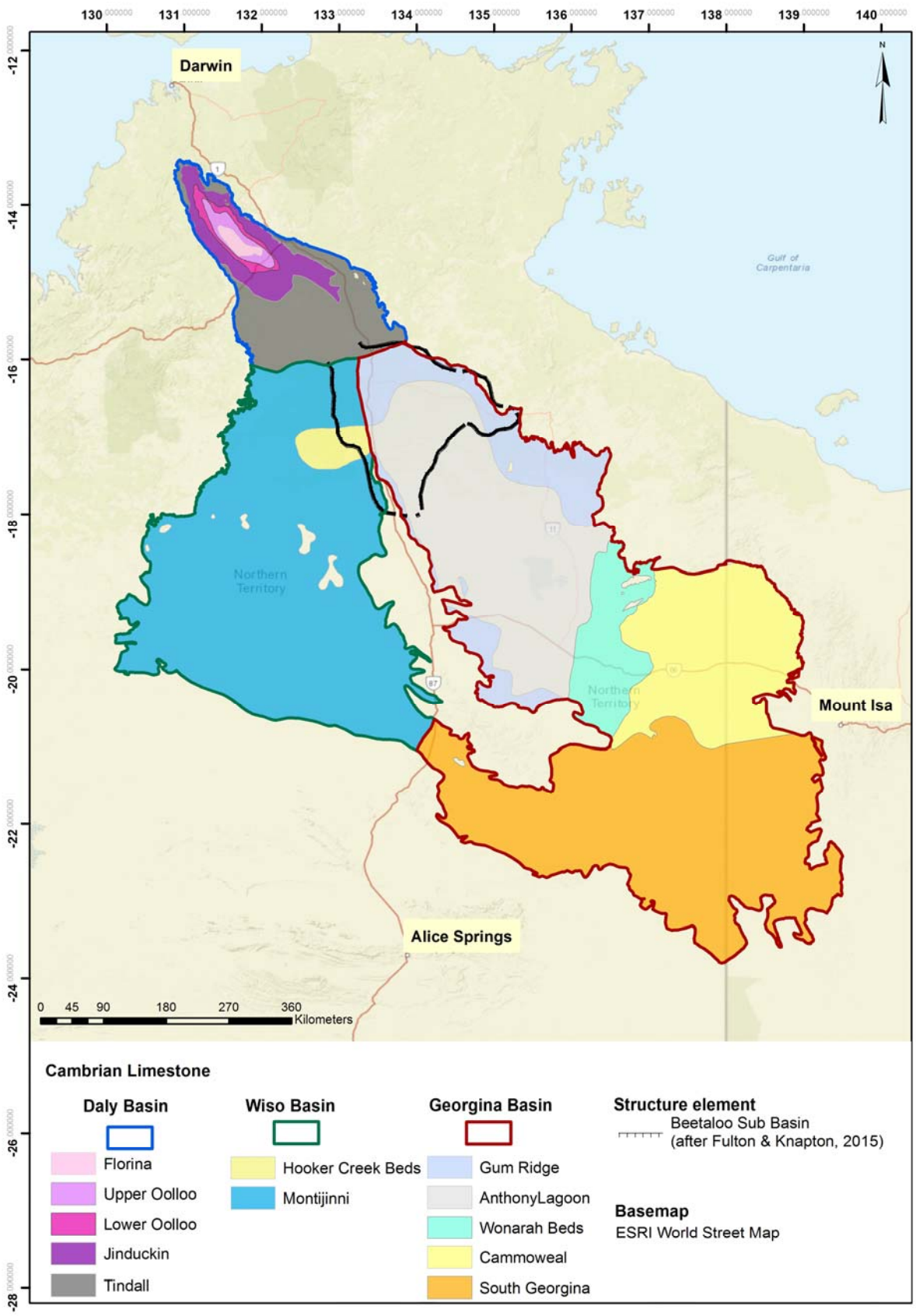

Figure 2.1 Surface geology of the Cambrian Limestone Aquifer including the Beetaloo Sub-basin

2.1 Geological Formations and Structure

The geology across the basin can be summarised with reference to the stratigraphy as shown in Table 1 (Fulton and Knapton 2015). The Velkerri Formation, the target for gas exploration and extraction, lies in the Roper Group. Above this are a series of mudstone and sandstone layers. Above the Roper Group is a set of Cambrian-aged formations, the highest of which is the Cambrian Limestone Aquifer (CLA) that currently provides the principal water resource via bores for the pastoral industry and local communities. Since the Antrim event about 530-510 MA, with its extrusion of the Antrim Plateau and Helen Springs Volcanics through the now-underlying sandstone, the region has been described as having limited tectonic activity, though with some reactivation of older faults (Fulton and Knapton 2015).

Table 1 Stratigraphy for the Beetaloo Sub-Basin (Fulton and Knapton 2015)

PROVINCE	PERIOD / AGE	FORMATION		AQUIFER STATUS	THICKNESS (m)	YIELD (l/s)	AVE. EC (µs/cm)
CARPENTARIA BASIN	CRETACEOUS 145 – 66 Ma	Undifferentiated		*Local Aquifer*	0 - 130	0.3 - 4	1800
GEORGINA BASIN	CAMBRIAN 497-630 Ma	Cambrian Limestone Aquifer (CLA)	Anthony Lagoon Beds	REGIONAL AQUIFER	0 – 200	1 - 10	1600
			Gum Ridge Formation	REGIONAL AQUIFER	0 – 300	0.3 - >20	1400
		Antrim Plateau Volcanics		REGIONAL AQUITARD *Local Aquifer*	0 – 440	0.3 - 5	900
		Bukalara Sandstone		*Local Aquifer*	0 – 75	0.3 - 5	1000
BEETALOO BASIN (ROPER GROUP)	NOT KNOWN	Hayfield Mudstone		REGIONAL AQUITARD *Local Aquifer*	0 – 450	-	32000
		Jamison Sandstone		*Local Aquifer*	0 – 150	-	138000
	MESO-PROTEROZOIC 1430-1500 Ma	Kyalla Formation		REGIONAL AQUITARD	0 – 800	-	-
		Moroak Sandstone		*Local Aquifer*	0 – 500	0.5 - 5	131000
		Velkerri Formation		REGIONAL AQUITARD	700 – 900	-	-
		Bessie Ck Sandstone		*Local Aquifer*	450	0.5 - 5	-

The Cambrian Limestone Aquifer is geographically differentiated into different formations according to its local basin, and within those basins some differences have been observed in the geology. The shallowest layer of the CLA (Anthony Lagoon Beds) does not exist in some areas, particularly in the South of the Daly Basin and much of the West of the Wiso Basin (Figure 2.1), likely due to erosion before the overlaying Cretaceous materials were deposited.

Table 2 Sub stratigraphy of strata in the Cambrian Limestone Aquifer (Yin-Foo and Matthews 2000)

CLA Strata	Daly Basin	Georgina Basin	Wiso Basin
Highest	Jinduckin	Anthony Lagoon Beds	Hooker Creek Beds
Sub	Tindall - massive, thinly bedded, multi-coloured crystalline, dolomitised limestone with some chert nodules and mudstone bands, particularly in the lower layers	Gum Ridge - similarly sequenced to the Tindall Limestone Formation, is generally described as consisting of limestone, fine grained sandstone and siliclastic mudstone and nodular chert, greater proportion of carbonate sediment	Montejinni - limestone, dolomitic limestone, dolomite and calcareous mudstone and siltstone. In many parts of the basin, a threefold division with intervening red/brown mudstone

2.2 Hydrogeology of the Cambrian Limestone Aquifer

The NTG Water Resources Division (WRD) conducted water resource assessments between 1996 and 2009 that mapped the shallow groundwater resources over approximately 95% of the Beetaloo Basin (Yin-Foo and Matthews 2000; Tickell 2003, 2005; Tickell and Bruwer 2017). The Cambrian Limestone Aquifer (CLA) is a karstified aquifer system and consists of different hydrostratigraphic and regional facies such as the Tindall Limestone, the Gum Ridge Formation and the Montejinni Formation. Where it exists as an overlying layer, the Jinduckin Formation, the Anthony Lagoon Beds and the Hooker Creek Beds can locally confine the formations of the Cambrian Limestone Aquifer. This observation is supported by bore hydrographs that show large water level fluctuations in the unconfined part compared to confined areas (Tickell 2005). Sinkholes are prominent karst features where the Tindall is unconfined and are expected to enable direct recharge in these areas. The assumed confinement also points to limited connectivity of these aquifers to surface water and infiltration. On the other hand, in the area of the Daly and Georgina Basins interfacing, Tickell (2005) noted there appears to be more hydraulic connectivity between the Anthony Lagoon Beds and the Gum Ridge Formation, and possibly also horizontally between the Anthony Lagoon Beds and the Tindall Limestone. In the regions of the Gum Ridge and Montejinni Formations, sinkholes are less prevalent. Instead recharge may occur by seepage from seasonal creeks crossing outcrops, particularly at the basin margins. Recharge of the Anthony Lagoon Beds may be via seasonal lakes (Tickell 2003; Tickell and Bruwer 2017).

The local groundwater flow is expected to be linked to the nature of the layers, i.e. the limestone and/or dolomite nature, and its associated karst or cavities. This introduces potential heterogeneities across the aquifers, the degree and impact of which are hard to predict. However, it is worth keeping in mind that these heterogeneities might affect the spatial distribution of environmental tracers to different degrees. Since the locations of sinkholes are not mapped in

detail it is also important to note that the whole area of the CLA is potential recharge area and potentially at risk to contamination from surface spills.

Considering only the stratigraphy, one can observe in cross sections that the base of the CLA is low in the mid-Georgina Basin. The outcrops on the margin assist with recharge, and groundwater levels are too deep to discharge to streams, hence the flow pattern is basin-wards from the margins and then to the north-west into the Daly Basin (Fulton and Knapton 2015). Regional groundwater level contours, based on over 3000 bores across the basin (Rachakonda *et al.* 2018), as well as Shuttle Radar Topographic Mission data (Tickell 2003) have indicated south-east to north-west flows.

The basalt layer of the Antrim Plateau Volcanics is considered to be an effective aquiclude, though in the southern reach (between Dunmarra and Elliot) of the basin the volcanics are absent and the Gum Ridge Formation directly overlies the Roper Group (Fulton and Knapton 2015).

2.3 Faults

The Tennant Creek Inlier is a bedrock high separating the Wiso and Georgina Basins, and extends northwards beneath the Daly Basin. It runs just to the west of – and parallel to – the Stuart Highway. Around this inlier are significant drop downs in the CLA, which are the mostly likely place for faults that might influence local groundwater, i.e. by providing connectivity through underlying basalt or other aquicludes. The Birdum Creek Fault, to the east of the bedrock high, has a 200 m displacement at Larrimah (Yin-Foo and Matthews 2000).

In the Roper Group, which is the series of sandstone and mudstone layers below the CLA and the underlying volcanics, are a series of faults that were activated and re-activated during periods between 2000 – 1324 Ma (Fulton and Knapton 2015). It has been posited that the structures of the lower Roper Group do not penetrate the Hayfield Mudstone (Silverman *et al.* 2007).

2.4 Recharge and Discharge

Recharge in the study area occurs when rainfall intensity and duration are sufficient to overcome evapotranspiration (ET) and where aquifers are unconfined (Fulton and Knapton 2015). Four mechanisms were outlined: direct recharge, channelling through macro-pores, localised indirect recharge into sinkholes and indirect recharge along ephemeral drainage in the arid southern region. The last two of these mechanisms are poorly understood. Direct recharge can be defined as precipitation infiltrating through the unsaturated zone. Some literature has defined concentrated recharge such as might be expected via sinkholes to rather be distinguished as *localized*, whereas *indirect recharge* is focussed by external water resources or surface features such as rivers or lakes (Healy 2010).

Large seasonal rain events lead to run-off in streams and lakes, and recharge of the aquifers can occur where this rain crosses outcropping formations. Infiltration of standing water, e.g. that in the seasonal shallow lakes, is possible for the Anthony Lagoon Beds in the region of the Barkly Tablelands (Tickell and Bruwer 2017). The Gum Ridge is thought to recharge from seasonal creeks where they cross outcrops (Tickell and Bruwer 2017).

In the Tindall, hydrographs show water level variation up to 7 m seasonally with the wet season in unconfined areas, whereas variation was 2-3 m from areas with a covering of cretaceous rocks (Tickell 2005). In the Georgina Basin, comparison of hydrographs and five-year moving averages for rainfall led to the conclusion that significant recharge events occur infrequently, separated by decades during which little recharge occurs (Tickell and Bruwer 2017).

Recharge of the CLA in the Georgina basin was estimated to be 0.4-0.8 mm/y (Fulton and Knapton 2015). In the southern Georgina Basin recharge was estimated to be between 2 and 6 mm/y (Fulton and Knapton 2015), 1 mm/y in the Barkley Tablelands (Tickell 2003) and 0.8-12.2 mm/y (Tickell and Bruwer 2017).

The Roper River and springs such as those found at Mataranka and Helen Springs are the main perennial outflow areas of the CLA (Karp 2008). Decadal changes of groundwater discharge to the Roper River suggest most of the recharge input is relatively close to the discharge area (Fulton and Knapton 2015). In a karst aquifer, however, this argument encompasses a very large region, since pressure propagates very quickly through karst.

Known discharge outlets include springs that drain into the Roper River at Mataranka in the north, and springs draining into Lawn Hill Creek and the Gregory River in Queensland to the east. The Roper River exhibits perennial flows that during the dry season has baseflows of 95-12.6 GL/y supplied by groundwater (Fulton and Knapton 2015).

2.5 Climate

The climate varies from in the North about Katherine being dry tropical savanna, to warm desert in the South near Tennant Creek. Most rainfall originates from monsoonal systems that approach from the north. The rainfall varies across the basin as summarised in Table 3 and Figure 2.2 (http://www.bom.gov.au/climate/).

Table 3 Mean annual rainfall for Beetaloo Sub-Basin along a North-South transect from Katherine (North) to Tennant Creek Airport (South).

LOCATION	RECORD PERIOD	MM/YEAR
Katherine	1873-2019	970
Larrimah	1952-2019	860
Daly Waters	1873-2013	673
Elliot	1949-2019	597
Helen Springs	1954-2016	454
Tennant Creek Airport	1969-2019	473

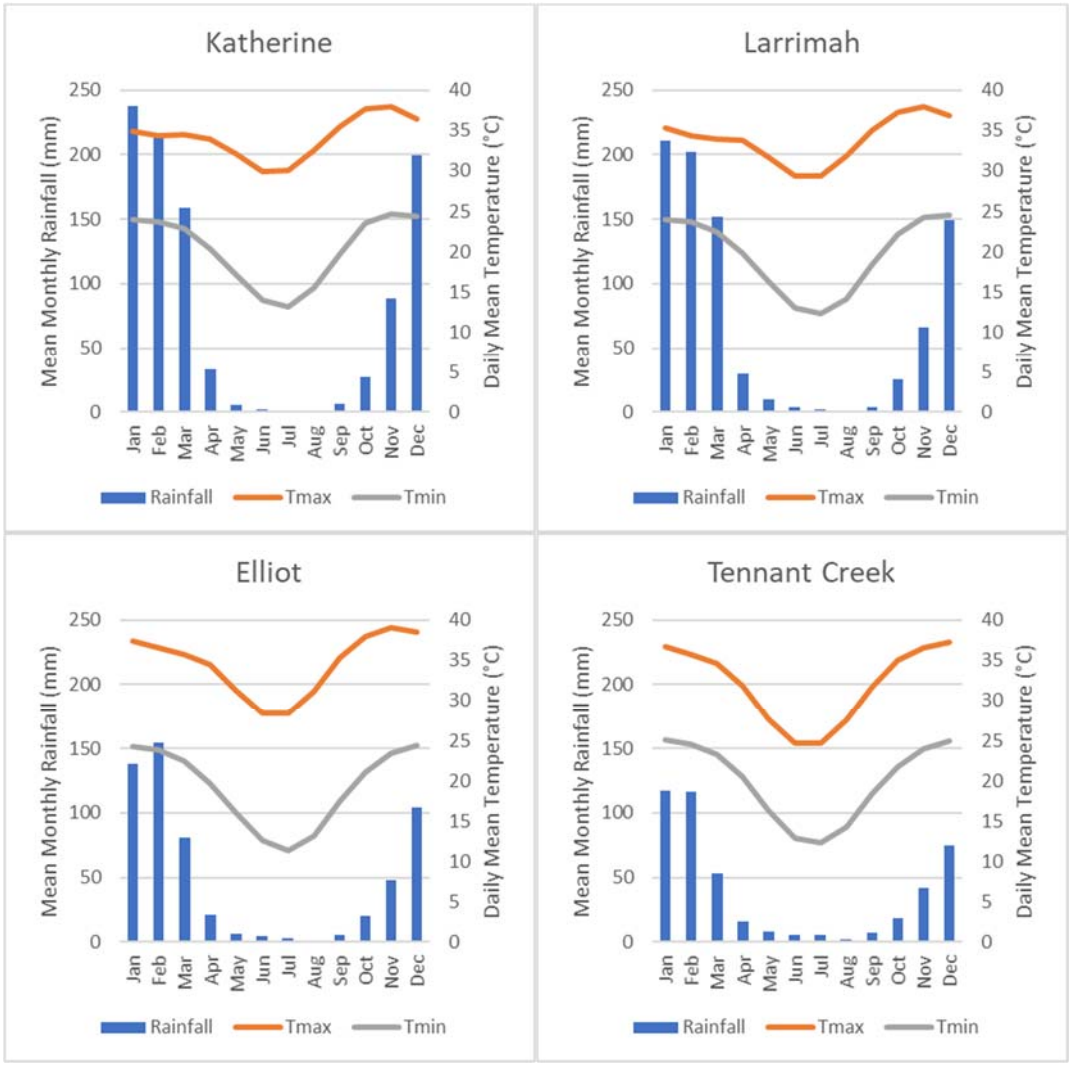

Figure 2.2 Monthly climate statistics for locations North-South across the Beetaloo Sub-basin

3 Applied methods

3.1 Bore selection

Of the few thousand bores available across the study area, selection was undertaken using bore report information, including final depth and bore log strata, and prioritising those bores with discrete screens indicated to be in formations of interest (Figure 2.2, Figure 3.1 and Table 4). In the south of the study area the limestone layers are quite thick and deep, with the bores mostly in the Gum Ridge or Anthony Lagoon Beds, or the equivalents in neighbouring basins. One bore at Helen Springs, thought to be a key area of recharge for the CLA, was in the overlaying Proterozoic Sandstone. In the NW of the study area, bores were mostly in the areas where the Tindall was not overlain by the confining Jinduckin layer. Bore logs indicated some were screened in basalt, i.e. the Antrim volcanics below the CLA Limestone. One of these bores (RN031397) reportedly is cased into the basalt at 62 m but is open hole down to 229 m and thereby also penetrates 8 m deeper into sandstone below the basalt, so waters drawn from here may have some Bukalara Sandstone component.

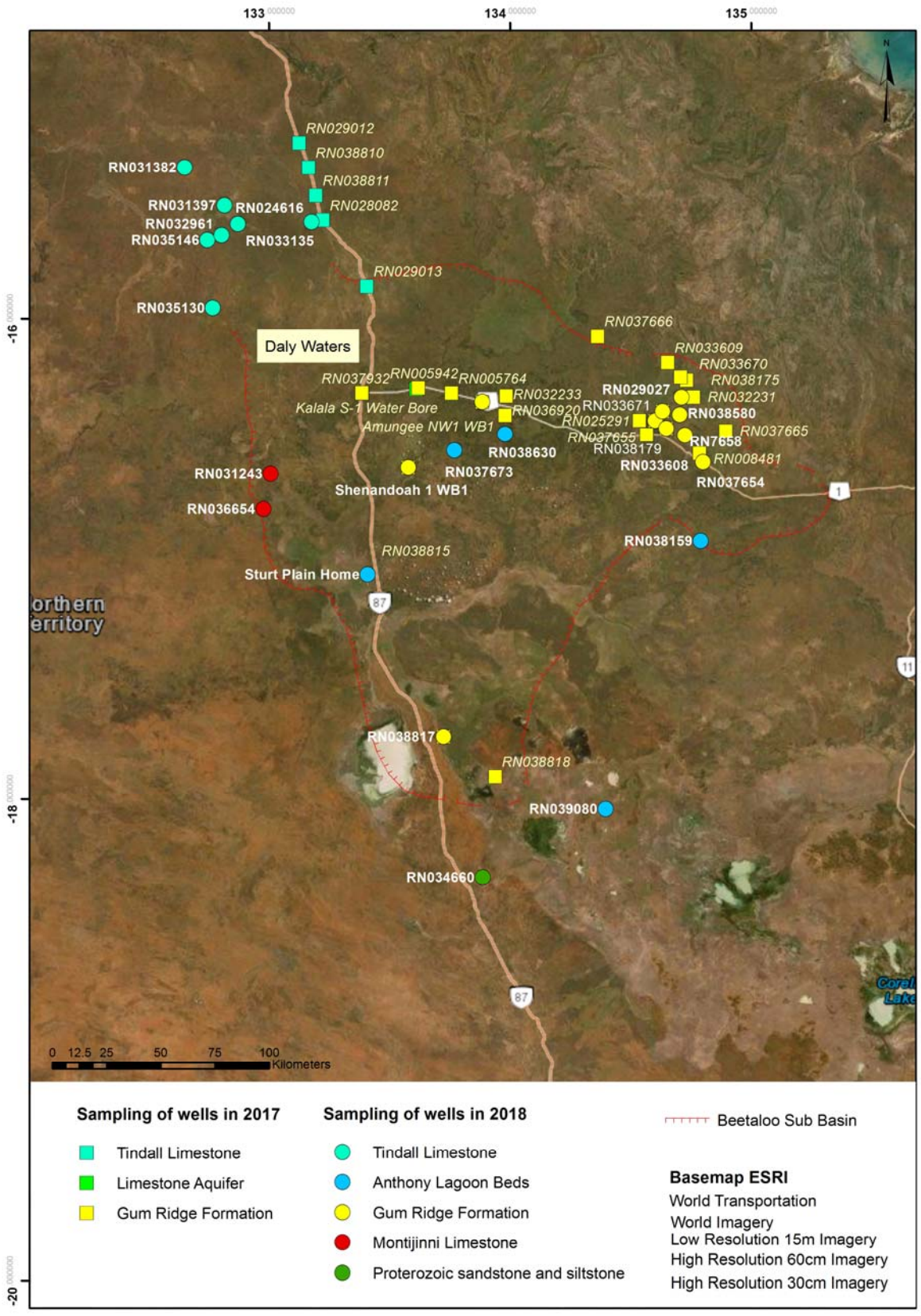

Figure 3.1 Locations of tracer sampling points and the sampled formation.

Table 4 Sampled wells including aquifer information.

Sampling ID	Sampling Name	External ID	Sampling Date	Final Depth	Top of Screen	Bottom of Screen	Geology	Strata from Borelogs
9769	RN31382	RN031382	18-Oct-18	80.6	73.4	79.9	Tindall Limestone	Basalt, above siltstone
9770	Cow Creek house bore	RN033135	18-Oct-18	52.5	40.99	43	Tindall Limestone	Basalt, above limestone and chert, clay stone
9771	Scrubby RN 31397	RN031397	18-Oct-18	229.1	61.8	229.1	Tindall Limestone	Sandstone, above Basalt and Chert/Limestone
9772	Ribone	RN035130	19-Oct-18	93	80	93	Tindall Limestone	Basalt, above Limestone
9773	Tarlee House	RN035146	19-Oct-18	69	57	69	Tindall Limestone	Limestone
9774	Tarlee Road	RN032961	19-Oct-18	120	54	114	Tindall Limestone	does not say, above Limestone
9775	Birdum Creek	RN024616	19-Oct-18	81.6	76	80	Tindall Limestone	Basalt, above Dolomite
9776	Taskers bore	RN038179	24-Oct-18	155	143	155	Gum Ridge Formation	Limestone
9777	Number 17	RN033671	24-Oct-18	114	102	108	Gum Ridge Formation	Sandstone, above shale
9778	RN029027	RN029027	24-Oct-18	98	75	84	Gum Ridge Formation	grey clay, some limestone bands
9779	RN7658	RN007658	24-Oct-18	94.4	82.3	88.4	Gum Ridge Formation	Limestone, above gravel and black sandy clay (Tindall)
9780	RN038159	RN038159	25-Oct-18	155	146	155	Anthony Lagoon Beds	Limestone
9781	RN037654	RN037654	25-Oct-18	155	143	155	Gum Ridge Formation	Limestone/ Dolomite, above brown black clay
9782	RN038580	RN038580	26-Oct-18	120	84	96	Gum Ridge Formation	does not say,above Limestone and on top soft black shale
9783	RN033608	RN033608	26-Oct-18	156	138	156	Gum Ridge Formation	Sandstone, Chalk brown clay
9784	XXXX	RN036654	27-Oct-18	106	99.5	106	Montijinni Limestone	Broken Limestone (above sand-sandstone)
9785	Wendy	RN031243	27-Oct-18	156	137	141.5	Montijinni Limestone	does not say, above Gravel
9786	Container bore	RN038630	30-Oct-18	146.54	140.54	146.54	Anthony Lagoon Beds	does not say what is below, above Clay
9787	Amungee NW1	No external ID	30-Oct-18				Gum Ridge Formation	
9788	Shenandoah 1 WB1	No external ID	01-Nov-18				Gum Ridge Formation	
9789	Vanderlin	RN037673	01-Nov-18	141	136	139	Anthony Lagoon Beds	Limestone
9790	Sturt Plain Home	No external ID	01-Nov-18				Anthony Lagoon Beds	
9791	RN034660	RN034660	02-Nov-18	180	48	162	Proterozoic sandstone and siltstone	Sandstone
9792	RN039080	RN039080	02-Nov-18	84	66	78	Anthony Lagoon Beds	Sandstone, Siltsone and Limstone layering
9793	RN038817	RN038817	03-Nov-18	212.83	76.67	190.95	Gum Ridge Formation	fractured brown limestone, above sandstone/ limestone

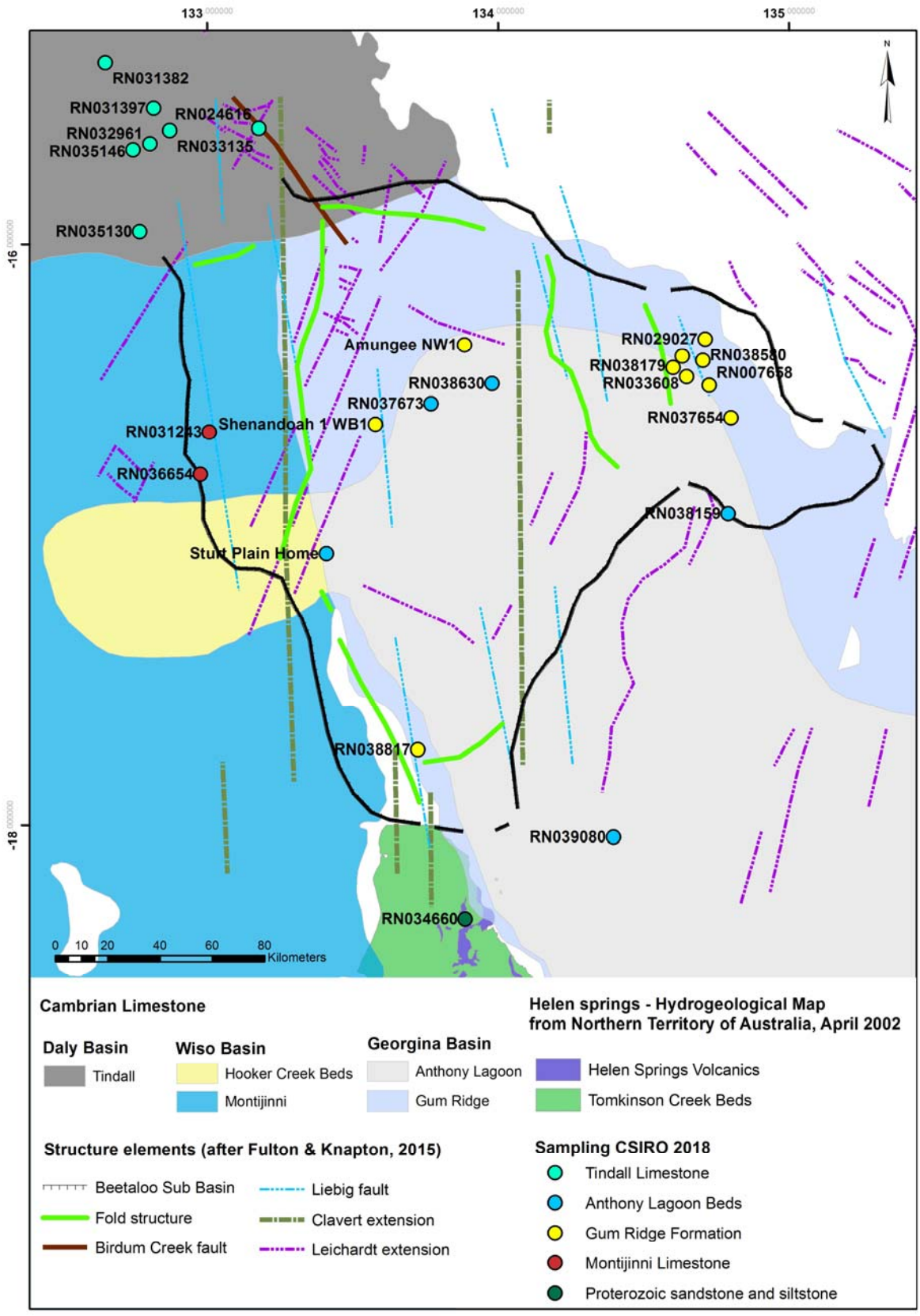

Figure 3.2 Hydrogeological map of the Beetaloo Sub Basin including the sampling locations

3.2 Field sampling

During the 2018 field campaign 25 samples were taken from bores located in the following aquifers: Tindall limestone, Gum Ridge formation, Anthony Lagoon beds, Montijinni formation and Proterozoic sandstone. A Bore Boss pump (Model no: BBR300S) was used for bores without any pump headworks. For bores with headworks, water samples were collected from existing sampling taps or a fitted outlet on the pump headworks.

Bores were purged for a minimum of three to five bore volumes. During sampling a steady state condition was maintained, and the pumping rate of the groundwater bore (bore yield) was estimated using a 9-litre bucket. Where this method was not practical due to the size of the flow or headworks configuration, bore yield was obtained from information provided in the Northern Territory groundwater database (NT 2019). During purging, field parameters were monitored regularly, and groundwater samples were collected only when the field parameters were stabilised within a range outlined in the NT Government methodology for the sampling of groundwater advisory note (DPIR 2016).

Field parameters – Electrical Conductivity (EC), pH, temperature, Oxidation Redox Potential (ORP), Dissolved Oxygen (DO) – were measured using Eureka Manta 2 Multiparameter water quality meters. Water quality meters were routinely field calibrated against standard solutions during the field program. EC and DO measurements have a precision of ±1 % units. Temperature and ORP measurements have an instrument precision of ±0.1°C and ±20 mV. The pH readings have a precision of ± 0.2.

Samples for major ions and trace elements of the groundwater were taken by CSIRO Energy (Wilkes *et al.* 2019).

Groundwater samples were collected using a flow rate leading to minimal bubbling, using bottles of size and type appropriate for their transport and later tracer analyses. Samples for CFCs and SF_6 were collected and sealed under the water surface in a bucket to limit contamination from ambient air. Samples for noble gases were collected using copper tubes and clamps developed by CSIRO.

Samplings of radon (Rn) isotopes were conducted after the method described by Leaney and Herczeg (2006).

Samples for strontium isotopes were taken in 150 ml PE bottles and analysed at the analytical services unit of CSIRO. For stable water isotopes, two glass McCartney bottles (each ca. 25 ml) were sampled without headspace. Carbon-14 and $\delta^{13}C$ were sampled in 1l PE bottles. All bottles were flushed three times before filling.

For rare earth elements including yttrium (REE+Y), 4 litres were sampled from the well and directly filtered with a 0.2 µm filter and acidified with ultrapure HCl. After sampling every sample was adjusted to pH 2 with ultrapure HCl, spiked with 1 ml Tm solution and slowly transferred on a cartridge containing cation exchange resin. Every cartridge was stored well packed and cooled until sending to the lab at the Environmental Research Centre (UFZ) in Germany.

Samples for $\delta^{34}S$ and $\delta^{18}O$ on sulphate were taken in 1.5l bottles. After filling the bottle without any bubbling, NaOH and $BaCl_2$ were added to bring the pH > 8 for precipitating $BaSO_4$. When the

water was clear after several days, only the precipitates was collected in smaller bottles (ca. 50 ml) and send to the lab at the Environmental Research Centre (UFZ) in Germany.

3.3 Analytical methods

Radon samples were transported from the field back to the CSIRO Environmental Tracer Laboratory (ETL) at the Waite Campus where analysis took place within two weeks after sampling using a Quantulus Liquid scintillation counter with an analytic precision of 5% and an overall detection limit of 0.01 Bq/L. Noble gas samples in copper tubes were also analysed at CSIRO ETL. Dissolved gasses were first separated from water on an offline extraction system. The resulting gas subsamples were analysed on a fully automated facility; this includes drying of all gases, raw gas analysis to determine the N_2/Ar ratio on a quadrupole mass spectrometer, separation of noble gases from reactive gases using a variety of reactive getter systems, separation of the noble gases by cryo techniques and measurement of gas amounts and their isotopic composition using a spinning rotor gauge, quadrupole mass spectrometers and a high-resolution HelixMC noble gas mass spectrometer (Suckow *et al.* 2019). Post processing of all radon and noble gas measurements was done using the LabData laboratory information management and database system (Suckow and Dumke 2001).

The following tracers were measured at GNS in New Zealand. For tritium, electrolysis was used to prepare an isotopically enriched subsample, then liquid scintillation counting to measure the tritium activity with an over all detection limit of 0.03TU. The molecular gas tracers SF_6, CFC-11, CFC-12, CFC-113 and Halon (H1301) were measured via purge and trap gas chromatography and an electron capture detector with a detection limit of 0.05pMol/kg for the CFCs and 0.2 fMol/kg and 0.3 fMol/kg for SF_6 and H1301 respectively. ^{14}C and $\delta^{13}C$ was measured via accelerator mass spectrometry and Isotope Ratio Mass Spectrometry (IRMS) at the Rafter Radiocarbon Laboratory with an accuracy of 0.2‰ for $\delta^{13}C$ and a detection limit of 0.5% for ^{14}C. Stable isotopes of water were measured in the stable Isotope Laboratory of GNS, New Zealand with analytic precision of 0.2‰ and 1.5‰ for $\delta^{18}O$ and $\delta^{2}H$ respectively.

Measurement of $\delta^{34}S$ and $\delta^{18}O$ isotopes of sulphate was done at the Environmental Research Centre (UFZ) in Germany using an Isotope Ratio Mass Spectrometer (IRMS delta S Finnigan MAT) coupled with continuous flow combustion technique to determine the respective isotope ratios. Analytical error (2σ) was ±0.3‰ for sulphur and ±0.6‰ for oxygen. Results are given in δ notation as $\delta\ ^{34}S(SO_4)$ and $\delta^{18}O(SO_4)$ as parts per thousand (‰) deviation relative to the Vienna Cañon Diablo troilite (VCDT) ^{34}S standard and Vienna Standard Mean Ocean Water for ^{18}O, respectively (VSMOW, IAEA). The IAEA-distributed reference material NBS 127 ($BaSO_4$) was used. The rare earth elements including Yttrium were analysed with high-resolution inductive coupled plasma mass spectrometry (HR-ICP-MS Element XR, Thermo Scientific, Germany). The recovery of the Tm-spikes was better than 83%.

3.4 Data evaluation

All post-processing and Lumped Parameter Modelling (LPM) presented in the following sections was done using the LabData laboratory information management and database system (Suckow and Dumke 2001) including the Lumped Parameter Modelling Code Lumpy (Suckow 2012, 2014b).

3.4.1 Major ions

Charge balance and alkalinity

Ion charge balance errors were calculated to check of plausibility of major analysis (Appelo and Postma 1999). It is applied to estimate the validity and quality of the water analyses or to identify unanalysed parts. An ion charge balance error between -5% and 5% is acceptable. A negative error indicates higher concentration of anions and positive error a higher cation amount.

$$\frac{\Sigma cations - |\Sigma anions|}{\Sigma cations + |\Sigma anions|} * 100 \approx \pm 5\%$$

Analyses were given in mg/l and on the basis of the atomic masses of each parameter and ion charge all concentrations for the dominating ions were transferred to meq/l. Dominating cations are: Ca, Mg, Sr, Na, K; dominating anions are: Cl, SO_4, NO_3, TDIC. The calculated ion charge balances for the analyses performed at CSIRO Energy range between 3% and 24% with only 4 analyses below 5%. The charge balance is positive throughout, meaning that more charges from cations have been determined than anions. There is also a significant difference between the TDIC measurement performed at the laboratory of CSIRO Energy and the titration performed in the field, where nearly all field titrations give a lower value for TDIC than the laboratory. One would normally expect the opposite: degassing of CO_2 on the way from the field to the lab would explain a higher value in the field, as would the dissolution of particulate material during titration (field titration is performed on the raw water whereas the lab analysis is performed on filtrated water). If one uses the values from field titration in the charge balance, the charge balance gets worse and increases from 4.8% to 35%. The reason for the bad charge balance and the discrepancy between TDIC field measurement and laboratory is not clear. While this is not satisfying, in the following discussion it was decided to ignore the TDIC values from the field titration, to achieve a better charge balance and to keep the discussion congruent between the field campaign from 2017 (where no field titration was conducted) and 2018.

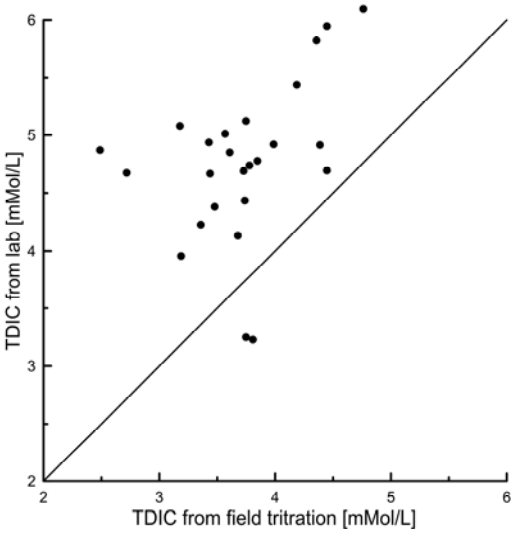

Figure 3.3 Comparison between field titration and laboratory analysis for Total Dissolved Inorganic Carbon (TDIC).

Chloride mass balance

The chloride mass balance (CMB) method was used to estimate recharge rates. The method compares the concentration of chloride in groundwater Cl_{GW} (mg/L) to that of rainfall Cl_P. The ratio of the chloride concentrations gives the proportion of precipitation P (mm/y) that becomes recharge (Davies and Crosbie 2018):

$$R = P \cdot \frac{Cl_P}{Cl_{GW}} = \frac{D}{Cl_{GW}}$$

Where R is the recharge rate (mm/y) and D is the chloride deposition rate (mg/m^2/y). To determine the chloride deposition rate, the average annual rainfall, as well as the chloride concentration in rainfall need to be measured. The closest stations to the Beetaloo Sub-Basin where such measurements are available are Darwin, Mount Isa, Halls Creek, and Alice Springs (Crosbie *et al.* 2012). Recently, Davies and Crosbie (2018) produced a gridded (0.05° grid) chloride deposition rate map for all of Australia, based on these and other measurements, which was used to calculate the chloride mass balance here.

3.4.2 Rare earth elements

Results of rare earth elements including yttrium (Y) were given in ng/l. To prepare comparable REE+Y patterns, C1 – standardization is applied by the use of C1 chondrite composition (Anders and Grevesse 1989), see Table 5 and Table 6. The rare earth element thulium (Tm) is used as spike for quality check of the sample preparation and therefore it is not considered in the interpretation of the results. The rare earth element promethium (Pm) was not analysed.

Table 5 Masses of rare earth element including Y from C1 chondrite (La to Gd) after Anders and Grevesse (1989)

	La	Ce	Pr	Nd	Sm	Eu	Gd
C1 chondrite [pmol/kg]	1691864.7	4304068.5	631653.7	3134535.4	977393.6	368421.1	1252384.0

Table 6 Masses of rare earth element including Y from C1 chondrite (Tb to Lu) after Anders and Grevesse (1989)

	Tb	Dy	Y	Ho	Er	Tm	Yb	Lu
C1 chondrite [pmol/kg]	226557.6	1495384.6	17546642.0	339599.8	950388.5	142095.9	942196.5	137142.9

Rare earth elements including yttrium (Y) support major and minor elements as an appropriate tool to characterize groundwater composition and development. Rare Earth Elements in water form characteristic patterns (“fingerprints”) that the infiltrating water and groundwater acquire (Johannesson *et al.* 1997; Johannesson and Lyons 2000).

In the study area two main types of REE patterns can be distinguished:

A) Tindall Limestone

There is a typical REE pattern for the Tindall limestone groundwater with a strong negative Ce anomaly. Samples of the Anthony Lagoon Beds (Sturt plain Home and RN039080) and the Proterozoic sandstone (RN034660) are further characterized by an increasing trend of the heavier REE.

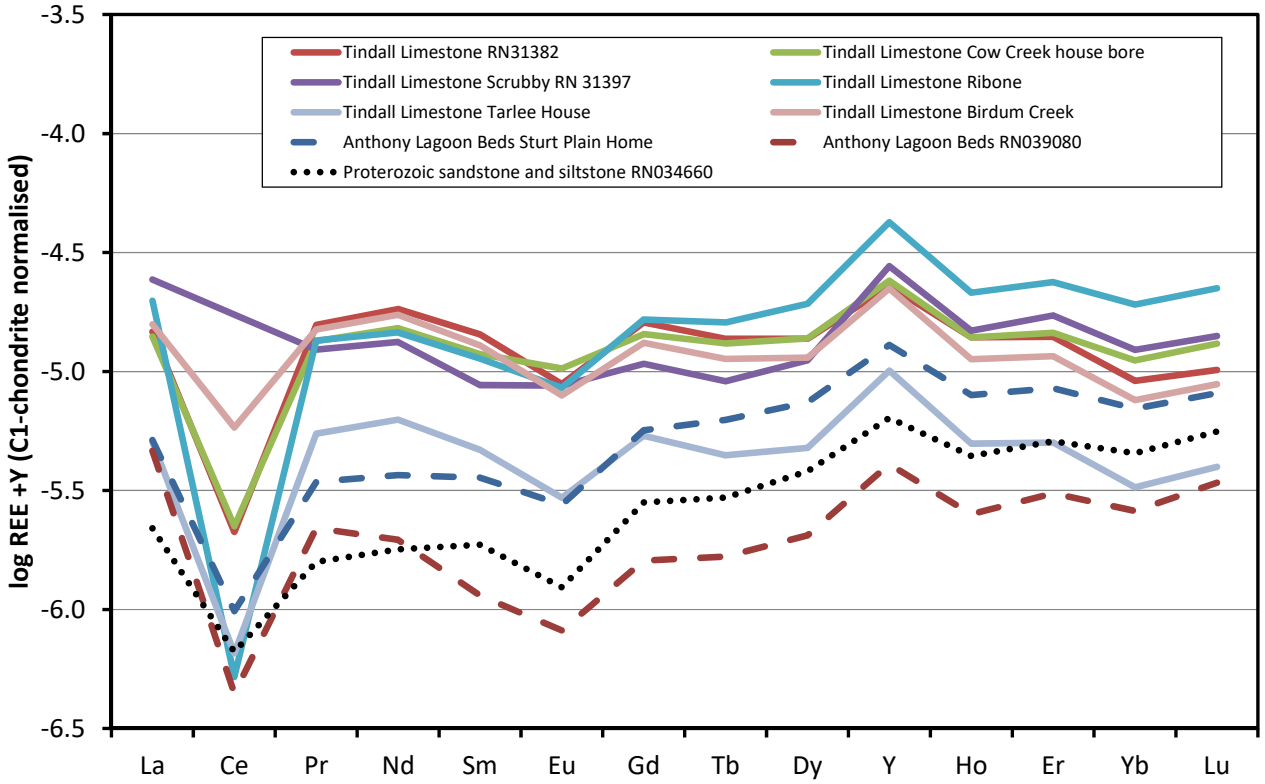

Figure 3.4 Specific REE pattern for groundwater of the Tindall Limestone.
This pattern is also shown in two samples of the Anthony Lagoon Beds (Sturt plain Home and RN039080) and of the Proterozoic Sandstone and Siltstone (RN034660).

B) REE groundwater pattern of Gum Ridge, Anthony Lagoon Beds and Montijinni formations

The REE analyses of groundwater from Gum Ridge, Anthony Lagoon Beds, Montijinni formations show a typical limestone pattern. A positive Ce-anomaly like in Shenandoah 1 WB1 can be related to dissolution of Fe-hydroxide in groundwater with low oxygen content, reducing conditions, or organic-rich environment. The sample from Amungee NW 1 could be influenced by groundwater from volcanic/basalt layers (bowl shape pattern).

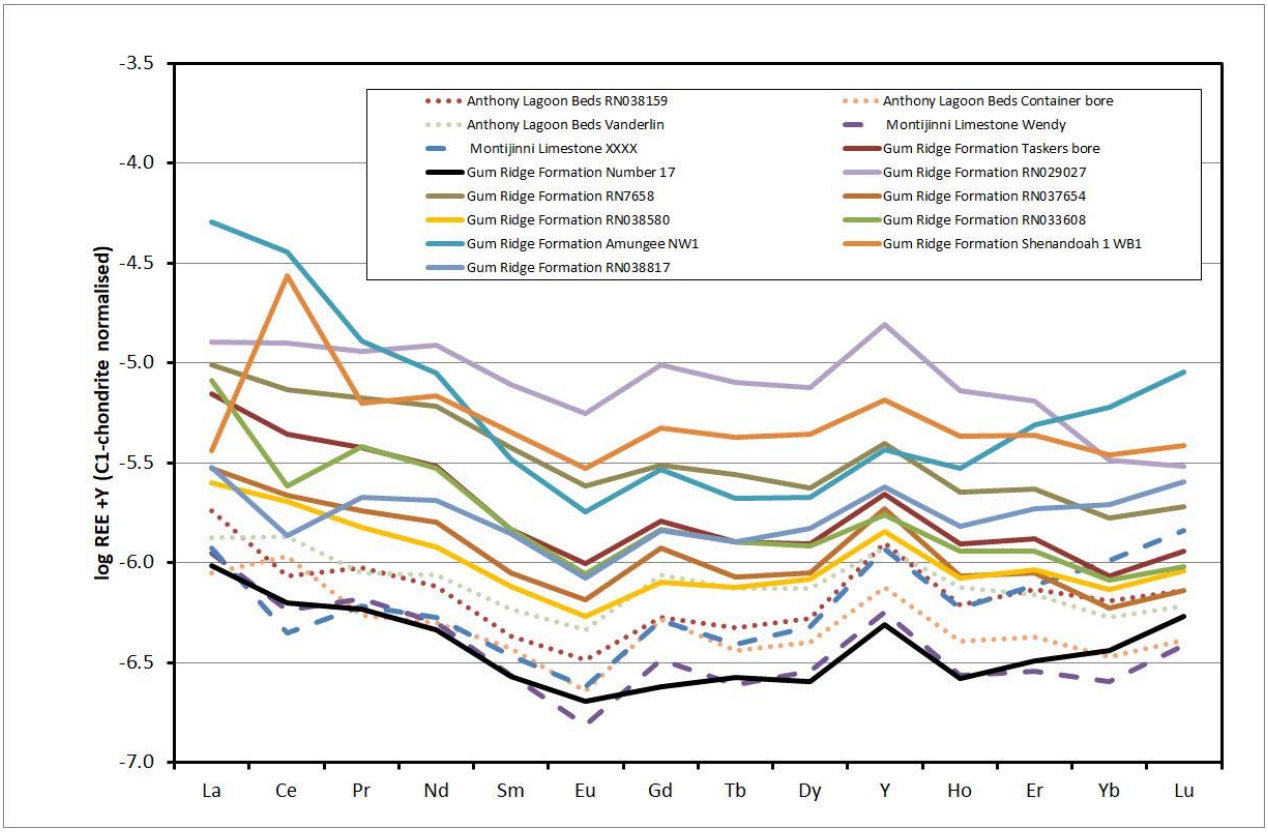

Figure 3.5 Specific REE pattern of the Gum Ridge, Anthony Lagoon Beds Montijinni Formations.

3.4.3 Cluster analysis

A cluster analysis was performed using the results of major ion, trace element, stable isotope and REE measurements. The goal was to identify groups (clusters) of samples that are similar and to assess their spatial distribution. The clustering is typically used to correlate groups with geographically distinct regions or with stratigraphic units.

The data to be used for the cluster analysis was selected as follows: First, because the current version of the data analysis script cannot deal with missing data points, parameters that were not measured in a significant number of samples (e.g. $\delta^{18}O$ of SO_4) were removed. Second, elements that were below the detection limit for a significant fraction of the samples were excluded. Third, for parameters that strongly correlate with each other (e.g. Cl, Na, and Br), only one representative parameter was selected, and the others removed to avoid obtaining clusters that just reflect different amounts of total dissolved solids. Finally, isotopes that mainly serve as tracers of age (^{3}H, ^{14}C) were omitted. The following parameters remained and were used for the cluster analysis:

- major and minor ions (8): B, Ca, Cl, Fe, Li, SO_4, TDIC, and Zn
- rare earth elements (3): Ce, Dy, and La
- isotopes (4): $\delta^{18}O$, $\delta^{13}C$, $^{87}Sr/^{86}Sr$, and ^{222}Rn

The data was then standardized using the equation $a_i = (z_i-z)/s$, where a_i is the a-transformed value, z_i is the original result (in mg/L), z and s are the mean and standard deviation of the sample

observations. Next, clusters were identified with Ward's hierarchical clustering method (using Euclidian distances). The significance of clusters was determined by multiscale bootstrap resampling using the Pvclust package (Suzuki and Shimodaira 2006). Finally, the identified clusters were used to create maps and box plots of concentrations of selected parameters for each cluster. All calculations were done with R scripts (R version 3.4.4).

4 Tracer results

- Hydrochemical and isotope cluster analysis allows distinction of water types by region.
- Stable isotopes of groundwater are on the negative side of local precipitation indicating that mainly Monsoon seasons with high amount of precipitation contribute to recharge.
- Tritium is absent in most samples, indicating localized recharge mainly in the north and east.
- Anthropogenic gas tracers (CFCs, SF_6, H1301) are detected in nearly all samples; this suggests recent recharge (since 1950), however contradicts tritium results.
- Radiocarbon (^{14}C) increases with flow distance in contrast to the expectation of radioactive decay with increasing travel time.
- ^{14}C can be explained as binary mixture indicating that radioactive decay along the flow path is negligible ("age" <2ky), confirming high flow velocities and short residence times.
- Helium is higher than solubility equilibrium during recharge in most samples, indicating production from U & Th decay and localized influx from deeper layers.
- Heavy noble gases (Ne, Ar, Kr, Xe) indicate high recharge temperatures (30°C-42°C) and considerable excess air.

4.1 Hydrochemistry

Cluster analysis

To test which parameters are most useful in identifying meaningful clusters, the clustering algorithm was run with subsets of the parameters (e.g. only using the major and minor ions, or using major and minor ions, REE and stable isotopes) and the resulting clusters evaluated. We found that including more parameters in the clustering algorithm generally increased the differentiability (i.e. clusters are more distinct in terms of both the level at which they separate and their significance as determined by Pvclust) and spatial coherence of clusters (i.e. all samples within a cluster are in a distinct geological formation or location (latitude and longitude), rather than dispersed throughout the study area). Using one class of parameters, i.e. major and minor ions, produces the most spatially coherent clusters, but also the least distinct ones. The best match between clusters and geological formations (and the highest distinction of clusters) was obtained when combining all three classes of parameters. Stable isotopes and REE may thus be useful in addition to major and minor ions for identifying groundwater origin especially in wells with a wide screen that spans more than one geological formation or in wells where it is unclear in which formation they are screened in.

The disadvantage of using stable isotopes and REE for the clustering analysis is that there is a significant number of samples (especially from the first campaign in 2017) without isotopes and without any REE. Therefore, in the following, the results for two data sets are presented and discussed: a) clustering using only major and minor ions (8 parameters, 53 samples); b) clustering using major and minor ions, stable isotopes, and REE (15 parameters, 25 samples).

Based on major and minor ions

The cluster analysis based on major and minor ions only results in four main clusters, some of which are further divided into sub-clusters (Figure 4.1). Some of the clusters only contain samples from a specific geological formation (e.g. cluster A only from the Tindall or cluster B2 only from Gum Ridge). However, for most formations, samples are spread across several sub-clusters which belong to different main clusters. For example, samples from the Tindall are found in clusters A, B1, B3, and D3, which belong to different main clusters, while Gum Ridge samples are found in all clusters except A. Geographically, some of the clusters correspond to clearly identifiable regions (e.g. cluster A is the western part of the Tindall, whereas cluster B1 is the eastern part of the Tindall, cluster D2 represents the southernmost part of the study area, Figure 4.2). Conversely, in

the easternmost part of the study area, clusters B2, C, and D1 (which also do not belong to the same main cluster) seem to be randomly distributed.

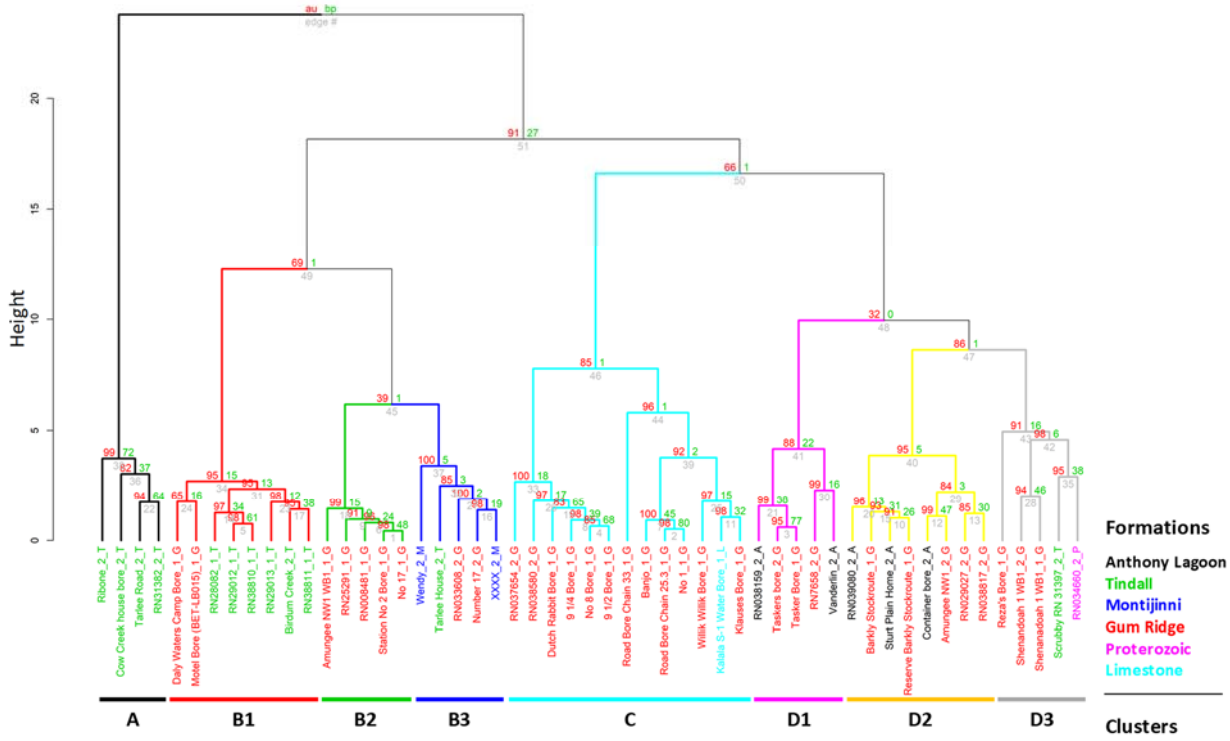

Figure 4.1 Hierarchical cluster dendrogram based on major and minor ions only (53 samples). Bore name are printed in the same colour as their formation.

There are notable differences in the chemistry of some of the main clusters. Some of these differences are visualised in Figure 4.3 and discussed in this paragraph. It is also possible to calculate for each cluster typical ranges of tracers that were not used in determining the clusters such as pH, $\delta^{13}C$, $\delta^{18}O$ and ^{222}Rn. This is particularly useful when comparing the two clustering methods that were used (i.e. clustering based on major and minor ions only versus also including stable isotopes and REE in the clustering itself).

Cluster A has by far the lowest mineralization of all clusters, and the highest Eh value and lowest Sr concentration and $\delta^{13}C$ value (the latter together with B1). C has the highest Li concentrations. The sub-clusters in D are often very variable, but all of them have relatively low TDIC and Ca concentrations compared to the other main clusters. Notable differences that separate the sub-clusters are: B1 has higher mineralization (highest of all clusters) than B2 and B3. The lowest pH of all clusters is found in B1, the highest in B2. In the D cluster, D3 has the lowest and D2 the highest mineralization. D3 has the highest $\delta^{18}O$ and ^{222}Rn. Conversely, Ca and Mg are lower in D3, as well as $\delta^{13}C$, which may indicate a lower availability of carbonate minerals in D3. Indeed, D3 contains the only sample from the Proterozoic sandstone and siltstone, as well as the Scrubby bore, where very high ^{4}He indicates an influence of deeper groundwaters. D1 has high Fe and Zn, as well as low $\delta^{18}O$ compared to B2 and B3. It is unclear, whether the high Fe and Zn in D1 represent contamination from the well casing or concentrations in the aquifer. Finally, where $^{87}Sr/^{86}Sr$ was measured, there are significant differences between different clusters.

A few bores were sampled in both sampling campaigns. Two of these (Shenandoah_1_WB1, Tasker's Bore) fall into the same sub-cluster both times. Another two (Number 17/No 17 and

RN033608/Station No 2 Bore) are in different sub-clusters, but still in the same main cluster. Finally, the Amungee_NW1 is in totally different clusters for the first and second sampling campaign.

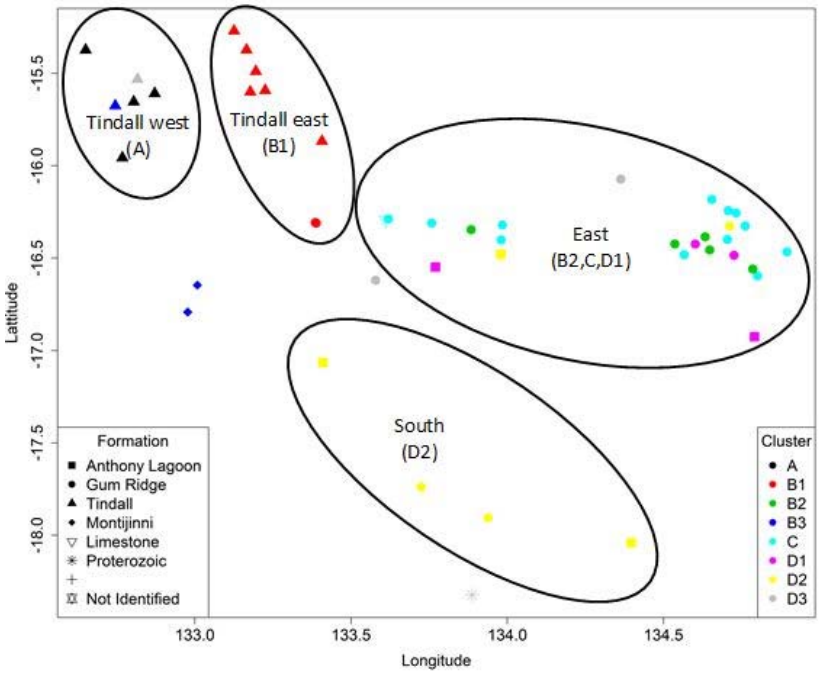

Figure 4.2 Map with the spatial distribution of the clusters based on major and minor ions only (54 samples).

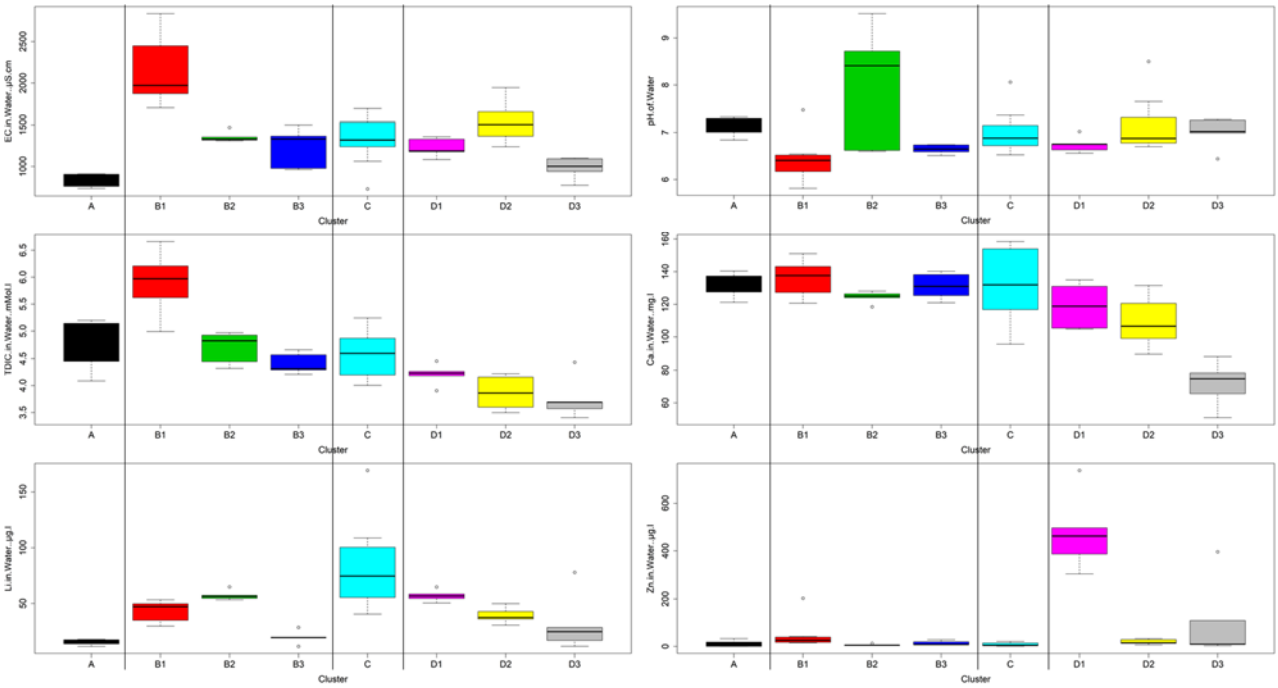

Figure 4.3 Boxplots of median and range of electrical conductivity (EC), pH, and concentrations for TDIC, Ca, Li, and Zn for the calculated clusters.
Outliers are presented as small circles.

Based on major and minor ions, stable isotopes, and REE

The cluster analysis based on major and minor ions, stable isotopes, and REE results in two main clusters that can be subdivided into seven sub-clusters (Figure 4.4). While samples from the same formation can often still be found in more than one cluster, there is now a clear distinction between samples from the Tindall and Montijinni formations in one main cluster (B), and samples from Anthony Lagoon and Gum Ridge in the other main cluster (A). Geographically, the observations from the chemistry-only clustering still apply (Figure 4.5): there is a cluster of samples in the south (A4); in the east, several sub-clusters are mixed randomly (A1, A2, A3), but at least, now they all belong to the same main cluster (A). The difference between western and eastern Tindall is not discernible anymore, because there is only one sample from the eastern Tindall. The fact that some samples in the Tindall are in the same cluster similar to the two samples from Montijinni suggests that there is some hydraulic connection between these two formations.

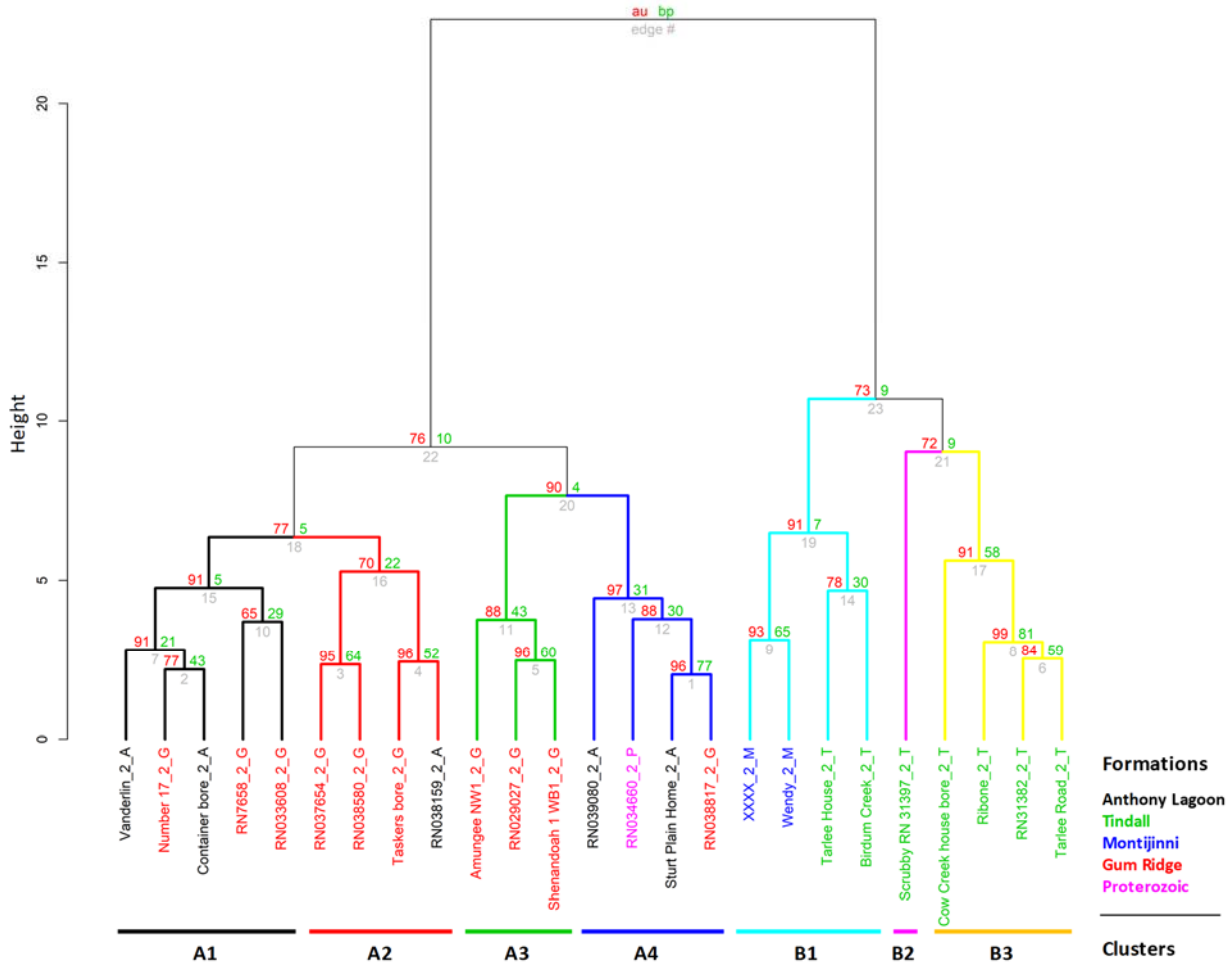

Figure 4.4 Hierarchical cluster dendrogram based on major and minor ions, stable isotopes, and REE (25 samples)

Some noteworthy differences between clusters in terms of their chemistry are given here. The significant difference between the two main clusters A and B is that $\delta^{13}C$ is generally lower in B, whereas the $^{87}Sr/^{86}Sr$ ratio is lower in A. In terms of chemistry, common differences are less obvious. The main difference between clusters A1 and A2 is that samples in A2 have much higher Fe, Li, and Zn concentrations. These metals are likely released by the reducing conditions found in A2, which is the only cluster where Eh is clearly negative. The southern sub-cluster (A4) deviates

from the other sub-clusters in A by having higher pH, and higher Cl concentrations and $\delta^{18}O$ values, which together may indicate more evaporation in this region than elsewhere. The main difference between B1 and B3 is that Cl and SO_4, in fact salinity overall, are significantly lower in B3, whereas pH is higher in B3 (7.2 instead of 6.7). TDIC in the Scrubby Bore (cluster B2) is significantly lower than in B1 and B3 (which have the highest TDIC of all clusters).

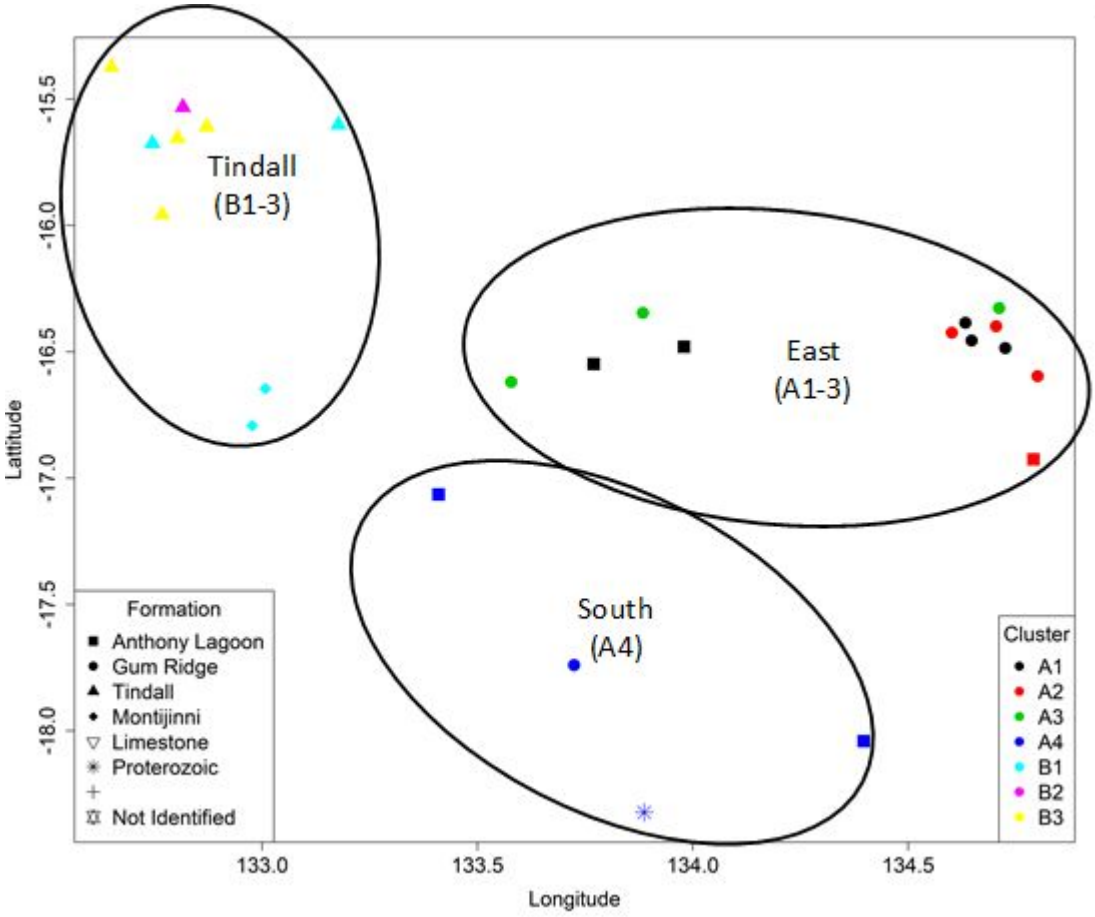

Figure 4.5 Map with spatial distribution of the clusters based on major and minor ions, stable isotopes, and REE (25 samples)

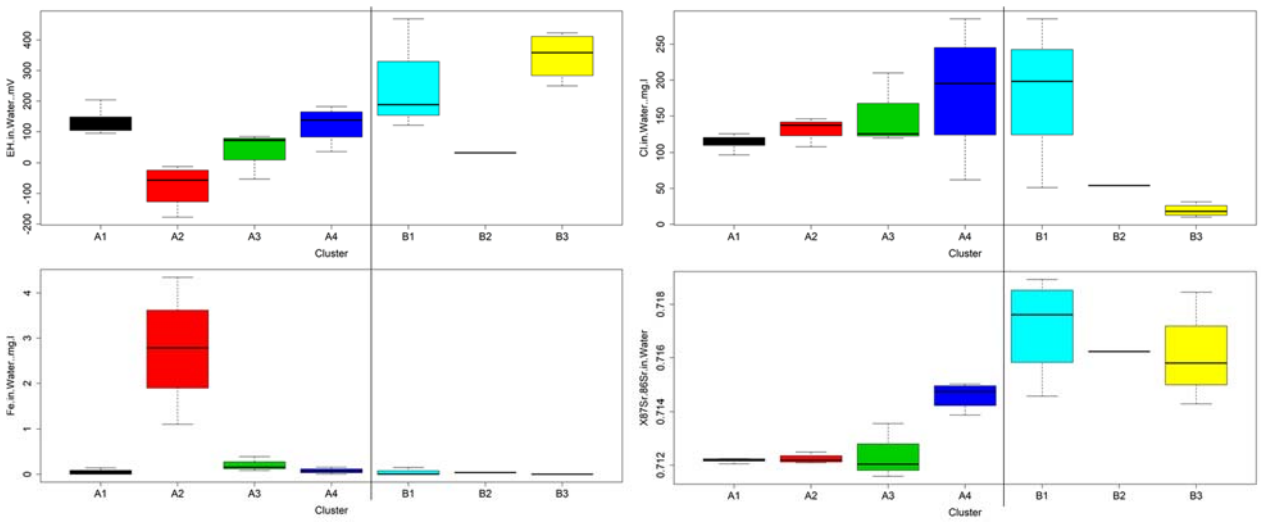

Figure 4.6 Boxplots with median and range for Eh, pH, Fe concentration, and $^{87}Sr/^{86}Sr$ ratio for the calculated clusters. Outliers are presented as small circles.

Implications

There are some general implications from the two clustering versions that are summarized here:

- There are three groups of clusters that can be distinguished spatially (Figure 4.2 and Figure 4.5): a southern cluster, an eastern group of clusters (which do not seem to be organized spatially, but rather randomly mixed), and clusters in the north, where the Tindall Limestone is found.
- The southern group of samples may be affected by more evaporation than the others.
- In the Tindall Limestone, there are two quite distinct flow paths in the west and east, respectively. The difference may either be related to different recharge areas (the western part getting its water from the Montijinni Limestone, whereas the eastern part would get water from Gum Ridge and Anthony Lagoon Aquifers) or to more local recharge in the west of the Tindall Limestone and dilution of the more saline water coming from the south.
- The Scrubby Bore is a bit of an outlier in the Tindall Limestone. The bore profile suggests that it may be influenced by some of the deeper sandstone aquifers, which is confirmed by the chemistry and elevated helium (Figure 4.1).
- It is not possible to establish a direct equivalence of (sub-)clusters between the two different data sets used for clustering, partly because the number of samples and spatial coverage vary, partly because some of the clusters overlap. Consequentially, we will not interpret the environmental tracers directly in the frame of any of the two cluster dendrograms.
- Variations in clustering that could be attributed to differences in rare earth elements were not observed across these data, i.e. clustering was apparently driven more by other analytes.

4.2 Stable Isotopes of water: δ^2H & $\delta^{18}O$

Stable Isotopes of the water molecule (δ^2H & $\delta^{18}O$) have been measured in a variety of historical studies. Figure 4.7 shows the precipitation data collected within the Global Network for Isotopes in Precipitation (GNIP) for the stations Darwin and Alice Springs, together with the stable isotope data of several historical studies and the new data collected in this study. The groundwater data are mostly on the negative side of the precipitation record, indicating that only the heavy rainfalls in the monsoon period contribute significantly to groundwater recharge.

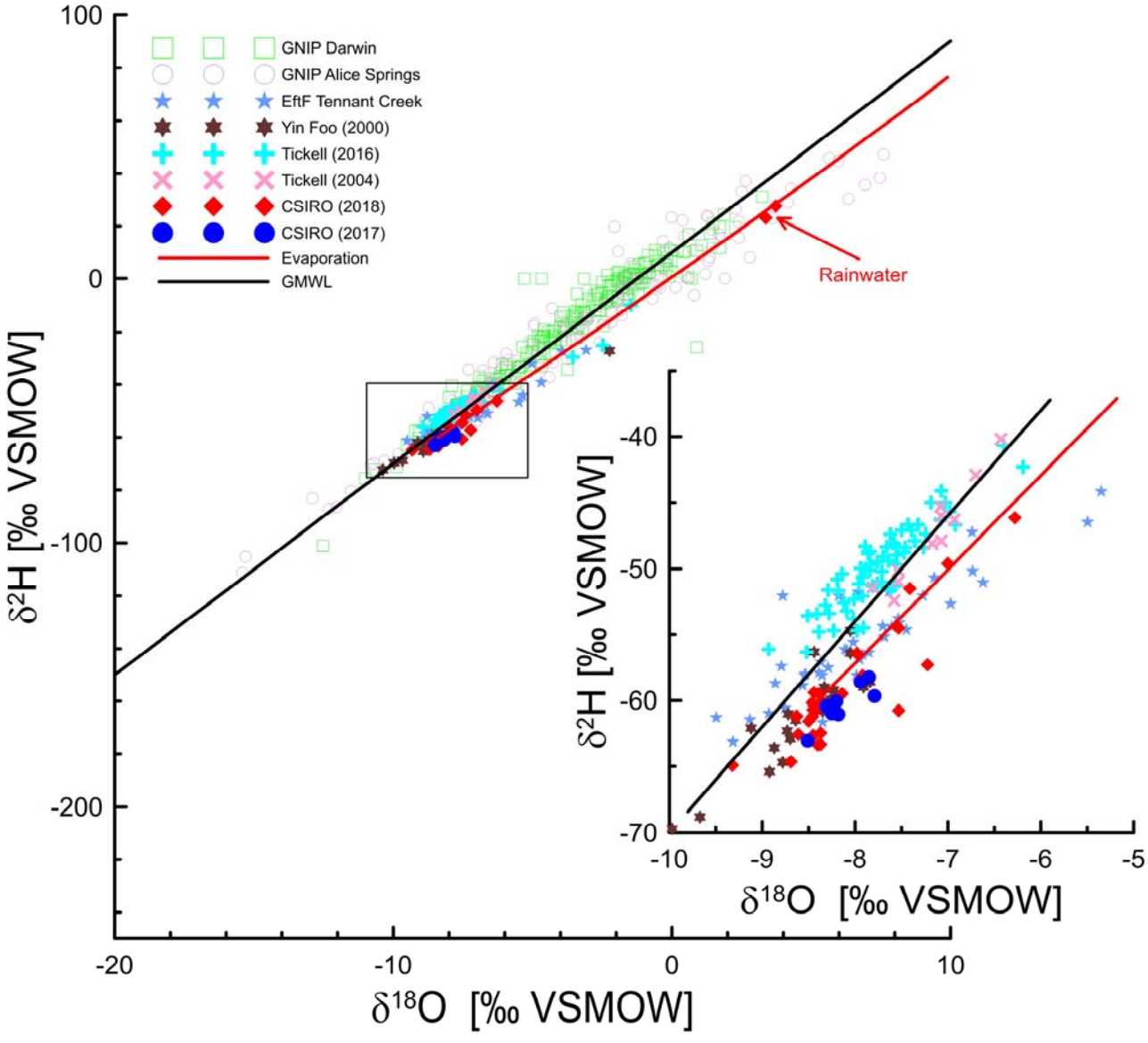

Figure 4.7 Stable Isotope plot δ^2H vs. $\delta^{18}O$.
The black line is the Global Meteoric Water Line (GMWL), the red line an evaporation line for a humidity of 30% and 30°C (Gonfiantini 1986). The GNIP stations Darwin and Alice Springs are taken as reference, together with historical data and the two CSIRO campaigns in 2017 and 2018.

During the 2018 campaign the team was able to collect a rainwater sample which plots on the positive side in both isotopes. These rainwater samples lie on an evaporation line calculated for 30°C and 50% humidity (Gonfiantini 1986). The samples from the Ooloo Dolostone are on average slightly more positive in both isotopes and lie along the GMWL (Tickell 2004). The samples from

Geoscience Australia (https://www.ga.gov.au/eftf/about) collected during the program Exploring for the Future rather follow the evaporation line, as do the data from Yin-Foo and Matthews (2000). In contrast, the data from the Tindall Limestone collected by Tickell (2016) are shifted by a few ‰ to more positive values for δ^2H only. The latter has no known physical explanation and may just be a shift due to different calibrations used in different laboratories.

4.3 Tritium (^3H)

A groundwater sample that contains tritium levels above the detection limit – in this study 0.05 TU – is an indication that part of this water recharged later than 1963 (see Appendix for details). Some attenuation of the tritium signals is expected due to diffusion and dispersion in the unsaturated zone and/or rapid movement of water along preferential routes (Zimmermann *et al.* 1967; Allison *et al.* 1971). In a comparison with tracers, ^3H was observed to give a much older age in recharge to porous aquifers than gas tracers such as CFCs, SF_6 and ^{85}Kr, with the difference attributed to slow percolation of water through thick unsaturated zone (Cook and Solomon 1995). However, in karst systems also the opposite was observed, that tritium reaches the water table faster than gas tracers through preferential flow paths, while the latter re-equilibrate during percolation (Wilske *et al.* 2019). Figure 4.8 shows the measured tritium concentrations as depth profile below the groundwater table.

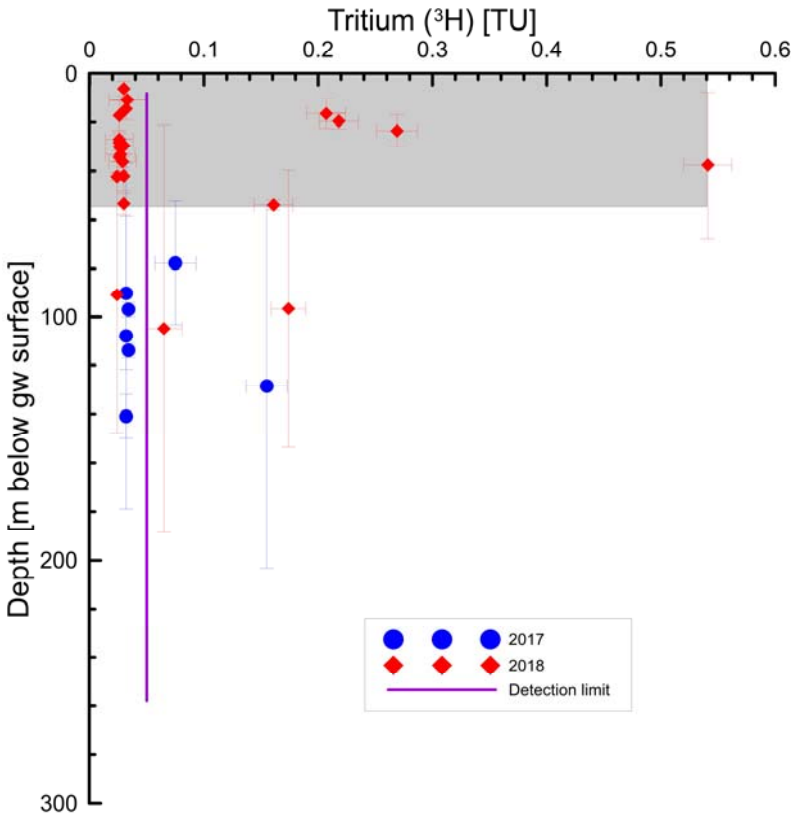

Figure 4.8 Plot of measured tritium (TU) vs. screen depth below groundwater.
Vertical error bars indicate the screen length. The shaded box represents the measurements used for recharge calculation (see discussion).

This depth profile shows that also for samples from wells extending down to 200m below groundwater, tritium is still detectable. However, many bores have either very long screens or are open boreholes with a very long intake interval (vertical error bars in Figure 4.8 indicate the upper and lower extents of the screens). If the dataset is restricted to a narrow intake interval of less than 10 m, then tritium is found only to less than 60 m depth below groundwater. All deeper wells have intake intervals long enough to extend also to a depth of less than 60 m and therefore most probably represent mixtures of tritium free water with some admixture of water containing tritium at shallow depth. However, restricting the dataset to wells with only short screens also demonstrates that many of the shallowest bores contain no tritium. This indicates that the recharge, leading to the observed tritium in groundwater, is not happening throughout the area but is a “patchy” process.

For four other bores no screen information was available hence they are not included in the plot. Their tritium concentrations measured as 0.026, 0.026, 0.035 and 0.275 TU, only the last being above detection limit – well BET-LB062, Shenanadoah 1 WB1.

Figure 4.9 shows the distribution of the tritium concentrations across the basin. In the south (mostly bores within the Gum Ridge and Anthony Lagoon Beds) only two bores had tritium levels above detection limit (=50mTU), whereas in the north (Tindall Limestone) there were more bores with detectable tritium and they are more frequent in the west. Indeed, the bores in the south are mostly in areas where the Gum Ridge is overlain by the Anthony Lagoon beds and/or up to 100 m thick cretaceous sand and clay, which can limit the contribution from young local recharge. The most Southerly bore, which exhibited 0.17 TU, is in Proterozoic sandstone. Another bore (Shenandoah 1 WB1), ~50 km SE of Daly Waters had no depth information though it is reportedly in the Gum Ridge Formation and exhibited 0.28 TU. This bore may be in an area where indirect recharge from ephemeral drainage occurs.

The higher tritium values in the NW indicates more modern recharge in the Tindall than in the Southerly formations. Anecdotal information obtained from landholders can add to the picture, e.g. during drilling one of the NW bores circulation fluid was lost at a depth of some tens of meters with no return of the drilling mud, however after some time it was noticed fluid began discharging and filling the bottom of a large sink hole 50 m to the North. This is indicative of significant connectivity at depth, and if sinkholes such as these act as points of indirect recharge then its reasonable that nearby bores would have higher tritium values indicating young water components.

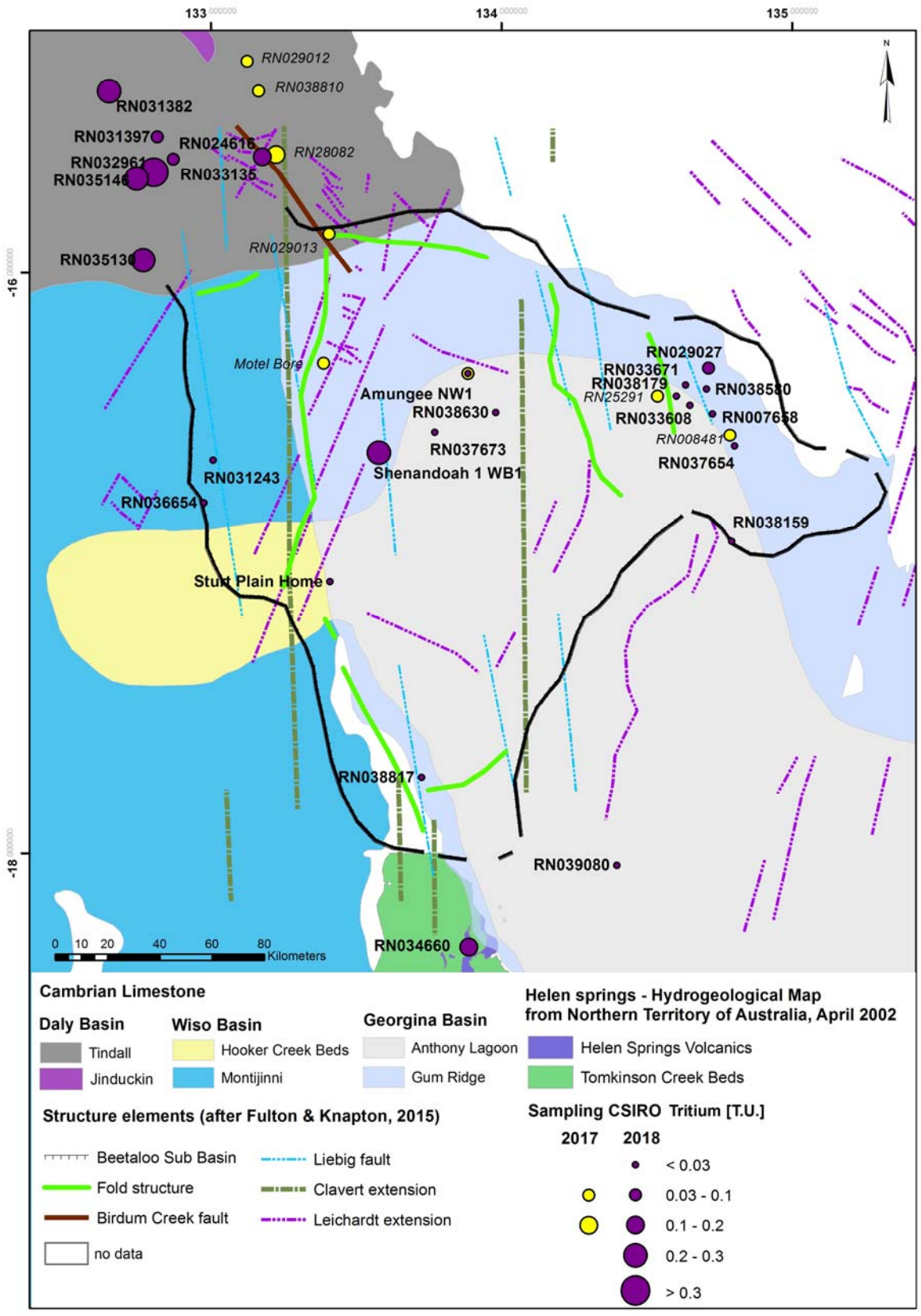

Figure 4.9 Map with tritium values at different bores.

4.4 Transient Anthropogenic Molecular Gas Tracers

The chemicals sulphur-hexafluoride (SF_6), halon H1301 and chlorofluorocarbons (CFC-11, CFC-12 and CFC-113) were measured during the 2018 campaign, whereas only SF_6 and halon H1301 were measured in 2017 (Suckow *et al.* 2018). These tracers indicate groundwater residence time scales of decades and their presence indicates contact of the groundwater with air later than the (ongoing) anthropogenic releases of these trace gases to the atmosphere throughout the last century.

All molecular gas tracers show high values at all depths from zero to nearly 200 m below the groundwater table (Figure 4.10), similar to the comparisons for SF_6 and halon made previously (Suckow *et al.* 2018). Only one sample each of SF_6 and H1301 is at the detection limit, and only few samples are at the detection limit for CFCs. This observation reveals a discrepancy in the behaviour of tracers transported with the water (like tritium) and those observing gas exchange (like CFCs, SF_6 and H1301). There is no distinct spatial pattern when mapped (see the map of SF_6 in Figure 4.11 which is the only display created for the gas tracers as an example), although the general tendency is like tritium, with higher concentrations found in the northwest of the study area. There is also high H1301 and SF_6 in the Gum Ridge and Montijinni formations, not only in Tindall Limestone.

One possibility for high values is for there to be a local source of contamination, e.g. items releasing CFC. The high values are unlikely to be caused by a localised source of contamination as the concentrations do not show a trend with the flow-path. Another reason why contamination is not probable is the remoteness of the area from any industry using CFCs, SF_6 and H1301 and the fact that all tracers are high simultaneously. Another possibility to explain high SF_6 values in groundwater discussed in the literature is underground production (Harnisch and Eisenhauer 1998; Koh *et al.* 2007; Friedrich *et al.* 2013), but this was never discussed for the CFCs and H1301 which are also very high.

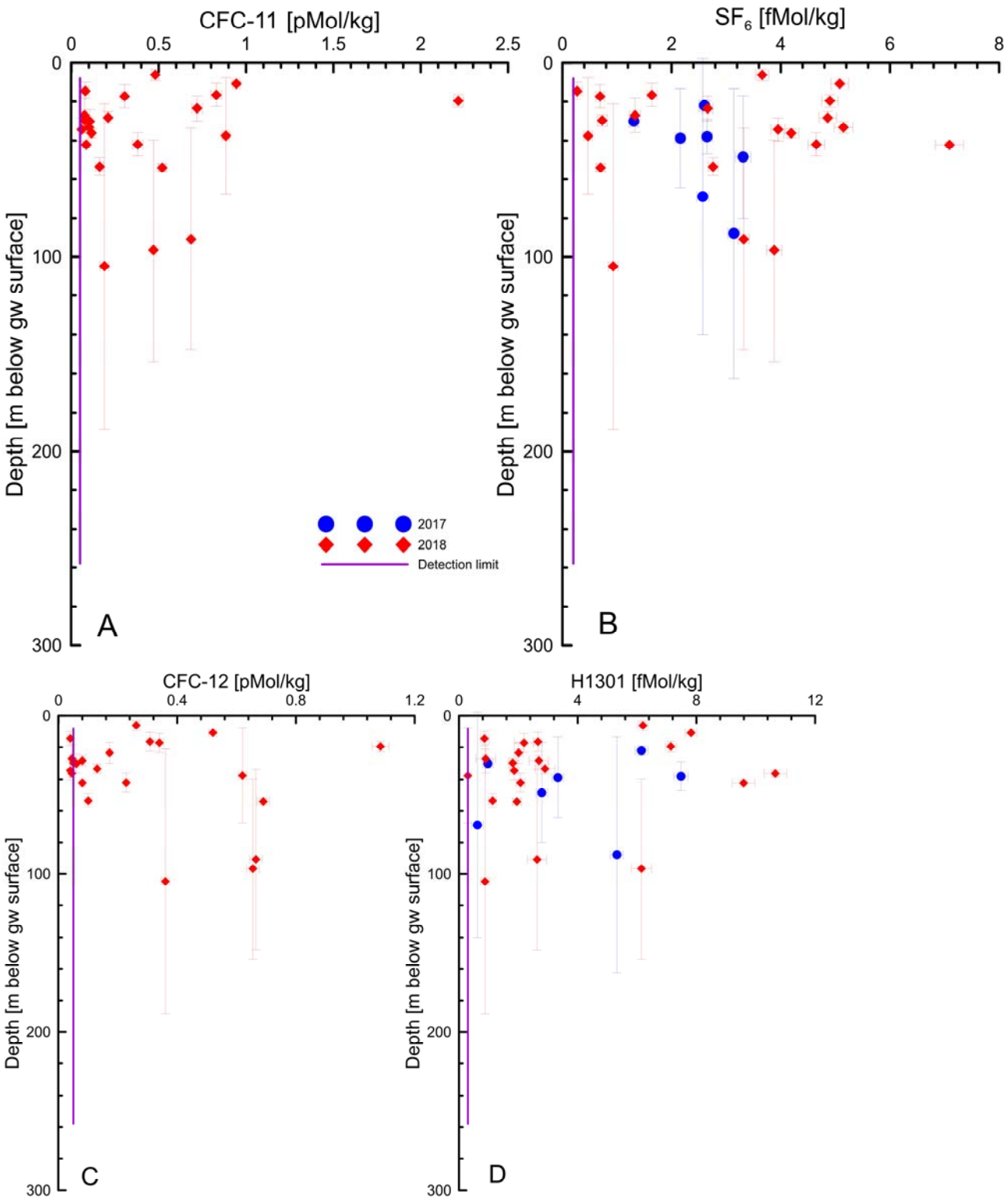

Figure 4.10 Plot of concentration versus depth below water level for transient gas tracers
A: CFC-11; B: CFC-11; C: CFC-12, D: SF_6. Magenta lines are the detection limit for each analyte.

The cross-plots of these tracers against tritium in Figure 4.12 show concentrations of the tracers from each sampled bore, and lines representing different mixing models. In these plots, most bores fall towards the gas-tracer side of the model lines, which indicates that the concentration of the gas tracer is too high for the gas tracers as compared to tritium. For this most recent data set, measurements of the CFCs are also available, whereas in the 2018 report only SF_6 and halon were

measured. The CFCs, like the other molecular gas tracers, exhibit concentrations that are in excess compared to the measured tritium.

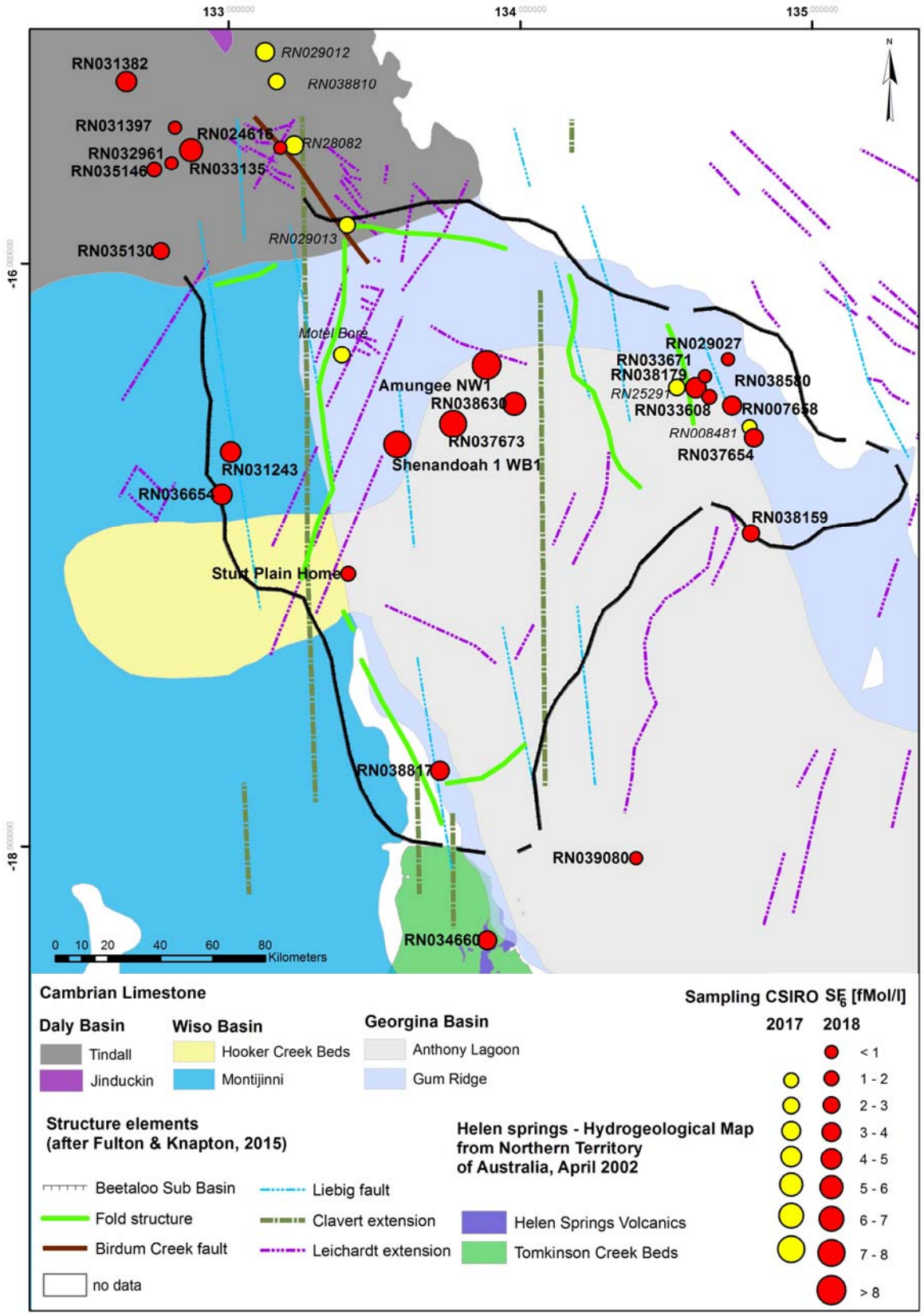

Figure 4.11 Map of SF_6 concentrations

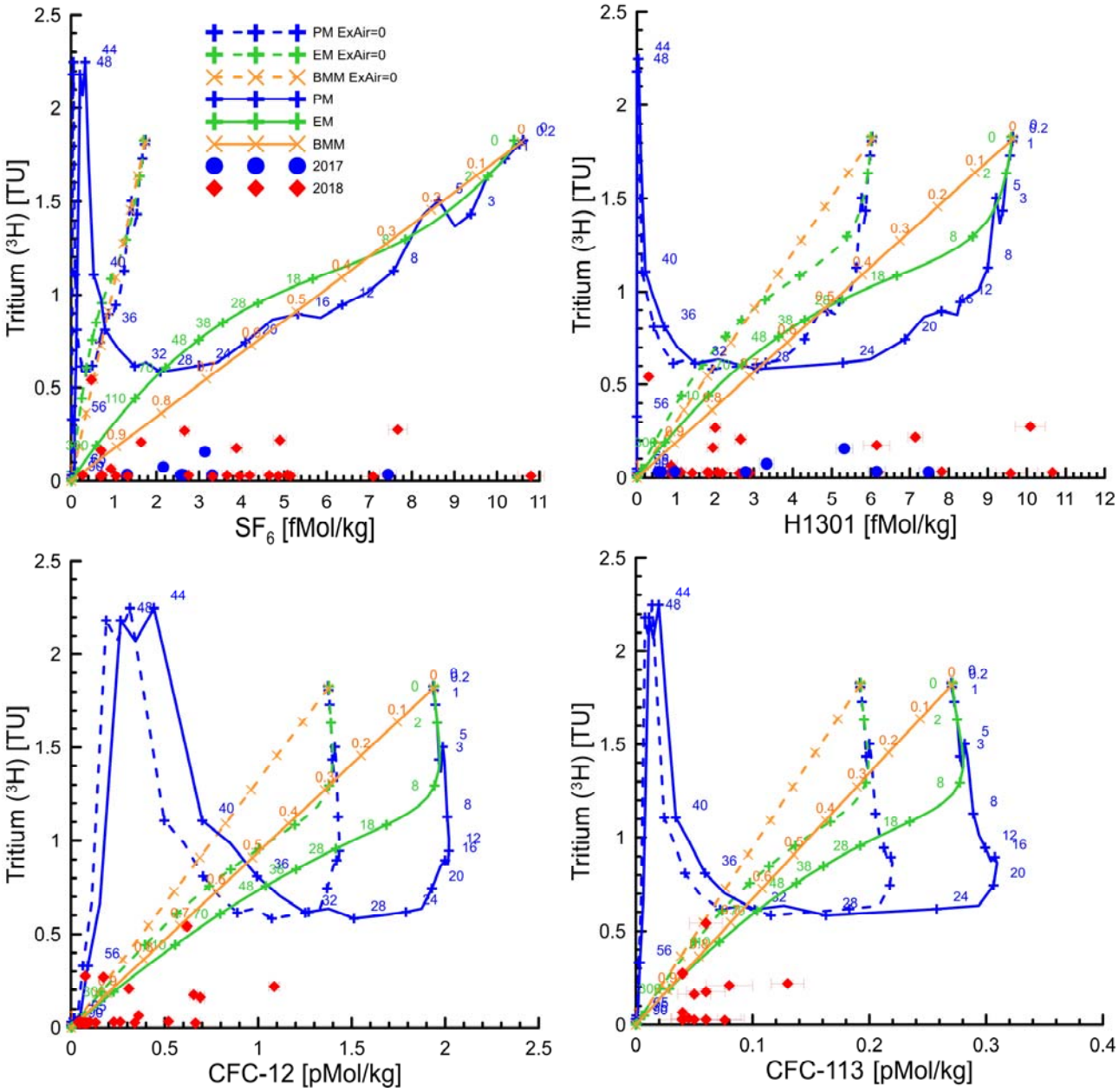

Figure 4.12 Cross plot of gas tracers versus ^{3}H.
Data points show measures values of each bore, lines show the expectation from different Lumped Parameter Models (LPM). Here PM is the Piston flow Model, EM the Exponential Model and BMM the Binary Mixing Model. Dashed lines are calculated with no excess air and solid lines with 25cc/kg excess air.

For the models to extend to the measured concentrations of SF_6 and H1301, excess air is needed up to concentrations of 25 cc/kg, which is higher than the up to 10 cc/kg indicated in the noble gas results (see below). To further explore the mechanisms that might drive the observed concentrations, the measurements of CFCs in samples from this trip provide opportunities for comparison extra to those made previously, i.e. SF_6 and Halon (Suckow *et al.* 2018). To further elucidate the mechanisms, similar cross plots are presented in Figure 4.13 for SF_6 versus the other gas tracers.

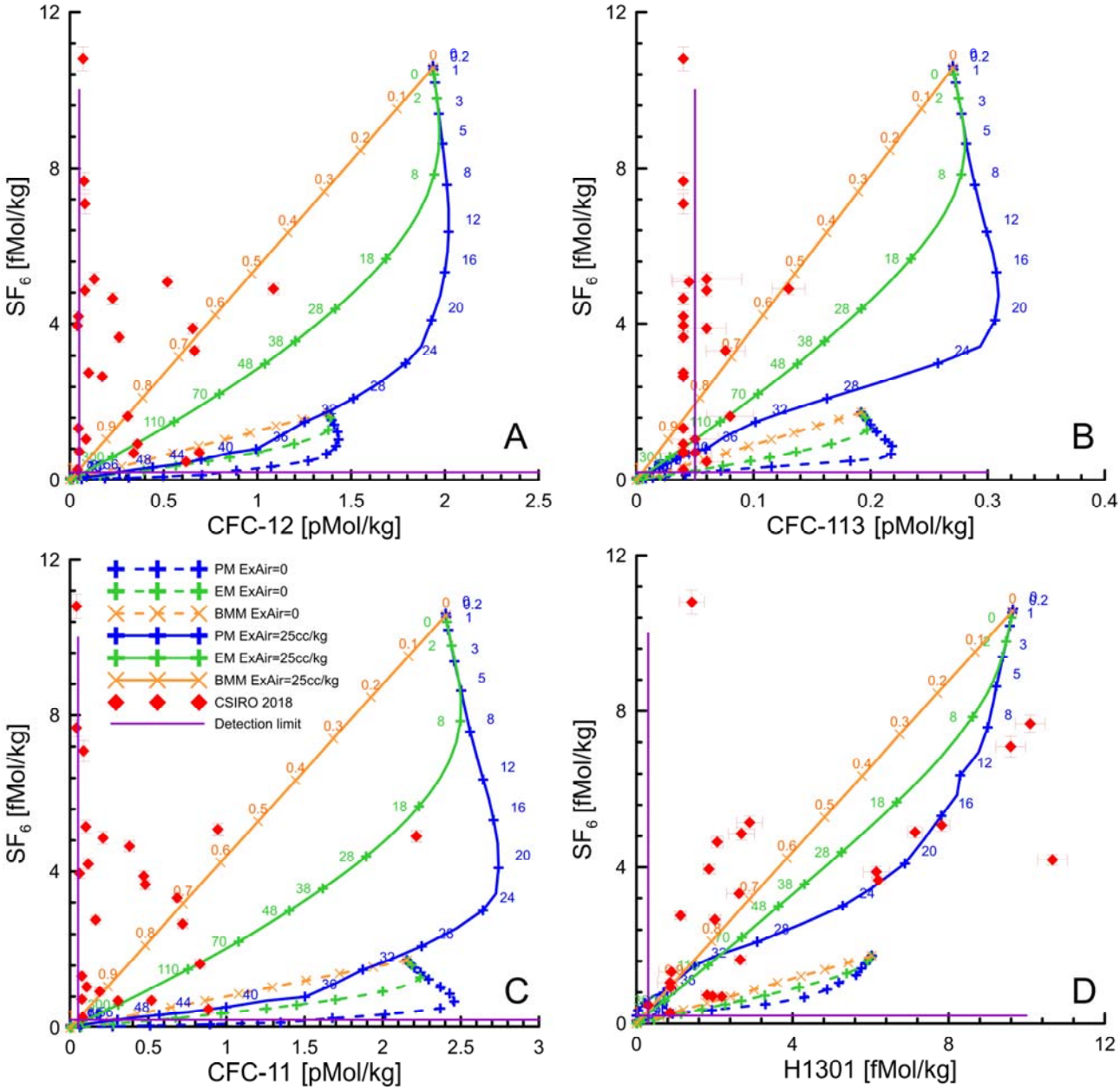

Figure 4.13 Cross plots of SF_6 versus other gas tracers.

These cross plots show that the measured SF_6 signals are higher than expected compared to the CFCs and come at least closer to the model lines for H1301. This is another indication that gas concentrations are influenced by processes other than solubility and water equilibria with air at the surface, and in the unsaturated zone during recharge events. Since the solubility of SF_6 is much smaller than of CFCs and H1301, excess air effects SF_6 much more than it does the CFCs or H1301, as outlined in more detail in the appendix. Furthermore, it is evident from plots A, B and C in Figure 4.13, that the CFCs are systematically lower than SF_6, which is also true for H1301 (the three cross plots of H1301 are not shown). This may be an indication of CFC degradation or absorption, as was observed already in earlier studies (Oster *et al.* 1996; Bauer *et al.* 2001; IAEA 2006; Archbold *et al.* 2011; Kashiwaya *et al.* 2015).

4.5 Carbon Isotopes

This study confirms the earlier findings (Suckow *et al.* 2018) that radiocarbon (^{14}C) in Total Dissolved Inorganic Carbon (TDIC – the sum of dissolved CO_2, HCO_3^- and CO_3^{2-}) generally increases with flow distance in the Cambrian Limestone aquifer (Figure 4.14). Reference point here is at lon 134.5° and lat -20.5°, which was chosen far enough out of the study area to get a similar distance relationship for all samples but is still in the area of the CLA. For ^{14}C a much bigger dataset is available than for the other isotopes, since several earlier studies also measured radiocarbon (Tickell 2004; Morris 2016; Tickell 2016; Suckow *et al.* 2018). Unfortunately, only the present study represents a dataset in which many environmental tracers were measured at the same sample, which means that mixtures of different water masses cannot be ruled out or quantified in the historical dataset. The increasing trend with flow distance is against the intuition that groundwater needs time to flow the total distance of many hundred kilometres within this formation, which would suggest a decreasing trend with distance, according to the black line in Figure 4.14. This counter-intuitive finding needs further corroboration with the aid of other isotopes in the TDIC system and other environmental tracers.

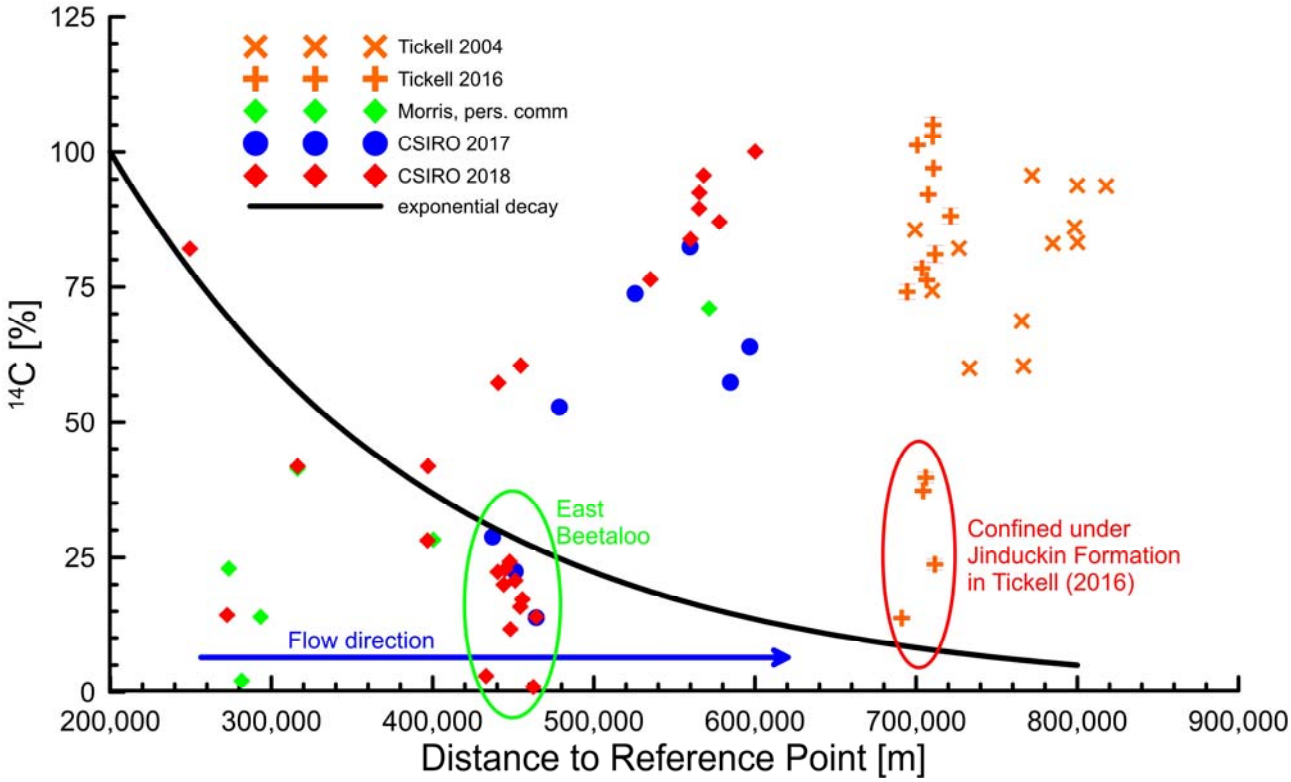

Figure 4.14 Historical and new ^{14}C data in the Cambrian Limestone aquifer along the flow transect.

Displaying the ^{14}C data spatially on a map reveals that the eastern part of the basin generally has lower ^{14}C values and contains the only values below 5%, these data around 450km flow distance are indicated by the green ellipse in Figure 4.14. The data in the Oolloo Dolostone are in a different geological formation and out of the scope of the map. However, the higher ^{14}C values are found along the Stuart Highway and west of it and closer to Larrimah or further north towards Katherine. The one sample with nearly 80% in ^{14}C at <250km flow distance is not from the CLA but from the Tomkinson Creek Beds.

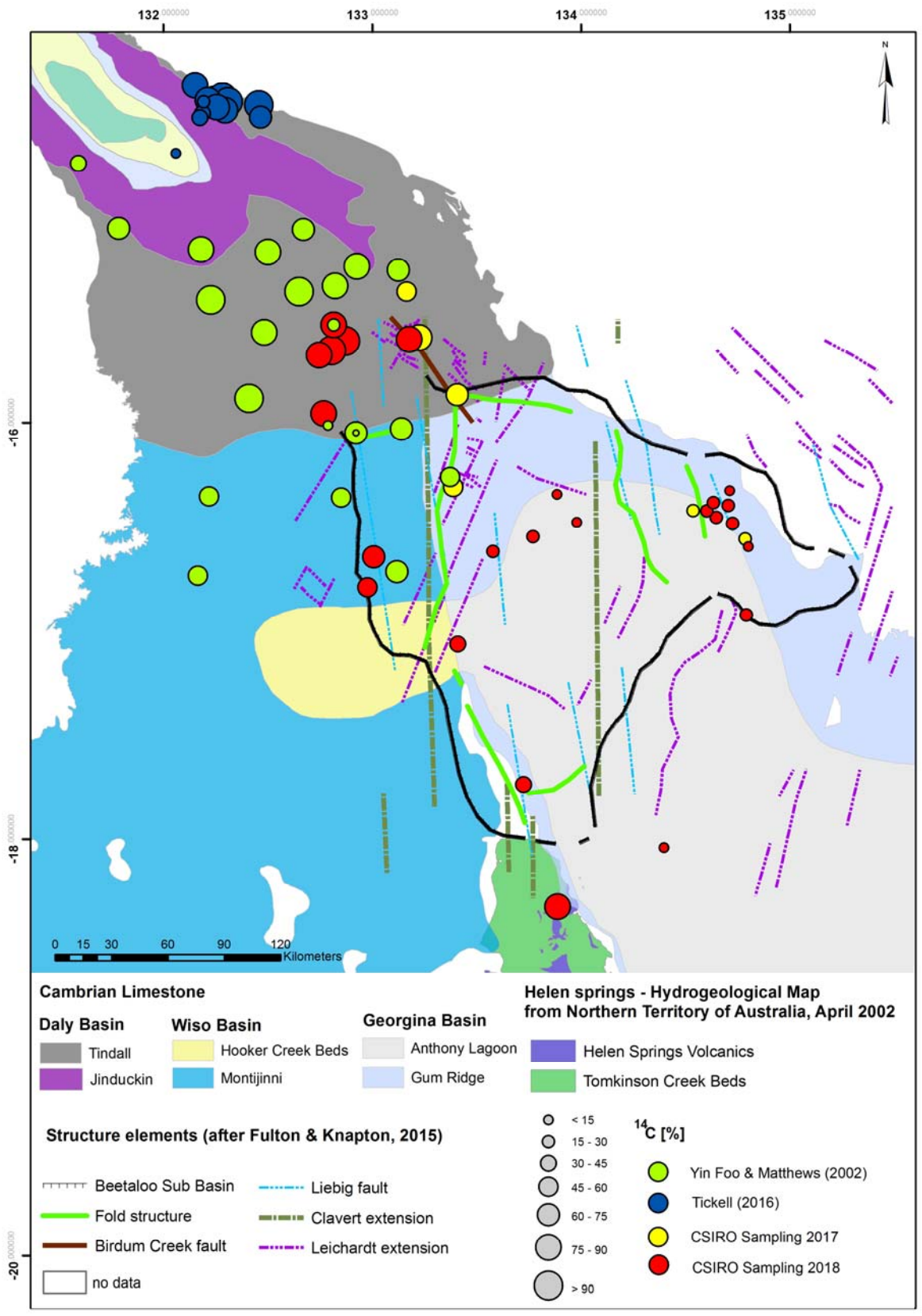

Figure 4.15 Map of historical and new ^{14}C data in the study area.

The anomalous findings in radiocarbon can be elucidated the same way as in (Suckow *et al.* 2018), by showing the cross-plots of TDIC, ^{13}C, ^{14}C and the absolute concentration of ^{14}C in atoms/L in Figure 4.16. The scatter of the new data is wider than previously, which is to be expected, since the earlier dataset had only eight samples close to Stuart Highway. Still most of the samples can be

explained with mixing of two different water masses having 1% and 100% in ^{14}C, respectively, as shown with the purple mixing lines. While the ^{14}C content of these water masses is unique between the two end-members, the TDIC and ^{13}C varies according to the position of recharge. The young component has TDIC values ranging from 3.6 to 8 mMol/L and $\delta^{13}C$ values from -12‰ to -15‰. This reflects the infiltration conditions in the north, where higher recharge is possible and allows for larger fluctuations of the groundwater table, dissolving carbonates under open conditions with tree and bush vegetation allowing for higher soil CO_2 concentrations with $\delta^{13}C$ values characteristic of C4 plants (Calvin photosynthetic cycle producing $\delta^{13}C$ values around -25‰). The old component in contrast has a lower range of TDIC (3.4 to 4.6 mMol/L) and more positive values in $\delta^{13}C$ ranging from -10‰ to -7‰, more characteristic of the savanna vegetation in the south with more grass in the plant biomass (Hatch Slack photosynthetic cycle producing $\delta^{13}C$ values around -13‰) (O'Leary 1981, 1988; Farquhar *et al.* 1989).

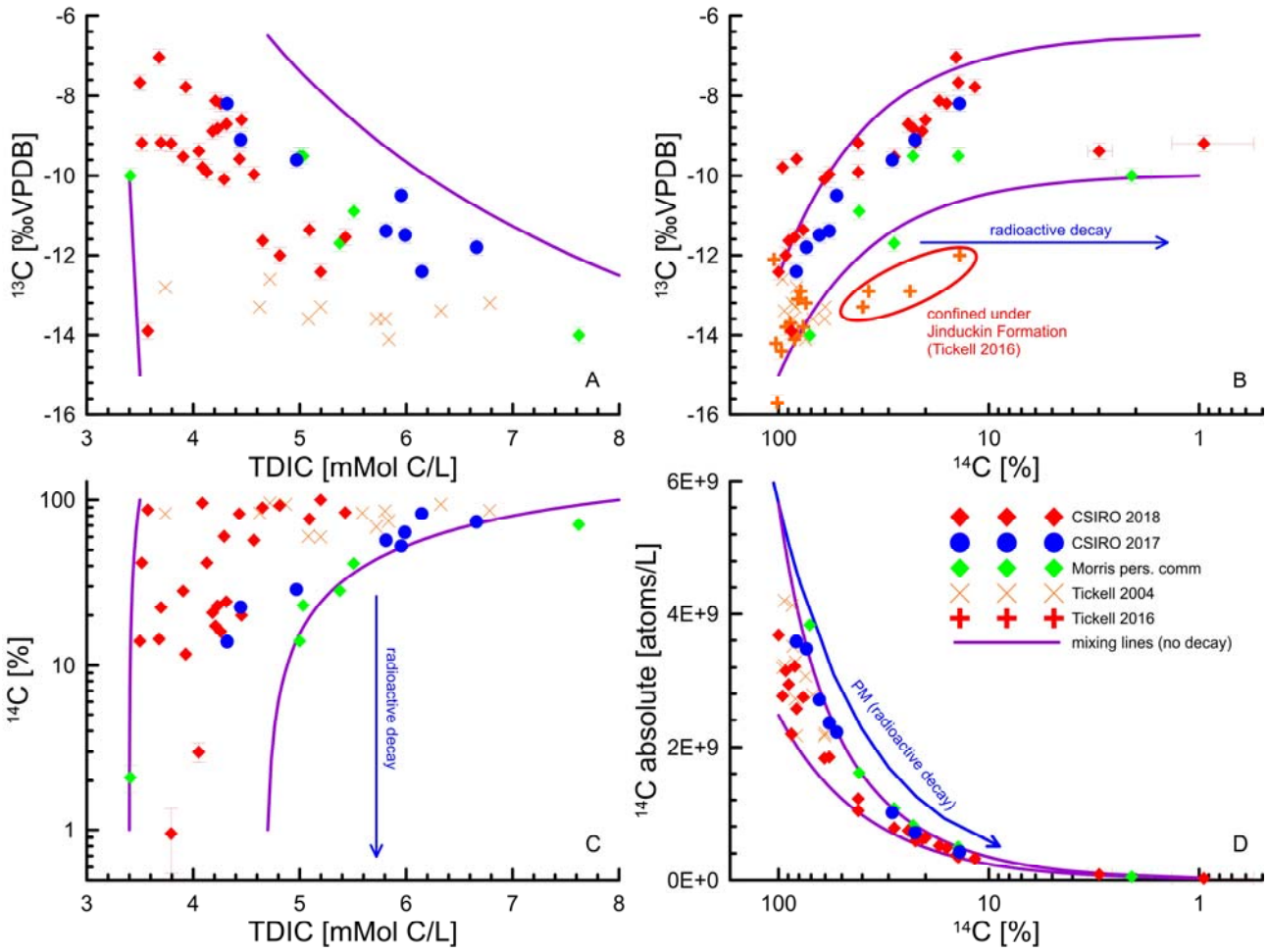

Figure 4.16 Cross-plots of TDIC, ^{13}C, ^{14}C and $^{14}C_{abs}$.

It is important to note that the mixing lines assume no radioactive decay and no aging of the water mass, just mixing between an *a priori* old water mass and young recharge. Radioactive decay in Figure 4.16 is horizontal towards the right in panel B (^{13}C is stable) and vertical downward in panel C. In panel D radioactive decay follows the blue line. Any aging of water is unequivocally detectable only if it leads out of the mixing range given by the purple lines. From this it is possible to conclude that those samples with highest TDIC show *no* significant radioactive decay, which

means they are “young” on the timescale of radiocarbon (that is: recharged less than 2000y ago). There is some ageing discernible in panel B for those samples from the areas confined under the Jinduckin Formation (Tickell 2016). Radioactive decay on the flow path cannot be excluded in the cross plots for those samples with low TDIC – but it would need a reasoning why only those samples with low TDIC show aging. Open questions are: where does the old water component originate and where does the recharge happen? The map of ^{14}C seems to indicate that the old waters originate mainly in the eastern and southern part of the basin. However, as mentioned in section 2.2, the total area of the CLA is potential recharge area, which is also confirmed by the environmental tracers for young water (tritium, CFCs, SF_6, H1301). Therefore, all areas of the CLA are potentially at risk to contamination from surface spills.

From the 2018 field campaign two samples exhibited radiocarbon below 10%, both were screened in the Gum Ridge formation and located in the north-east of the study area where the formation is overlain with thick cretaceous sand and clay. The other bores around this area had ^{14}C below 30%. These could indicate that the time it takes for water to pass through the Gum Ridge Formation from its areas of recharge to the south, throughout which it is overlain by the Anthony Lagoon Beds, is significant on the radiocarbon time scale (several thousand years). About these latitudes, the ^{14}C is higher to the west, with values about 50-60%, which may be indicative of the Montijinni Limestone not being overlain by the Hooker Creek Beds and therefore recharging more locally. Throughout the south there is mostly negligible tritium and that indicates the radiocarbon signals are not likely a bomb peak contribution, i.e. the CLA water is older than 55 years. In the quarter of the study area to the north west of Daly Waters the ^{14}C values are all above 50%.

Another open question is whether the high radiocarbon is really recharge. Gas exchange like observed for the modern tracers CFCs, SF_6 and H1301 would also influence the ^{14}C and ^{13}C values, since the soil air contains CO_2 that exchanges with the dissolved TDIC. And this process would be more efficient in the north, since the CO_2 concentration in soil air is higher due to denser vegetation.

4.6 Helium

Helium concentrations are observed to be up to a factor of 500 above expected solubility equilibria (Figure 4.17). He concentrations up to a factor of 2.5 higher than solubility can be explained by very high excess air as indicated by the heavier noble gases (10 cc/kg, green line in Figure 4.17). Because the ratio of the noble gas Ne vs. He does not fit to excess air, there must be an additional He source. This could be an admixture of an old groundwater component, e.g. from a deeper aquifer that is higher in helium concentration. The mixing ratio cannot be quantified as long as the helium concentration of this source is not known.

It also deserves notice that BET-LB025, Amungee NW-1 Water Bore 1 was sampled for noble gases in both CSIRO campaigns (2017 and 2018) and the results agree for all noble gas concentrations except argon to within 1.5%; for Ar the two measurements deviate 4.4% and for the Ar/N_2 ratio by 2.9%. This is an excellent reproducibility of the noble gas measurements.

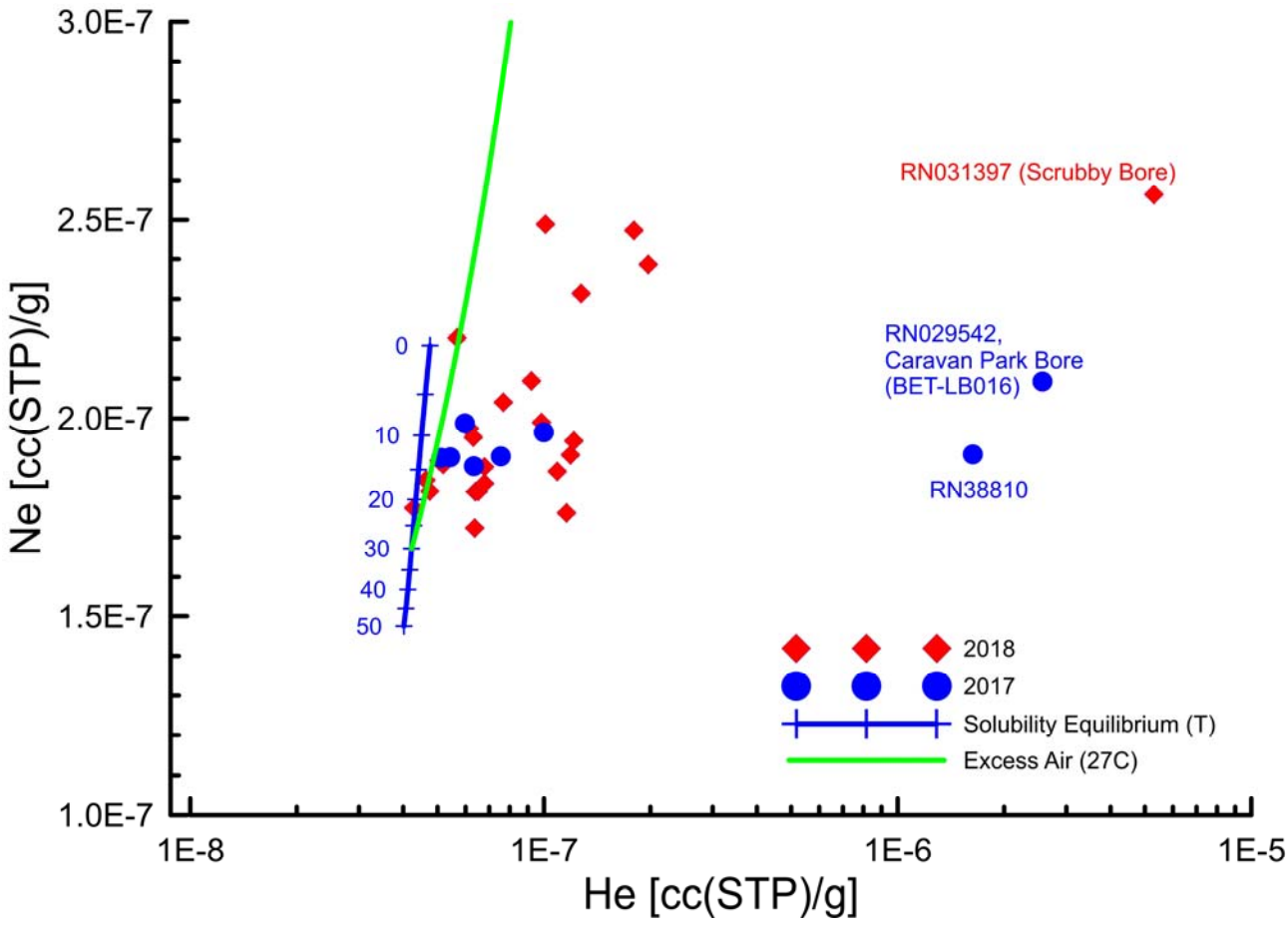

Figure 4.17 Helium -Neon cross plot.

Helium isotope ratios were measured for the first time on the samples of the 2018 campaign. Helium isotope ratios can be used to distinguish the origin of helium in groundwater – volcanic intrusions or deep connections to the mantle via fractures would result in higher $^{3}He/^{4}He$ ratios than crustal production from the decay of uranium and thorium. Some details on the usefulness of $^{3}He/^{4}He$ ratios can be found in the appendix. The Weise plot (helium isotope plot) in Figure 4.18 indicates that the samples plot along the line of terrigenic helium, which is a mixing line between atmospheric helium at solubility equilibrium and radiogenic helium produced in the crust origination only from the decay of uranium and thorium (Suckow 2013; Torgersen and Stute 2013). The sample with highest helium concentration (RN031397 Scrubby bore) defines the end-member at the bottom left of this mixing line in Figure 4.18; no sample shows any significant deviation to higher $^{3}He/^{4}He$ ratios. It can thereby be said that measured helium is only of radiogenic origin, i.e. there is no mantle component; this means the fractures in the area do not go very deep and are crustal faults, not due to mantle intrusions. There is also no indication of tritiugenic ^{3}He (helium produced from the decay of tritium), though this is not to be expected to be detectable on the Southern Hemisphere due to relatively low tritium concentrations, but this nonetheless offers some extra check for the data and methods.

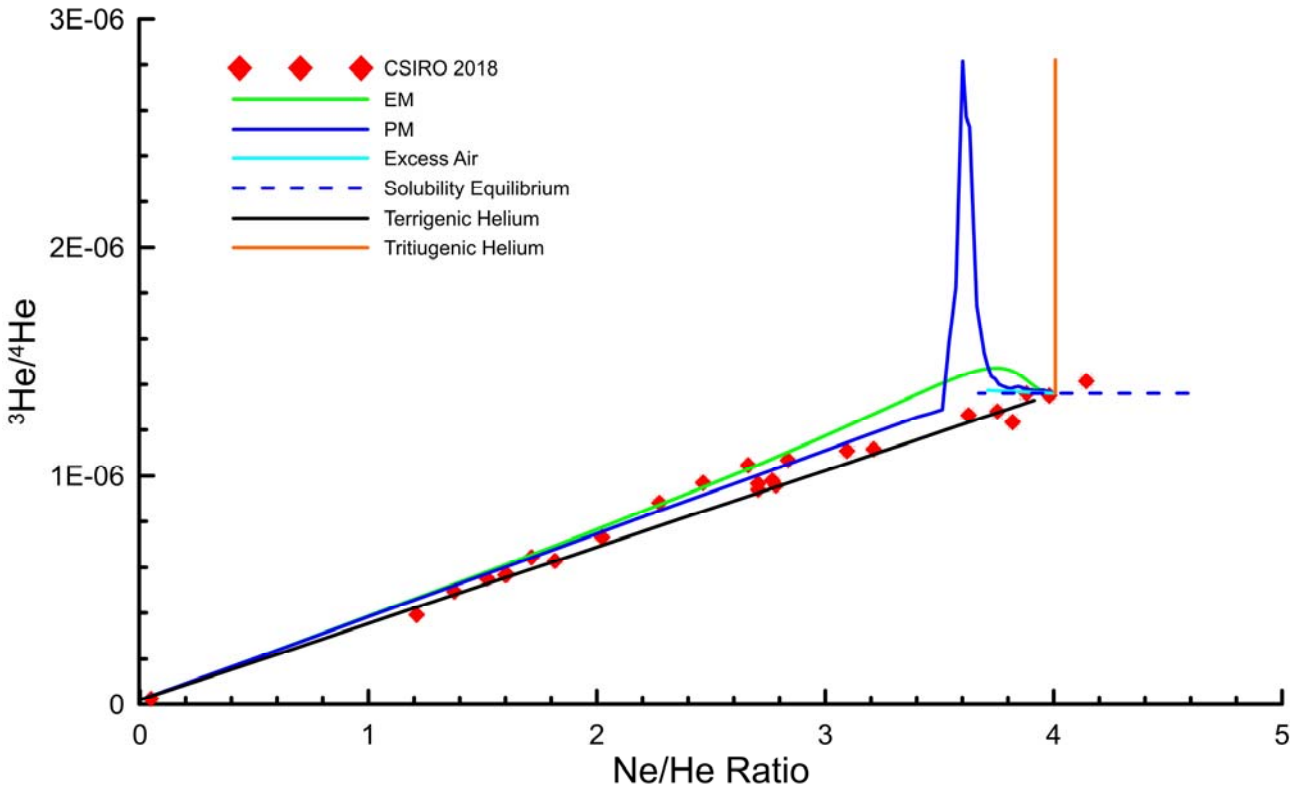

Figure 4.18 Helium isotope plot.

Both the map of helium concentrations in Figure 4.19 as well as the helium transect in Figure 4.20 show that no clear systematic increase of He with distance is discernible. Especially the three bores with very elevated helium stand out by a factor of ten compared to other bores with similar distance to the reference point at longitude 134.5° and latitude -20.5°. The sample with the second highest helium concentration (RN029542, Caravan Park Bore BET-LB016, see Figure 4.19) is very close (<5km) to a known system of faults within the Leichardt extension. This indicates that the high helium values come locally into the groundwater, possibly along fractures, and are not a development with time, which would show steady increase along the flow-path. This result confirms the ^{14}C-derived observation of mixing of old and young components, i.e. water does not age along the flow-path.

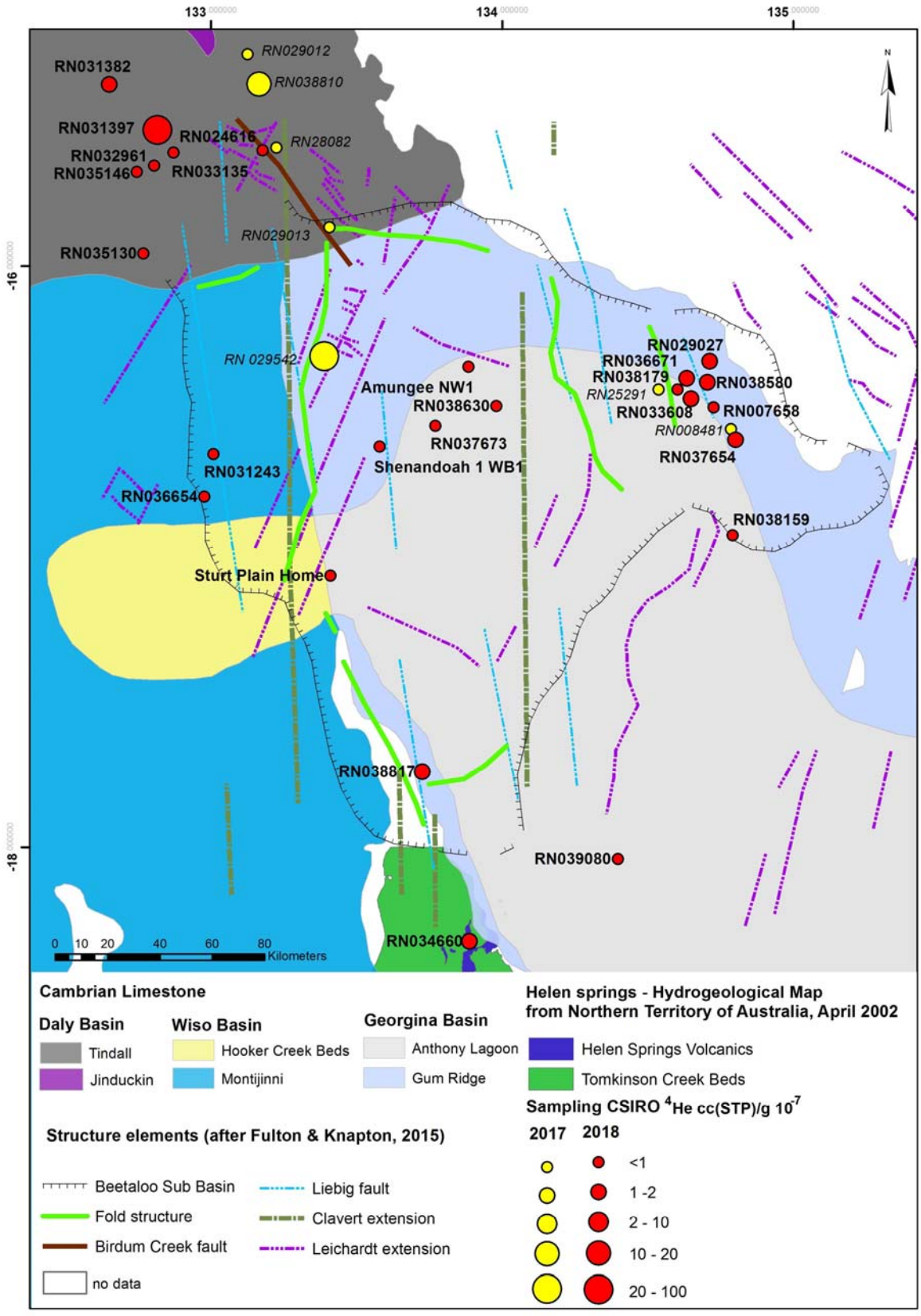

Figure 4.19 Map of helium concentrations.

The bore with highest helium concentration (RN031397 Scrubby bore) is open through approximately 160 m of basalt (Antrim volcanic) and 8 m deeper into the Bukalara sandstone. This

is an indication that one source of helium (and possibly the older water in the ^{14}C mixing relation) may be the formation directly underlying the Tindall Limestone. However, the bore also appears to be close (less than 10km) to an NW-SE undifferentiated fault (Fulton and Knapton 2015). Similarly, a map in Yin-Foo and Matthews (2000) shows a nearby unnamed NW-SE fault that offers a border between overlaying limestone on the west side, and upwards-displaced basalt on the east side.

If the helium originates from the formation directly under the CLA, the scatter of helium concentrations along the transect (lower dashed line in Figure 4.20 with a helium production of $5 \cdot 10^{-12}$ cc(STP)/(g·m)) may be helium production with a large scatter resulting from the distance of the lowest intake point of the well to the underlying formation. This can only be clarified with a detailed geological model determining the depth of the CLA under the sampled bores.

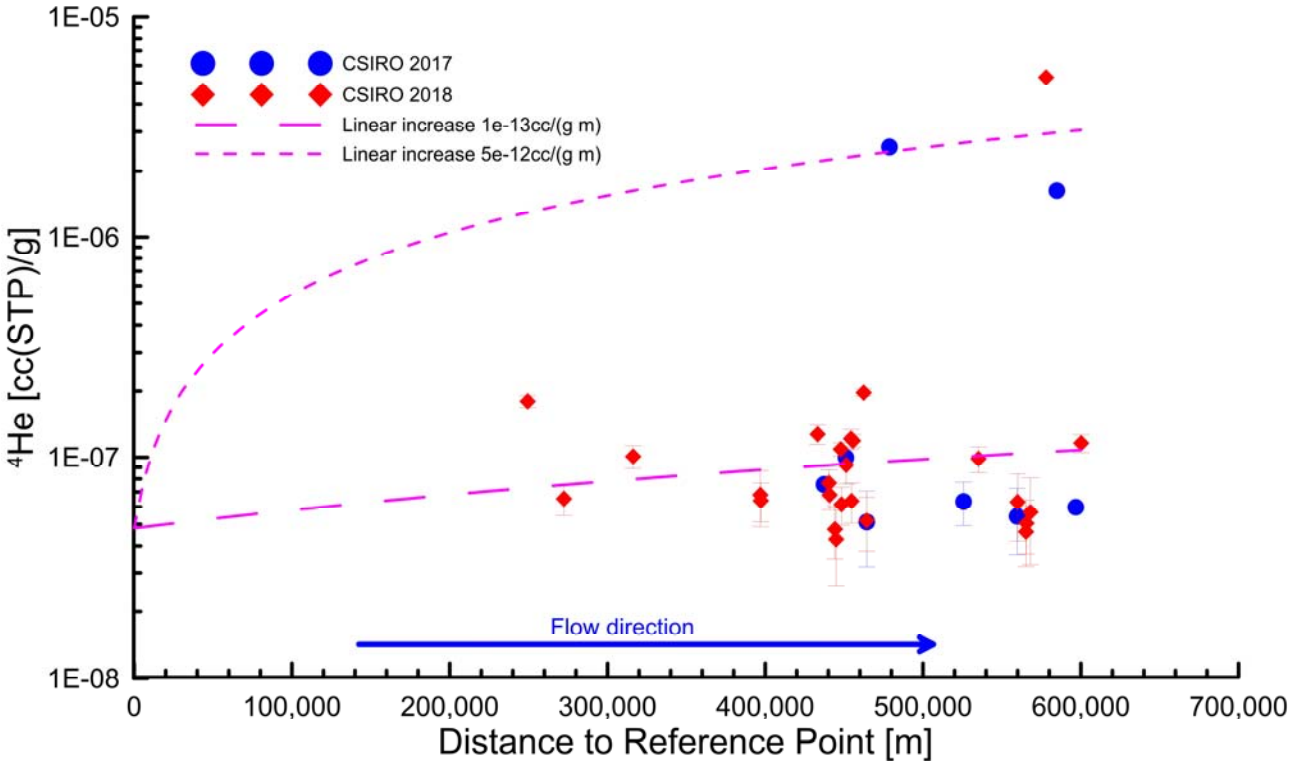

Figure 4.20 Helium concentrations along the flow line.

Low ^{14}C values show no correlation with high helium, nor high ^{14}C with low helium, as observed in Figure 4.21. This lack of correlation is another indication that ^{14}C and ^4He are not directly correlated with water age as defined via the distance along a flow path.

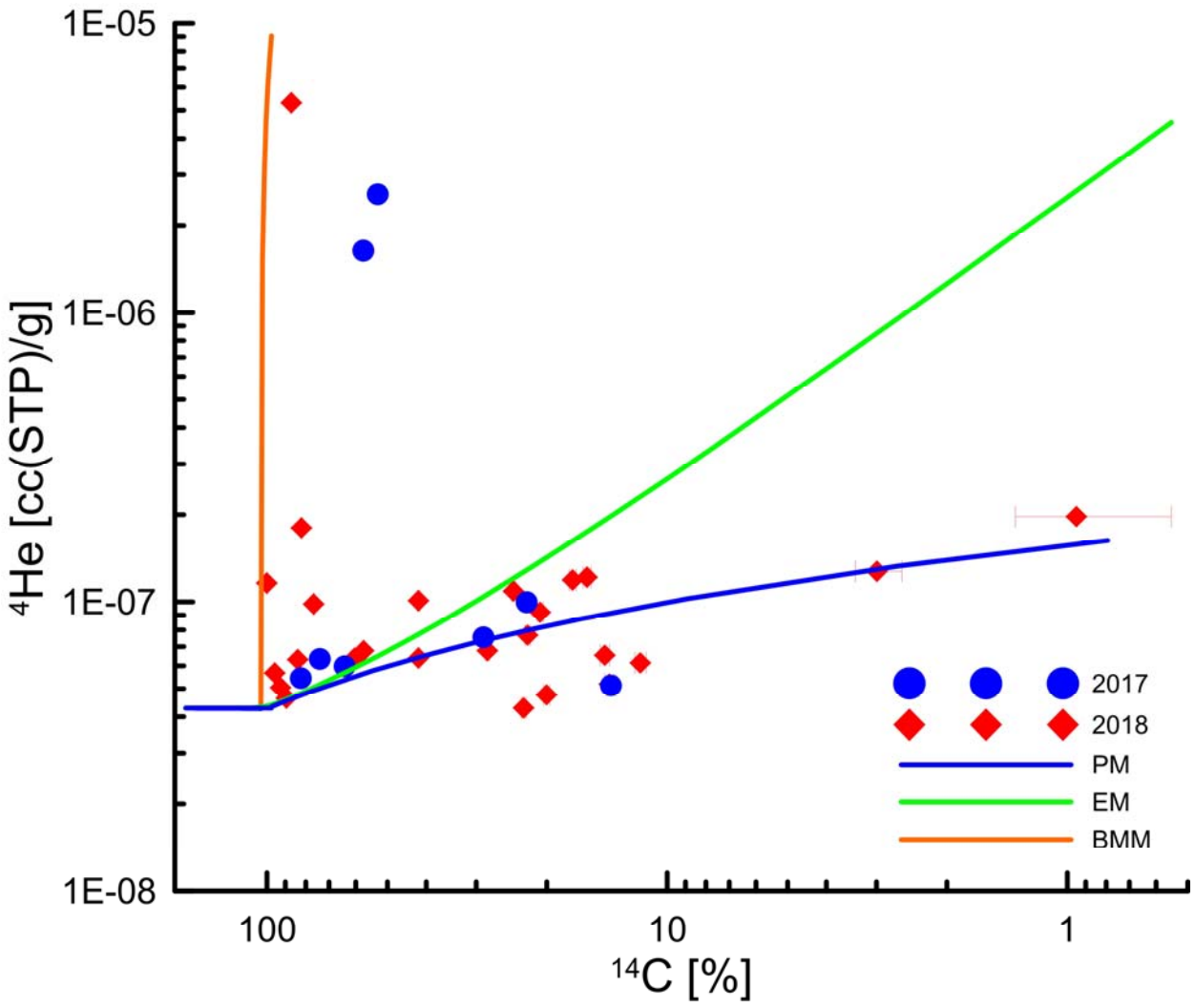

Figure 4.21 Cross-plot of helium with radiocarbon.

4.7 Heavy Noble Gases and Nitrogen

Measurements of the noble gases provide information that is least likely to have any interference by chemical reactions. Furthermore, the heavy noble gases (Ar, Kr and Xe) provide information about the infiltration temperatures. Xenon has the largest variation of solubility (and hence concentration) with temperature and therefore provides the best estimate for infiltration temperature. Neon has the smallest variation of solubility with temperature and therefore provides the best estimate for excess air. In most applications the single noble gas concentrations are converted into noble gas recharge temperatures and excess air using a non-linear fitting algorithm (Jung and Aeschbach 2018) and different model assumptions about the genesis of the excess air and infiltration. While this is an option, it obscures the insight into the different effects influencing the single noble gases. In this aquifer system we have previously observed various effects upon gas tracers related to excess air and different transport and equilibration processes of air (Suckow *et al.* 2018). Hence, we plot different combinations of the heavy noble gases, in part to see if effects are evident on the different noble gases and modelled temperatures, instead of just reporting one noble gas temperature at each bore derived from all the noble gases.

The heaviest noble gases krypton and xenon, which have the highest variation of solubility with temperature, indicate recharge temperatures between 30°C and 42°C (panels A and B in Figure

4.22). There is excess of Kr compared to the Xe especially for the higher infiltration temperatures, i.e. samples are to the right of the solubility equilibrium line in panel A. Those samples exhibiting highest Xe and Kr amounts are generally from the south of the study area. The three bores featuring the lowest Xe and Kr amounts are from the west. The Xe vs. Ne plot (panel B in Figure 4.22) shows significant excess air contributions for a lot of bores, as the Ne concentrations are all to the right of the solubility equilibrium line. From this plot excess air is up to 6 cc(STP)/kg, whereas Kr and Xe (panel A in Figure 4.22) indicate much higher values of excess air of >10 cc(STP)/kg.

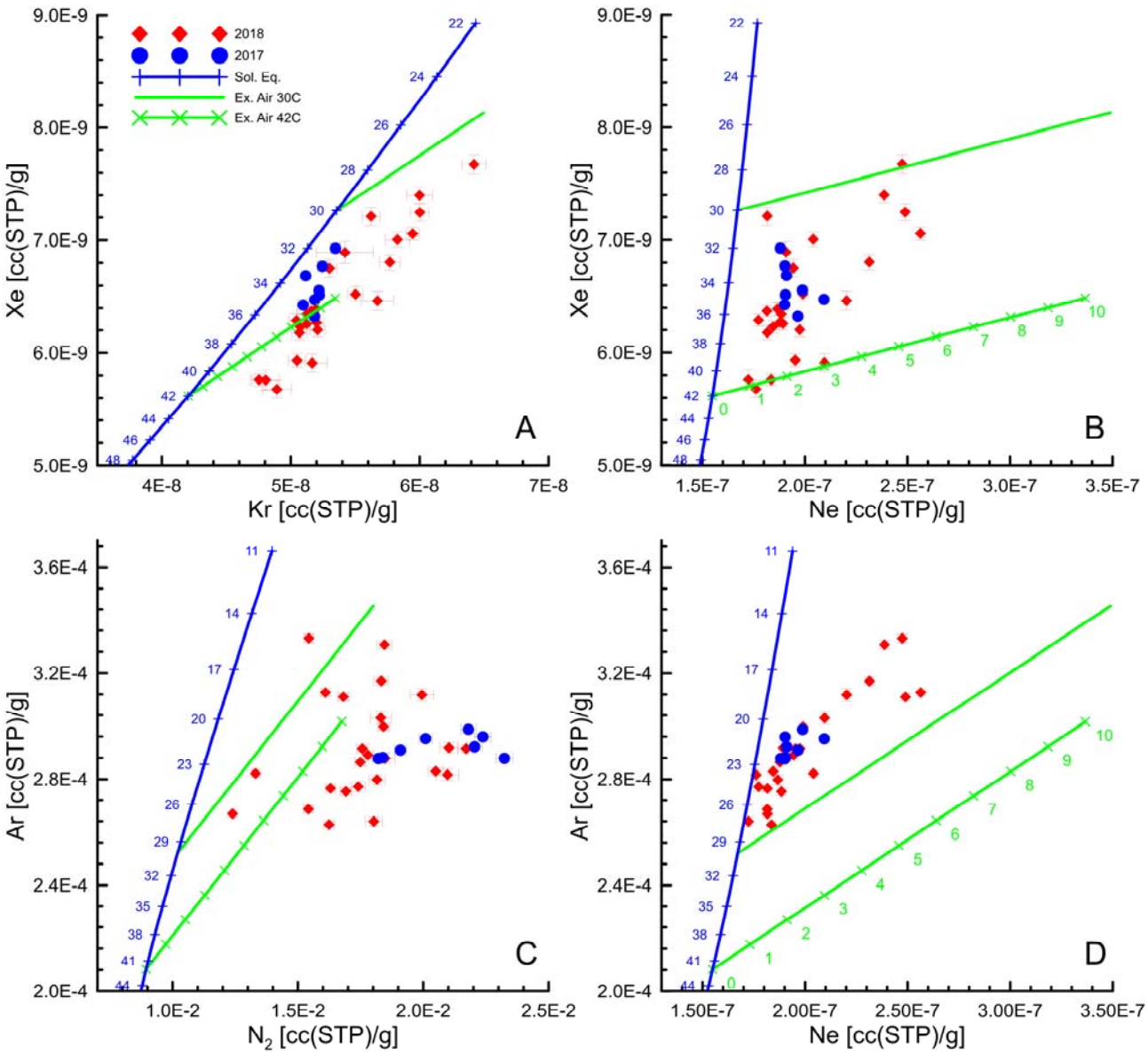

Figure 4.22 Cross-plots of the noble gases Xe, Kr, Ar and N_2.
Blue lines show solubility equilibrium of the noble gases, green lines show the addition of up to 10cc(STP)/kg excess air to water equilibrated at 30°C and 42°C.

The plot of Ar vs. N_2 shows a very significant excess of nitrogen up to a factor 2-3 above the concentrations to be expected from solubility and excess air in comparison with the other noble gases (panel C in Figure 4.22). This is unexpected, as the argon concentrations are also in excess as compared to neon: panel D in Figure 4.22 shows all samples above the excess-air line that

indicates (starts at) the lowest acceptable infiltration temperature derived from the Xe-Ne plot at 30°C (panel B).

Excesses in nitrogen – which is not a noble gas and can be produced by de-nitrification in the aquifer – might originate from termite mounds, which are abundant in the study area and known to produce nitrate naturally (Stadler *et al.* 2008; Stone and Edmunds 2014).

Figure 4.23 Termite mounds and small natural sinkholes in the study area.

5 Discussion

This chapter attempts to summarize the results for hydrochemistry and environmental tracers and to derive a conceptual model of groundwater movement and recharge that explains the phenomena with least internal contradiction. While very rough estimated values for recharge are derived, a detailed spatial modelling of recharge and flow is beyond the scope of this report.

- The seemingly contradictory and anomalous tracer results can be explained with a new conceptualisation of recharge.
- Tritium in groundwater indicates localized and fast recharge through sinkholes.
- High concentrations of CFCs, SF_6 and H1301 in all wells are probably not indicative of recharge but instead of gas exchange caused by water-level fluctuations induced elsewhere by localized recharge.
- The gradient of increasing ^{14}C in flow direction indicates recharge and admixture of young water to an old component. Nearly all sampled groundwaters can be described as such binary mixture. The origin of the old water component remains unclear and can be either from the south or from deeper layers.
- Elevated helium can be from in-situ production or from exchange with layers underlaying the CLA. The three samples with high helium indicate flow from below, probably along fractures. The amount of this inflow cannot be quantified without knowing the helium concentration in those formations.
- Both the open questions for ^{14}C and for helium cannot be answered without tracer measurements in aquitards and aquifers below the CLA.
- There is uncertainty about the source of modern ^{14}C, including from recharge (input on time scales of hundreds of years) and gas exchange (more recent input). Resolving this requires a unique tracer (^{39}Ar) to assess residence times between those of tritium and ^{14}C while not being influenced by excess air.
- Using only tritium to estimate recharge over the last 50 years results in an estimated average value between 76 mm/y and 190 mm/y.
- This estimate is valid is valid only for those locations where recharge through sinkholes happens.
- An estimate of total recharge over the CLA needs mapping of sinkhole locations and of the extent to which tritium penetrates the aquifer.

5.1 Groundwater evolution in the Beetaloo Basin

This section interprets present knowledge about the tracer values to derive a qualitative model that can explain the seemingly contradicting results of tritium and the gas tracers. It involves processes such as localized point recharge through sinkholes and gas exchange that is triggered by water-level fluctuations over the whole area.

5.1.1 Conceptualization of recharge and gas exchange

As discussed in IAEA (2006), effects of excess air, particularly upon molecular gases such as CFCs, SF_6 and H1301, can be expected to be larger:

- at higher recharge temperature
- for less soluble gas, e.g. Ne or SF_6 rather than Xe or CFCs and H1301
- for younger water rather than for older water (Busenberg and Plummer 1992).

The noble gas results indicated that this region exhibits high recharge temperatures. Between 40°C and 10°C there is a four-fold difference in CFC equilibria concentrations, thus it is reasonable that the excess air effects we observe here are more extreme than those observed in more temperate climates, e.g. most southern regions of Australia or New Zealand.

Stute and Schlosser (1993) and Visser *et al.* (2007) observed via noble gas measurement and interpretation that excess air could be fractionated, i.e. a change of the concentration ratios of the

noble gases as compared to solubility equilibrium and unfractionated excess air due to diffusion and loss of the light gases to soil atmosphere, whereas the heavy noble gases are retained. A different model has trapped air bubble(s) partially dissolving in groundwater under equilibrium conditions in a closed system (Aeschbach-Hertig *et al.* 2000; Aeschbach-Hertig *et al.* 2008) – and because heavy noble gases are more soluble in water these become enriched. Thus, it is possible that over time air that is trapped underground becomes more concentrated in the less diffusive gas such as Xe, Kr, CFCs, SF_6 and Halon. With recharge events the molecular gases equilibrate with water and receive a fresh load of excess air, since water level fluctuations can provide high pressure, e.g. 100 mbar of pressure per metre of raised head, that can drive gas molecules into solution in the water. Hence, the concentrations of the least diffusive tracers (Xe, SF_6) are higher than might be expected compared to other tracers (He, Ne). This would explain why the excess air calculations that rely on the concentrations of Ne gave relatively lower values than for Kr vs. Xe or SF_6.

Perhaps exacerbating the excess air scenario, which occurs during recharge events, we can also consider the effects of barometrically driven exchange of air into the soil and aquifer system. Pressure fluctuations of external atmosphere and convection driven by temperature differences can force air to flow into karst systems, within times scales of minutes to days (Badino and Chignola 2019). Anecdotal reports in the region include blowing and sucking of air at bores. Thus, fresh air can be provided into the system within short timescales.

The molecular gas tracers are evidently higher in concentrations than what is expected compared to tritium. During recharge the tritium signal is introduced into the aquifer as part of the water molecule. On the other hand, the gas tracers are included during recharge via solubilisation in the water, with concentrations determined by gas-liquid equilibria, and mechanisms such as inclusion of excess air.

This leads to the following conceptual model of recharge and gas exchange explaining qualitatively the observed tracer patterns (Figure 5.1):

1) During the heavy monsoon rains enough precipitation reaches the ground to flow overland to the sinkholes. That there needs to be a certain threshold for recharge to occur is indicated by the stable isotopes.
2) Recharge infiltrates through the sinkholes into groundwater and creates local "groundwater mounds" around the sinkholes, which enriches the groundwater locally with tritium (as part of the water molecule) and gas tracers (second panel of Figure 5.1).
3) After these local recharge events, the groundwater mounds disperse their pressure (not their water) into the whole groundwater body. This leads to a general increase in groundwater level in the whole area which entraps air, leading to excess air and a supersaturation of gas tracers in groundwater (third panel of Figure 5.1).
4) During the dry periods before the next recharge event, the fastest diffusion gas tracers, like helium and neon, partly re-equilibrate with soil air. The slowest diffusing tracers, like Xe and SF_6, stay in supersaturation.

This conceptual model can explain *qualitatively* a pattern of groundwater with low tritium but high gas tracer values. It can also qualitatively explain the observed enrichment of heavy gas molecules such as SF_6 and Xe. Whether this model is *quantitatively* accurate would need a detailed numerical

model of gas diffusion and water transport processes that are beyond the scope of the present tracer study. However, this conceptualization has several consequences:

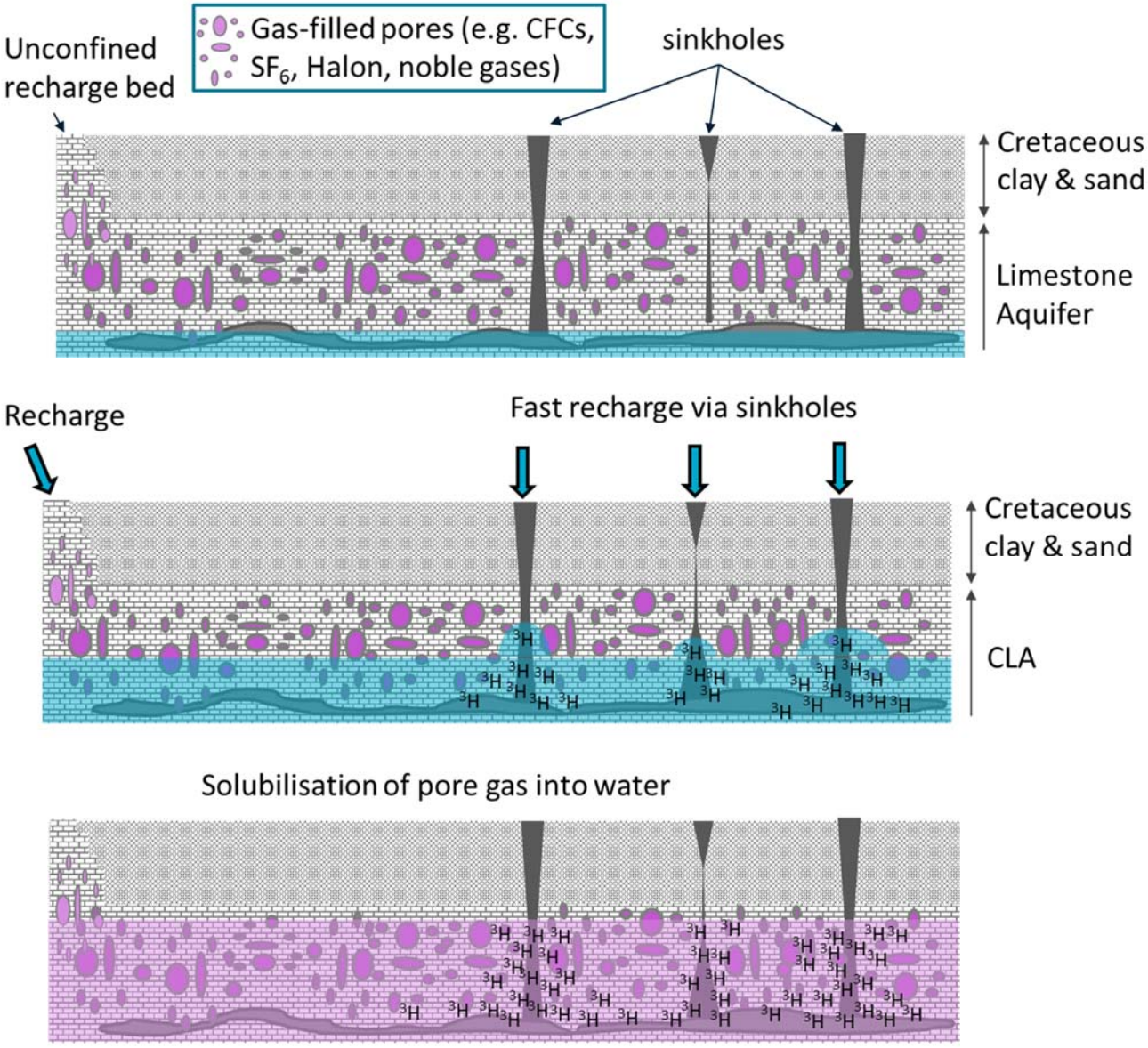

Figure 5.1 Conceptual model of recharge and water level fluctuations explaining low tritium and gas tracer findings. Top panel: After extended dry periods (season or multi-year) water table is low in the CLA. Pore space and voids in the unsaturated zone are in contact with modern air and CFCs, SF_6, H1301. Middle panel: After a precipitation event water infiltrates (and with it tritium as HTO) localized at the locations of sinkholes, creating a local pattern of ^3H in groundwater. Bottom Panel: Once the groundwater table re-equilibrates (time scale of weeks to months) also some pore space and voids are flooded, contributing CFCs, SF_6 and H1301 into groundwater in the whole area (pink colouring) whereas the tritium stays local.

- The gas tracers (CFCs, SF_6 and H1301) are not a reliable indicator of recharge, because they reach the groundwater just by water-level fluctuations and the recharge may occur elsewhere.
- Tritium is an indicator of groundwater recharge, and only where tritium is found the real recharge occurs (that is: on a fraction of the total area).

- Chloride also reaches the water table together with recharge, but the amount of chloride may be higher in recharge than it would be if infiltration happens over the whole area (the overland flow in 1) dissolves Cl from dry precipitation and focuses it into sinkholes). Similarly nitrate (from animal middens) may be concentrated into the recharging water.
- The described process of gas exchange can transport also modern CO_2 from root transpiration in soil air into the groundwater. Thus, it may be (possibly only partly) responsible for the observed mixing relation between modern TDIC (with 100% in ^{14}C) and the old groundwater component.

Since according to this conceptual model only tritium and possibly chloride are reliable indicators for actual groundwater recharge the following discussion will use only these two compounds.

5.2 Recharge estimates

5.2.1 Chloride mass balance

The recharge rates estimated with the chloride mass balance vary widely between 25 mm/y and less than 1 mm/y, which reflects the karst nature of the Beetaloo Sub-Basin. Despite the high variability, there is a clear spatial trend of increasing recharge from south to north (Figure 5.2). The average recharge rates for the three latitudinal sections from -18.5° to -17°, -17° to -16°, and -16° to -15° are 1.7±1.1 mm/y, 5.0±2.0 mm/y, and 7.4±8.4 mm/y, respectively. Finally, Figure 5.2 shows that there is a wide range in recharge rates in the northernmost part (<16° North), which reflects the two distinct clusters in the east and west of the Tindall Limestone identified in Figure 4.2. Calculating separate averages for the western and eastern Tindall results in recharge rates of 12.8±9.1 mm/y and 2.0±0.3 mm/y, respectively.

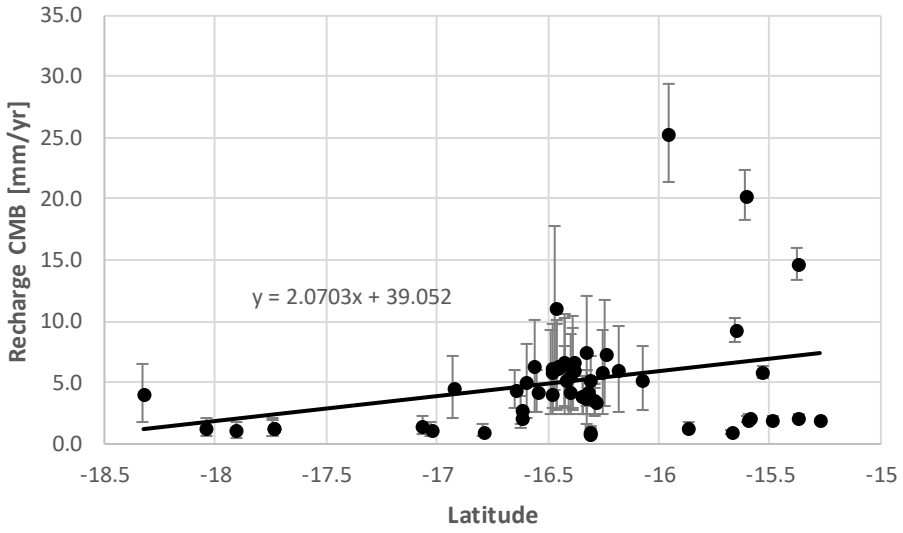

Figure 5.2 Groundwater recharge estimated with the chloride mass balance method as a function of the latitude of the sampling locations.

5.2.2 Recharge Estimation from Tritium

As discussed above only tritium is used as the tracer for characterising recharge of young waters. This uses the peak of tritium in precipitation related to nuclear bomb testing in the 1960s and its half-life of 12.43 years. Use of unsaturated zone tritium profiles to determine groundwater recharge rates is more common in arid and semi-air regions (Phillips *et al.* 1988; Suckow *et al.* 1993; Cook *et al.* 1994). Tritium has previously been used in different regions across Australia to determine recharge rates (Allison and Hughes 1975; Allison *et al.* 1985; Cartwright *et al.* 2007; Cartwright and Morgenstern 2012; Cartwright *et al.* 2017; King *et al.* 2017). Also Cook and Walker (1996) compiled studies where recharge estimates were obtained with both tritium and chloride.

The choice of tritium is framed by the general age information across the region, such as no aging being indicated by the ^{14}C, and the other 'young' tracers showing complex behaviours heavily influenced by gas exchange and excess air that make their results unsuitable for determining a flow velocity. However, the standard method on the northern hemisphere to calculate a tritium-^{3}Helium age and to derive recharge from a depth profile of such ages (Solomon *et al.* 1995; Houben *et al.* 2018) is not possible here because 1) the tritiugenic helium is not easily detectable since the anthropogenic tritium fallout is much smaller and 2) since one-location depth profiles from multilevel wells in the CLA are not available under the present infrastructure situation. Using tritium alone either also needs a high-resolution depth profile in the aquifer or in a lumped parameter model approach results in enormous ambiguity in the mean residence time.

There are two techniques used here to estimate the recharge, similar to those outlined in Phillips *et al.* (1988) and other references mentioned above.

1.) Integrate the measured tritium signals and compare it to a historical input, i.e. a mass balance;
2.) Use the peak of the tritium signal from a depth profile over an area to determine the depth in which the recharge of 1963 is found in the profile and divide the total cumulative water in the profile above this depth by the time difference of 55 years between sampling (2018) and tritium peak (1963).

5.2.2.1 Historical Tritium and Rainfall Records

We approximate the location for the area of significant measured tritium values to be Larrimah, that is 1000 km north of Alice Springs and 500 km south of Darwin. The Bureau of Meteorology has published rainfall records for Larrimah; the average rainfall for the period 1963-2018 was 860 mm/y (Figure 5.3 top panel). We use the data set for tritium measurements of rainfall from Darwin rather than Alice Springs because it is much more extensive. Since 1990 the trend of the Kaitoke tritium dataset was used, where a linear scaling was determined by comparing it with the Darwin data set from 1982-1989 (Figure 5.3 middle panel). The raw tritium signal is relatively flat since 1990, in recent years it is about 2.7-3.2 TU. Also plotted is the amount of tritium that has rained, which was calculated by multiplying the monthly rainfall by the measured tritium value and then summing into yearly contributions. The total rained tritium since 1963 decay corrected until today is 53.7 TU·m.

It is evident from the decay corrected tritium (Figure 5.3 bottom panel) that it would now be difficult to distinguish between water from the bomb peak water (1960-1980) and modern water (infiltrated before 2005), as the TU·m/y are similar. It might be possible to distinguish the low tritium gap for the period 25-50 years ago (1980-1990) within a depth profile, as the tritium signals might be approximately three to five times less than modern or bomb peak water.

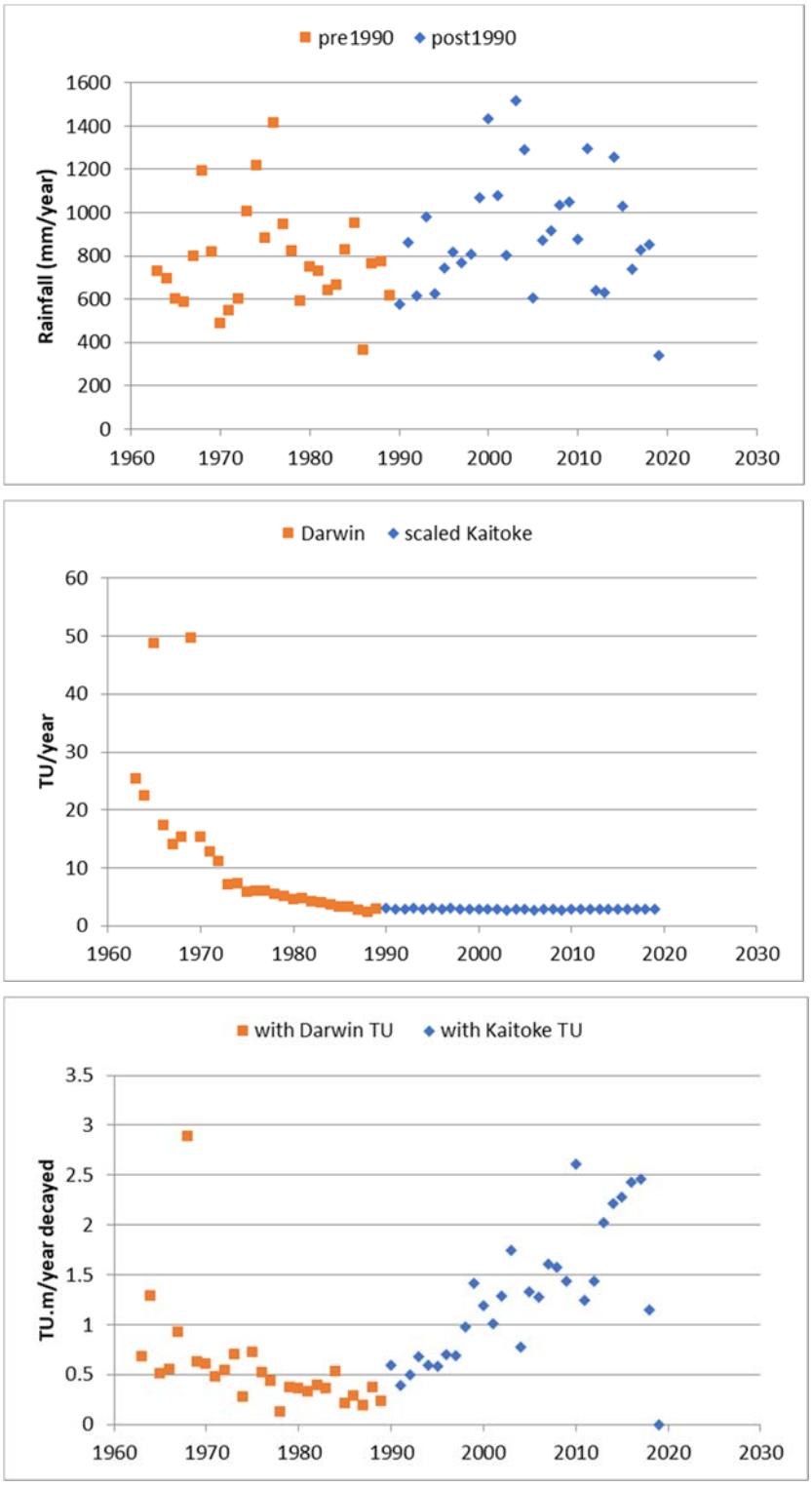

Figure 5.3 Rainfall data at Larrimah, tritium from Darwin.
Data are calculated and decay-corrected TU·m/y

5.2.2.2 Integration of tritium signals (Mass Balance)

The basic form of the integration method is to determine (e.g. equation 13.1 in Cook 2000):

Recharge (or water flux below soil surface) = *B/A* = %rain

Where:

A is the water input = $Input_{Water} = \int TU \cdot rain \cdot e^{-\lambda t} dt$ (will give TU·m)

B is the signal today = $Signal = \int_0^{\infty} \theta \cdot TU \, dz$ (will give TU·m)

This method requires the integration of the tritium signal over time, i.e. for the years before the present.

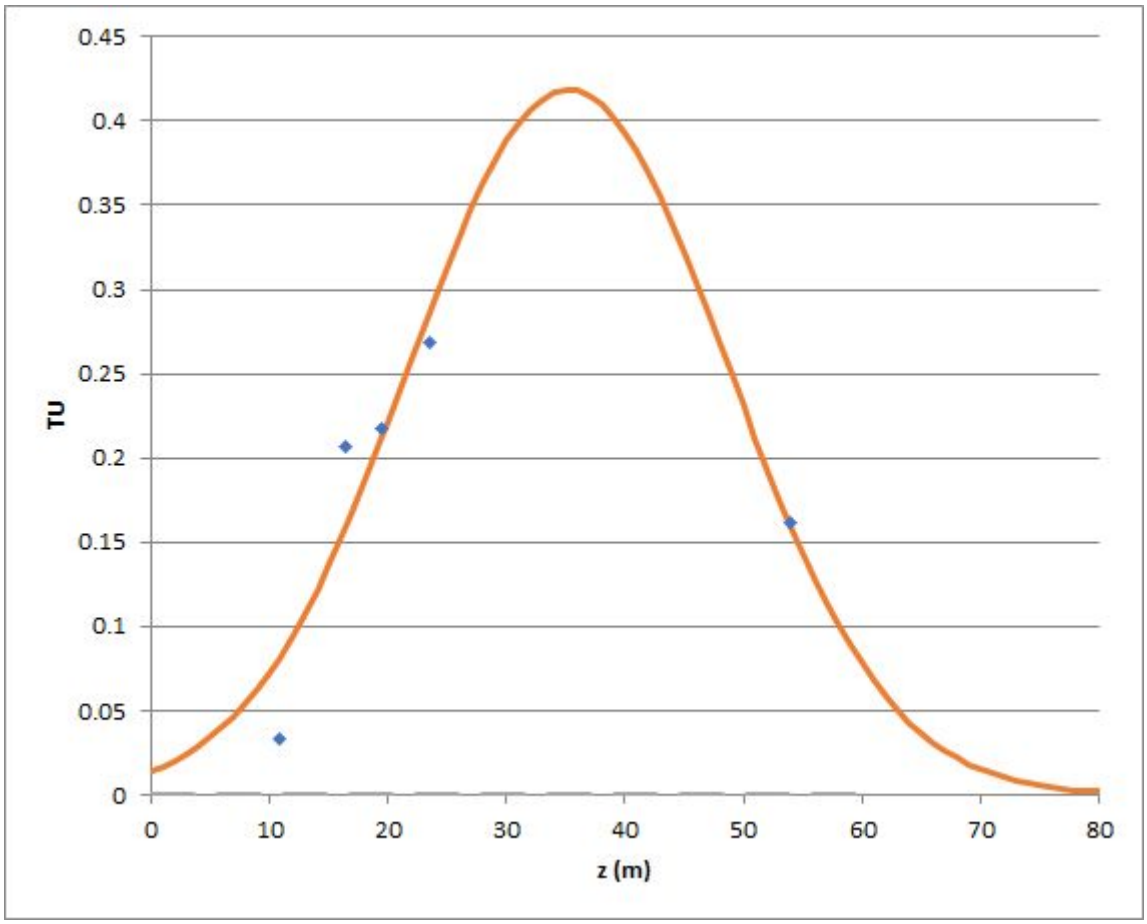

Figure 5.4 Plot of a Gaussian profile fitted to integrate the measured tritium signals.
z is the depth screen midpoint below water level, peak position is at 35 m below groundwater.

For the integration we fit a gaussian profile of the form $f(z) = ae^{-\frac{(z-b)^2}{2c^2}}$, where a is the height of the peak, b is the peak position and c is the standard deviation, z is the depth of the screen midpoint below the water table. The profiles were fitted by minimizing the squared sum of the differences between the measured data points and ordinate for each z. We focus on the peaks in the NW quadrant of the study area, i.e. the Tindall Limestone, and within those with screen lengths less than 10 m. An integration across all points yields 15 TU·m. Multiplying by a maximum porosity value of 0.3 and dividing by the rain input since 1963 (53.7 TU·m) gives a recharge value of 8% of rainfall. Multiplying by the average rainfall since 1963 (860 mm) results in a recharge estimate of 66 mm/y.

It must be mentioned here that this recharge value is probably at the lower end, since the fit ignores modern tritium input after the peak in the groundwater profile. Another integral calculation averages the tritium amount over the whole depth profile and integrates a constant

tritium concentration in the depth profile (shown as shaded rectangle in Figure 4.8). This would imply a constant tritium concentration of 0.54 TU in the water column down to a depth of 54 m, resulting in an integral of 29 TU·m. With the same calculations and values as above this results in a percentage of 16% rainfall and 140 mm/y recharge.

5.2.2.3 Bomb Peak – Distance Velocity

The volume of water in a profile above centre of mass or peak concentration is assumed equal to total soil water flux over relevant time period (Cook *et al.* 1994). We consider the relevant profile to be that bounded by the top of the water column, i.e. the water level in the bore, and the bomb peak.

Using the peak fit in Figure 5.4 we locate the depth of the tritium peak to 35 m. The distance velocity is determined dividing the depth of peak concentration (35 m) by the number of years since the peak, (2018-1963 i.e. 55 years), resulting in 630 mm/y. With an assumed porosity of 0.3, this results in a recharge rate of 190 mm/y.

5.2.3 Comments on tritium recharge assessment

Evidently these recharge calculations from tritium depth profiles contain a significant amount of ambiguity: the depth to which tritium is found is restricted by a very limited dataset, the maximum or peak concentration is as restricted, and the depth profile is synthesized from tritium measurements on wells that are many tens or hundreds of kilometres apart.

The assumed porosity is reasonable for the total porosity of the formation but certainly at the higher end of effective porosity and any effect of preferential flow results in lower recharge. However, earlier studies have shown that for the estimate of tracer-derived infiltration rates in karst the best assumed porosity is probably somewhere between total and effective porosity, due to dual porosity effects (Wilske *et al.* 2019).

Also, this recharge estimate is only valid for those areas where tritium has been detected, close to sinkholes. An assessment of the total amount of recharge over the CLA (in GL/y) needs mapping of the sinkholes delivering recharge and the extend to which tritium penetrates the aquifer around those sinkholes. This needs a much better infrastructure of wells and much higher density of tritium measurements than the present study was able to provide.

6 Summary

The present study significantly increased the available tracer dataset in the Cambrian Limestone Aquifer of the Beetaloo Sub-Basin. It confirmed and emphasized the counter-intuitive tracer patterns and internal contradictions between different tracer types, which were encountered during the first study. The following tracer findings are unusual or anomalous:

- ^{14}C increases along the flow path instead of decreasing due to radioactive decay.
- Gas tracers like CFCs, SF_6 and H1301 indicate in all samples a significant contribution of modern water (infiltrated past 1950, so during the last 60-70 years) whereas tritium indicates the presence of infiltration past 1963 in only a small fraction of samples (9 out of 33 samples).
- Heavy noble gases show high infiltration temperatures (30^oC-42^oC) but with unusual patterns of the noble gases such as excess in argon and excess in dissolved nitrogen.
- Helium is elevated in nearly all samples, in contradiction to the results from the anthropogenic gas tracers, in some samples up to 500-fold above solubility equilibrium, indicating influx of old water from deeper formations.

The new conceptual model derived in the present study reconciled many of the face value contradictions of the tracer patterns. According to this conceptualization

- Significant and highly localized infiltration and recharge happens through sinkholes and only during the heavy rains of the rainy season.
- This localized recharge transports tritium to the groundwater, since tritium is part of the mater molecule (HTO).
- This local infiltration raises the water table in the whole area by several meters, which entraps gas bubbles in the unsaturated zone creating comparably large excess air and "pumping" the gas tracers into groundwater. This explains a pattern of modern gas tracers (CFCs, SF_6, H1301) in absence of tritium.
- Between the recharge events part of the gases with high diffusivity (such as helium and neon) can escape the water column by partial re-equilibration with the soil gases, whereas the gas tracers with low diffusivity (such as SF_6, H1301, Kr and Xe) stay enriched above solubility equilibrium in groundwater.

This conceptual model explains the tracer results in a qualitative way. It would be desirable to also develop a quantitative (numerical) model of these processes. However, this is beyond the scope of the present report.

The conceptual model suggests that the conventional gas tracers (CFCs, SF_6, H1301) are not reliable indicators of recharge in this area, since they are overprinted by excess air and gas exchange processes. A future study needs to clarify whether gas tracers that are not sensitive to excess air, such as ^{85}Kr and ^{39}Ar, can further constrain the timing of recharge and gas exchange. Our attempt to quantify recharge in those areas where tritium is detected is in agreement with

results from the chloride mass balance. Tritium indicates that recharge is much higher in the north and north-west of the study area.

Future studies need to clarify what exactly is the source of elevated helium in the CLA. Most probably localized fractures generate the three very elevated helium concentrations encountered, but a general flux of helium from underlying formations is not completely ruled out. It also remains unclear how much water flow this helium flux represents, a question which can only be answered once the helium concentration in pore water and groundwater of deeper formations is measured. This requires new drilling.

The present conceptualisation includes the hypothesis that the increasing ^{14}C along the flow path is only due to increasing gas exchange where modern CO_2 from root respiration is "pumped" into the groundwater as dissolved total inorganic carbon. Another hypothesis concerns the significant fraction of the modern ^{14}C that results from infiltration on a larger time scale than represented by tritium (centuries). A tracer in the intermediate time scale (^{39}Ar) is necessary to provide the corroborative evidence; this represents a significantly higher effort in sampling and measurement. The measurement of radioactive noble gas isotope (^{85}Kr and ^{39}Ar) can also further elucidate the gas exchange processes, since these tracers are not influenced by excess air.

References

Aeschbach-Hertig, W, El-Gamal, H, Wieser, M, Palcsu, L (2008) Modelling excess air and degassing in groundwater by equilibrium partitioning with a gas phase. *Water Resources Research* **44**,

Aeschbach-Hertig, W, Peeters, F, Beyerle, U, Kipfer, R (2000) Paleotemperature reconstruction from noble gases in ground water taking into account equilibration with entrapped air. *Nature* **405**, 1040-1044.

Allison, GB, Holmes, JW, Hughes, MW (1971) Tritium fallout in southern Australia and its hydrologic implications. *Journal of Hydrology* **14**, 307-321.

Allison, GB, Hughes, MW (1975) The use of environmental tritium to estimate recharge to a South-Australian aquifer. *Journal of Hydrology* **26**, 245-254.

Allison, GB, Stone, WJ, Hughes, MW (1985) Recharge in karst and dune elements of a semi-arid landscape as indicated by natural isotopes and chloride. *Journal of Hydrology* **76**, 1-25.

Anders, E, Grevesse, N (1989) Abundances of the elements: Meteoritic and solar. *Geochimica et Cosmochimica Acta* **53**, 197-214.

Andrews, JN, Davis, S, Fabryka-Martin, J, Fontes, JC, Lehmann, BE, Loosli, HH, Michelot, J-L, Moser, H, Smith, B, Wolf, M (1989) The in-situ production of radioisotopes in rock matrices with particular reference to the Stripa granite. *Geochimica et Cosmochimica Acta* **53**, 1803–1815.

Andrews, JN, Florkowski, T, Lehmann, BE, Loosli, HH (1991) Underground production of radionuclides in the Milk River aquifer, Alberta, Canada. *Applied Geochemistry* **6**, 425–434.

Andrews, JN, Lee, DJ (1979) Inert gases in groundwater from the Bunter Sandstone of England as indicators of age and palaeoclimatic trends. *Journal of Hydrology* **41**, 233-252.

APLNG (2014) Australia Pacific LNG Upstream 2013-2014 Groundwater Assessment Report. Available at http://www.aplng.com.au/pdf/Q-LNG01-75-RP-0001__Annual_GW__Report_Rev1_Final.pdf.

Appelo, CAJ, Postma, D (1999) Chemical analysis of groundwater. *Geochemistry, Groundwater and Pollution. AA Balkema/Rotterdam/Brookfield*

Archbold, ME, Elliot, T, Kalin, RM (2011) Carbon Isotopic Fractionation of CFCs during Abiotic and Biotic Degradation. *Environmental Science & Technology* **46**, 1764-1773.

Badino, G, Chignola, R (2019) Fluctuations of Atmospheric Pressure and the Sound of Underground Karst Systems: The Antro del Corchia Case (Apuane Alps, Italy). *Frontiers in Earth Science* **7**,

Bauer, S, Fulda, C, Schäfer, W (2001) A multi-tracer study in a shallow aquifer using age dating tracers 3H, 85Kr, CFC-113 and SF6 - indication for retarded transport of CFC-113. *Journal of Hydrology* **248**, 14-34.

Bentley, HW, Phillips, FM, Davis, SN, Habermehl, MA, Airey, PL, Calf, GE, Elmore, D, Gove, HE, Torgersen, T (1986) Chlorine 36 Dating of Very Old Groundwater 1. The Great Artesian Basin, Australia. *Water Resources Research* **22**, 1991-2001.

Busenberg, E, Plummer, LN (1992) Use of chlorofluorocarbons CCl3F and CCl2F2 as hydrologic tracers and age-dating tools: the alluvium and terrace system in central Oklahoma. *Water Resources Research* **28**, 2257-2283.

Cartwright, I, Cendón, D, Currell, M, Meredith, K (2017) A review of radioactive isotopes and other residence time tracers in understanding groundwater recharge: Possibilities, challenges, and limitations. *Journal of Hydrology* **555**, 797-811.

Cartwright, I, Morgenstern, U (2012) Constraining groundwater recharge and the rate of geochemical processes using tritium and major ion geochemistry: Ovens catchment, southeast Australia. *Journal of Hydrology* **475**, 137-149.

Cartwright, I, Weaver, TR, Stone, D, Reid, M (2007) Constraining modern and historical recharge from bore hydrographs, 3H, 14C, and chloride concentrations: Applications to dual-porosity aquifers in dryland salinity areas, Murray Basin, Australia. *Journal of Hydrology* **332**, 69-92.

Collon, P, Kutschera, W, Loosli, HH, Lehmann, B, Purtschert, R, Love, A, Sampson, L, Anthony, D, Davids, B, Cole, D, Morrissey, D, Pardo, R, Paul, M, Sherrill, B, Steiner, M (2000) 81Kr in the Great Artesian

Basin, Australia: a new method for dating very old groundwater. *Earth and Planetary Science Letters* **182**, 103-113.
Cook, P, Beck, V, Brereton, D, Clark, R, Fisher, B, Kentish, S, Toomey, J, Williams, JW (2013) Engineering Energy: Unconventional Gas Production. Final Report for the Report for the Australian Council of Learned Academies, www.acola.org.au. Australian Council of Learned Academies (ACOLA).
Cook, PG, Jolly, ID, Leaney, FW, Walker, GR, Allan, GL, Fifield, LK, Allison, GB (1994) Unsaturated zone tritium and chlorine 36 profiles from southern Australia: Their use as tracers of soil water movement. *Water Resources Research* **30**, 1709-1719.
Cook, PG, Solomon, DK (1995) Transport of Atmospheric Trace Gases to the Water Table: Implications for Groundwater Dating with Chlorofluorocarbons and Krypton 85. *Water Resources Research* **31**, 263-270.
Cook, PG, Walker, G (1996) Evaluation of the use of 3H and 36Cl to estimate groundwater recharge in arid and semi-arid environments. In 'Isotopes in Water Resources Management. Vienna'. Volume I pp. 397-403. (IAEA, Vienna.:
Cox, G, Collins, A (2017) A time capsule containing 118 trillion cubic feet of gas is buried in northern Australia. *The Conversation*
Craig, H (1961) Isotopic variations in meteoric waters. *Science* **133**, 1702-1703.
Crosbie, RS, Morrow, D, Cresswell, R, Leaney, FW, Lamontagne, S, Lefournour, M (2012) New insights to the chemical and isotopic composition of rainfall across Australia.
Davies, PJ, Crosbie, RS (2018) Mapping the spatial distribution of chloride deposition across Australia. *Journal of Hydrology* **561**, 76-88.
Deeds, DA, Vollmer, MK, Kulongoski, JT, Miller, BR, Mühle, J, Harth, CM, Izbicki, JA, Hilton, DR, Weiss, RF (2008) Evidence for crustal degassing of CF4 and SF6 in Mojave Desert groundwaters. *Geochimica et Cosmochimica Acta* **72**, 999-1013.
DPIR (2016) Methodology for the Sampling of Groundwater. Northern Territory Government, Department of Primary Industries and Resources., Darwin. Available at https://nt.gov.au/__data/assets/pdf_file/0014/203360/aa7-024-methodology-for-the-sampling-of-groundwater-advisory-note.pdf.
Einstein, A (1905) Über die von der molekularkinetischen Theorie der Wärme geforderte Bewegung von in ruhenden Flüssigkeiten suspendierten Teilchen. *Annalen der Physik* **17**, 549-560.
Farquhar, GD, Ehleringer, JR, Hubick, KT (1989) Carbon Isotope Discrimination and Photosynthesis. *Annual Review of Plant Physiology and Plant Molecular Biology* **40**, 503-537.
Friedrich, R, Vero, G, von Rohden, C, Lessmann, B, Kipfer, R, Aeschbach-Hertig, W (2013) Factors controlling terrigenic SF6 in young groundwater of the Odenwald region (Germany). *Applied Geochemistry* **33**, 318-329.
Fulton, S, Knapton, A (2015) Beetaloo Basin Hydrogeological Assessment. CloudGMS.
Gonfiantini, R (1986) Environmental Isotopes in Lake Studies. In 'Handbook of Environmental Isotope Geochemistry. Vol. 2, The Terrestrial Environment B.' (Eds P Fritz, J-C Fontes.) Vol. 2 pp. 113-168.
Harnisch, J, Eisenhauer, A (1998) Natural CF4 and SF6 on Earth. *Geophyscal Research Letters* **25**, 2401-2406.
Healy, RW (2010) 'Estimating Groundwater Recharge.' (Cambridge University Press: Cambridge)
Heaton, THE, Vogel, JC (1981) "Excess Air" in Groundwater. *Journal of Hydrology* **50**, 201-216.
Hoffmann, G, Jouzel, J, Masson, V (2000) Stable water isotopes in atmospheric general circulation models. *Hydrological Processes* **14**, 1385-1406.
Houben, GJ, Koeniger, P, Schloemer, S, Gröger-Trampe, J, Sültenfuß, J (2018) Comparison of depth-specific groundwater sampling methods and their influence on hydrochemistry, isotopy and dissolved gases – Experiences from the Fuhrberger Feld, Germany. *Journal of Hydrology* **557**, 182-196.
IAEA (2006) 'Use of Chlorofluorocarbons in Hydrology. A Guidebook.' (International Atomic Energy Agency: Vienna)
IAEA (2013) 'Isotope Methods for Dating Old Groundwater.' (International Atomic Energy Agency: Vienna)
IAEA/WMO (2015) Global Network for Isotopes in Precipitation. The GNIP Database. Release 3, October 1999.
Jähne, B, Heinz, G, Dietrich, W (1987) Measurement of the diffusion coefficients of sparingly soluble gases in water. *Journal of Geophysical Research: Oceans* **92**, 10767-10776.

Jiang, W, Bailey, K, Lu, ZT, Mueller, P, O'Connor, TP, Cheng, CF, Hu, SM, Purtschert, R, Sturchio, NC, Sun, YR, Williams, WD, Yang, GM (2012) An atom counter for measuring 81Kr and 85Kr in environmental samples. *Geochimica et Cosmochimica Acta* **91**, 1-6.

Johannesson, KH, Lyons, BW (2000) Rare Earth Elements in Groundwater. (Cook, Peter G., Herczeg, Andrew L. (eds.): Environmental Tracers in Subsurface Hydrology, pp. 485-492; Kluwer Academic Press (Boston, Mass.):

Johannesson, KH, Stetzenbach, KJ, Hodge, VF (1997) Rare earth elements as geochemical tracers of regional groundwater mixing. *Geochimica et Cosmochimica Acta* **61**, 3605-3618.

Jung, M, Aeschbach, W (2018) A new software tool for the analysis of noble gas data sets from (ground)water. *Environmental Modelling & Software* **103**, 120-130.

Karp, D (2008) Surface and Groundwater Interaction the Mataranka Area. Department of Natural Resources, Environment and the Arts No. ISBN: 978 1 921519 01 7 Available at http://www.territorystories.nt.gov.au/bitstream/10070/228528/1/WRD08017.pdf.

Kashiwaya, K, Hasegawa, T, Nakata, K, Tomioka, Y, Mizuno, T (2015) Multiple tracer study in Horonobe, northern Hokkaido, Japan: 2. Depletion of chlorofluorocarbons (CFCs) estimated using 3H/3He index and lumped parameter models. *Journal of Hydrology* **524**, 111-122.

Kersting, A (2018) Dating of groundwater and ocean samples with noble gas radioisotopes – sample preparation and field applications. PhD thesis, Ruperto-Carola University of Heidelberg.

King, AC, Raiber, M, Cox, ME, Cendón, DI (2017) Comparison of groundwater recharge estimation techniques in an alluvial aquifer system with an intermittent/ephemeral stream (Queensland, Australia). *Hydrogeology Journal* **25**, 1759-1777.

King, DB, Saltzman, ES (1995) Measurement of the diffusion coefficient of sulfur hexafluoride in water. *Journal of Geophysical Research: Oceans* **100**, 7083-7088.

Koh, D-C, Plummer, LN, Busenberg, E, Kim, Y (2007) Evidence for terrigenic SF6 in groundwater from basaltic aquifers, Jeju Island, Korea: Implications for groundwater dating. *Journal of Hydrology* **339**, 93-104.

Königer, P, Leibundgut, C, Link, T, Marshall, JD (2010) Stable isotopes applied as water tracers in column and field studies. *Organic Geochemistry* **41**, 31-40.

Königer, P, Leibundgut, C, Stichler, W (2009) Spatial and temporal characterisation of stable isotopes in river water as indicators of groundwater contribution and confirmation of modelling results; a study of the Weser river, Germany. *Isotopes in Environmental and Health Studies* **45**, 289 - 302.

Lamontagne, S, Taylor, AR, Batlle-Aguilar, J, Suckow, A, Cook, PG, Smith, SD, Morgenstern, U, Stewart, MK (2015) River infiltration to a subtropical alluvial aquifer inferred using multiple environmental tracers. *Water Resources Research* **51**, 4532-4549.

Leaney, FW, Herczeg, AL (2006) A rapid field extraction method for determination of radon-222 in natural waters by liquid scintillation counting. *Limnology and Oceanography: Methods* **4**, 254-259.

Lehmann, BE, Love, A, Purtschert, R, Collon, P, Loosli, HH, Kutschera, W, Beyerle, U, Aeschbach-Hertig, W, Kipfer, R, Frape, SK, Herczeg, A, Moran, J, Tolstikhin, IN, Gröning, M (2003) A comparison of groundwater dating with 81Kr, 36Cl and 4He in four wells of the Great Artesian Basin, Australia. *Earth and Planetary Science Letters* **211**, 237-250.

Lu, ZT, Schlosser, P, Smethie Jr, WM, Sturchio, NC, Fischer, TP, Kennedy, BM, Purtschert, R, Severinghaus, JP, Solomon, DK, Tanhua, T, Yokochi, R (2014) Tracer applications of noble gas radionuclides in the geosciences. *Earth-Science Reviews* **138**, 196-214.

Mallants, D, Jeffrey, R, Zhang, X, Wu, B, Kear, J, Chen, Z, Wu, B, Bekele, E, Raiber, M, Apte, S, Gray, B (2018) Review of plausible chemical migration pathways in Australian coal seam gas basins. *International Journal of Coal Geology* **195**, 280-303.

Maloszewski, P, Zuber, A (1985) On the theory of tracer experiments in fissured rocks with a porous matrix. *Journal of Hydrology* **79**, 333-358.

Mook, WG (Ed. IAH (2005) 'Introduction to Isotope Hydrology:Stable and Radioactive Isotopes of Hydrogen, Carbon, and Oxygen.' (Taylor & Francis IAH series:

Mook, WG, Plicht, Jvd (1999) Reporting 14C activities and concentrations. *Radiocarbon* **41**, 227-239.

Morris, R (2016) personal communication.

NT (2018) The Scientific Inquiry into Hydraulic Fracturing in the Northern Territory, Final Report. Northern Territories Government, Darwin NT. Available at https://frackinginquiry.nt.gov.au/inquiry-reports?a=494286.
NT, 2019. The NT Water Data WebPortal v2019.1.205. The Northern Territory Government, Darwin.
O'Leary, MH (1981) Carbon isotope fractionation in plants. *Phytochemistry* **20**, 553-567.
O'Leary, MH (1988) Carbon Isotopes in Photosynthesis. *BioScience* **38**, 328-336.
Oster, H, Sonntag, C, Münnich, KO (1996) Groundwater age dating with chlorofluorocarbons. *Water Resources Research* **32**, 2989-3001.
Phillips, FM (2013) Chlorine-36 dating of old groundwater. In 'Isotope Methods for Dating Old Groundwater.' (Eds A Suckow, PK Aggarwal, LJ Araguas-Araguas.) pp. 125-152. (International Atomic Energy Agency: Vienna)
Phillips, FM, Mattick, JL, Duval, TA, Elmore, D, Kubik, PW (1988) Chlorine 36 and tritium from nuclear weapons fallout as tracers for long-term liquid and vapor movement in desert soils. *Water Resources Research* **24**, 1877-1891.
Plummer, LN, Glynn, PD (2013) Radiocarbon Dating in Groundwater Systems. In 'Isotope Methods for Dating Old Groundwater.' (Eds A Suckow, PK Aggarwal, LJ Araguas-Araguas.) pp. 33-89. (International Atomic Energy Agency: Vienna)
Purtschert, R, Onstott, TC, Jiang, W, Lu, ZT, Müller, P, Zappala, J, Yokochi, R, Van Heerden, E, Cason, E, Lau, M, Kieft, T, Brennwald, MS (2017) Underground production of 81Kr detected in subsurface fluids. In 'Goldschmidt 2017. Paris'. (European Association of Geochemistry and the Geochemical Society:
Purtschert, R, Yokochi, R, Sturchio, NC (2013) 81Kr dating of old groundwater. In 'Isotope Methods for Dating Old Groundwater.' (Eds A Suckow, PK Aggarwal, LJ Araguas-Araguas.) pp. 91-124. (International Atomic Energy Agency: Vienna)
Rachakonda, PK, Wilkes, P, Larcher, A, Hortle, A, Barrett, D, Horner, N, Woltering, M (2018) Groundwater Baseline Assessment of the Beetaloo Sub-Basin, Northern Territory. Report for Origin and Santos. CSIRO.
Radke, BM, Ferguson, J, Cresswell, RG, T.R., R, Habermehl, MA (2000) 'Hydrochemistry and implied hydrodynamics of the Cada-owie-Hooray Aquifer Great Artesian Basin.' (Bureau of Rural Sciences, Australia:
Ransley, TR, Smerdon, BDe (2012) Hydrostratigraphy, hydrogeology and system conceptualisation of the Great Artesian Basin. CSIRO Water for a Healthy Country Flagship, Australia.
Rohden, Cv, Kreuzer, A, Chen, Z, Aeschbach-Hertig, W (2010) Accumulation of natural SF6 in the sedimentary aquifers of the North China Plain as a restriction on groundwater dating. *Isotopes in Environmental and Health Studies* **46**, 279-290.
Roß, JO (2010) Simulation of atmospheric krypton-85 transport to assess the detectability of clandestine nuclear reprocessing. PhD thesis, Universität Hamburg.
Rozanski, K (1985) Deuterium and Oxygen-18 in European groundwaters - Links to atmospheric circulation in the past. *Chemical Geology (Isotope Geoscience Section)* **52**, 349-363.
Silverman, MR, Landon, SM, Leaver, JS, Mather, TJ, Berg, E (2007) No fuel like an old fuel: Proterozoic oil and gas potential in the Beetaloo Basin, Northern Territory, Australia. In 'Proceedings of the Central Australian Basins Symposium (CABS). Alice Springs, Northern Territory', 16–18 August, 2005. (Eds TJ Munson, GJ Ambrose) pp. 205–215. (Northern Territory Geological Survey, Special Publication 2 Munson (2014):
Smith, DC, Richards, JM (2015) Social License to Operate: Hydraulic Fracturing-Related Challenges Facing the Oil & Gas Industry. *Oil & Gas, Nat. Resources & Energy J.* **1**, 81-163.
Smith, SD (2015) Geochemical baseline monitoring: quartz-helium trial. CSIRO, Adelaide. Available at https://gisera.org.au/wp-content/uploads/2012/06/BaselineChem_Quartz-He_report-March-2015.pdf.
Solomon, DK, Poreda, RJ, Cook, PG, Hunt, A (1995) Site Characterization Using 3H/3 He Ground-Water Ages, Cape Cod, MA. *Groundwater* **33**, 988-996.
Sonntag, C, Münnich, KO, Jacob, H, Rozanski, K (1983) Variations of Deuterium and Oxygen-18 in Continental Precipitation and Groundwater, and Their Causes. In 'Variations in the Global Water Budget.' (Eds A Street-Perrott, M Beran, R Ratcliffe.) pp. 107-124. (Springer Netherlands: Dordrecht)

Sonntag, C, Schoch-Fischer, H (1985) Deuterium and Oxygen 18 in Water Vapour and Precipitation: Application to Atmospheric Water Vapour Transport and to Paleoclimate. *Isotopenpraxis* **21**, 193-198.

Stadler, S, Osenbrück, K, Knöller, K, Suckow, A, Sültenfuß, J, Oster, H, Himmelsbach, T, Hötzl, H (2008) Understanding the origin and fate of nitrate in groundwater of semi-arid environments. *Journal of Arid Environments* **72**, 1830-1842.

Stevanović, Z (2015) 'Karst Aquifers - Characterization and Engineering.' (Springer International Publishing:

Stone, AEC, Edmunds, WM (2014) Naturally-high nitrate in unsaturated zone sand dunes above the Stampriet Basin, Namibia. *Journal of Arid Environments* **105**, 41-51.

Stuiver, M, Polach, HA (1977) Discussion of Reporting of 14C Data. *Radiocarbon* **19**, 355-363.

Stute, M, Forster, M, Frischkorn, H, Serejo, A, Clark, JF, Schlosser, P, Broecker, WS, Bonani, G (1995) Cooling of Tropical Brazil (5°C) During the Last Glacial Maximum. *Science* **269**, 379-383.

Stute, M, Schlosser, P (1993) Principles and applications of the Noble Gas Paleothermometer. In 'Climate Change in Continental Isotopic Records, Geophysical Monograph.' (Eds PK Swart, KC Lohmann, J McKenzie, S Svin.) Vol. 78 pp. 89-100. (American Geohysical Union:

Stute, M, Sonntag, C, Deak, J, Schlosser, P (1992) Helium in deep circulating groundwater in the Great Hungarian Plain: Flow dynamics and crustal and mantle helium fluxes. *Geochimica et Cosmochimica Acta* **56**, 2051-2067.

Stute, M, Talma, S (1997) Glacial temperatures and moisture transport regimes reconstructed from noble gases and d18O, Stampriet aquifer, Namibia.

Suckow, A (2009) Analysis of Radionuclides. In 'Environmental Radionuclides. Tracers and Timers of Terrestrial Processes.' (Ed. K Froehlich.) Vol. Volume 16 pp. 363-406. (Elsevier:

Suckow, A (2012) 'Lumpy - an interactive Lumped Parameter Modeling code based on MS Access and MS Excel., EGU 12.' Vienna (European Geosciences Union. Available at http://meetingorganizer.copernicus.org/EGU2012/EGU2012-2763.pdf

Suckow, A (2013) System Analysis using Multi-Tracer Approaches. In 'Isotope Methods for Dating Old Groundwater.' (Eds A Suckow, PK Aggarwal, LJ Araguas-Araguas.) pp. 217-244. (International Atomic Energy Agency: Vienna)

Suckow, A (2014a) The age of groundwater – Definitions, models and why we do not need this term. *Applied Geochemistry* **50**, 222-230.

Suckow, A (2014b) Lumpy - Lumped Parameter Modelling of Age Distributions using up to two Parallel Black Boxes. Software Manual. Leibniz Institute for Applied Geophysics (LIAG), S3, Geochronology and Isotope Hydrology, Hannover.

Suckow, A, Deslandes, A, Gerber, C, Lamontagne, S (2018) Environmental Tracers in the Beetaloo Sub-Basin. Historical data and a first reconnaissance study of eight samples. CSIRO, Adelaide, Australia.

Suckow, A, Deslandes, A, Gerber, C, Mallants, D, Smith, SD (2019) Commissioning of the CSIRO Noble Gas Facilities at Waite. CSIRO Land and Water, Adelaide.

Suckow, A, Dumke, I (2001) A database system for geochemical, isotope hydrological, and geochronological laboratories. *Radiocarbon* **43**, 325-337.

Suckow, A, Sonntag, C (1993) The influence of Salt on the Noble Gas Thermometer. In 'Isotope Techniques in the Study of Past and Current Environmental Changes in the Hydrosphere and the Atmosphere. Vienna'. pp. 307-318. (International Atomic Energy Agency (IAEA):

Suckow, A, Sonntag, C, Gröning, M, Thorweihe, U (1993) 'Ground water recharge in the Umm Kedada Basin, NW-Sudan, derived from environmental isotopes of soil moisture in samples collected from deep dug wells.' (Thorweihe, U., Schandelmeier, H. (eds): Geoscientific Research in Northeast Africa, pp. 677-685; Balkema, Rotterdam:

Sudicky, EA, Frind, EO (1981) Carbon 14 dating of groundwater in confined aquifers: Implications of aquitard diffusion. *Water Resources Research* **17**, 1060-1064.

Suzuki, R, Shimodaira, H (2006) Pvclust: an R package for assessing the uncertainty in hierarchical clustering. *Bioinformatics* **22**, 1540-1542.

Tadros, CV, Hughes, CE, Crawford, J, Hollins, SE, Chisari, R (2014) Tritium in Australian precipitation: A 50 year record. *Journal of Hydrology* **513**, 262-273.

Taylor, AR, Pichler, MM, Olifent, V, Thompson, J, Bestland, EA, Davies, PJ, Lamontagne, S, Suckow, AO, Robinson, NI, Love, A (2015) Groundwater Flow Systems of North Eastern Eyre Peninsula: a multi-

disciplinary approach: hydrogeology, geophysics and environmental tracers. Facilitating Long Term Outback Water Solutions —Stage 2. Goyder Institute for Water Research.
Tickell, SJ (2003) Water Resource Mapping Barkly Tablelands. Natural Systems Division, Northern Territory Department of Infrastructure Planning and Environment, No. Technical Report No. 23/2003 Available at http://www.territorystories.nt.gov.au/jspui/bitstream/10070/228204/1/WRD03023.pdf.
Tickell, SJ (2004) Carbon Dating of Groundwaters in the Oolloo Dolostone Aquifer. Department of Infrastructure Planning and Environment, Natural Resources Division Available at https://www.territorystories.nt.gov.au/jspui/bitstream/10070/229203/1/WRD04021.pdf.
Tickell, SJ (2005) Groundwater Resources of the Tindall Limestone. Department of Natural Resources the Environment and the Arts, Natural Resources Division, Darwin. Available at http://ntl.communitystories.net/jspui/bitstream/10070/241885/1/Groundwater_Resources_of_the_Tindall_Limestone.pdf.
Tickell, SJ (2016) Stable isotopes and carbon dating of groundwaters in the Tindall aquifer. Water Resources Division, Northern Territory Department of Land Resource Management, No. Technical Report No. 12/2016D Available at http://www.territorystories.nt.gov.au/jspui/bitstream/10070/265589/1/Stable%20isotopes%20and%20carbon%20dating%20of%20groundwaters%20in%20the%20Tindall%20aquifer.pdf.
Tickell, SJ, Bruwer, Q (2017) Georgina Basin Groundwater Assessment: Daly Waters to Tennant Creek. Northern Territory Department of Environment and Natural Resources Available at https://www.territorystories.nt.gov.au/jspui/bitstream/10070/304921/9/Georgina%20Basin%20Groundwater%20Assessment%20-%20Daly%20Waters%20to%20Tenant%20Creek.pdf.
Torgersen, T, Purtschert, R, Phillips, FM, Plummer, LN, Sanford, W, Suckow, A (2013) Defining Groundwater Age. In 'Isotope Methods for Dating Old Groundwater.' (Eds A Suckow, PK Aggarwal, LJ Araguas-Araguas.) pp. 21-32. (International Atomic Energy Agency: Vienna)
Torgersen, T, Stute, M (2013) Helium (and other Noble Gases) as a Tool for Understanding Long Timescale Groundwater Transport. In 'Isotope Methods for Dating Old Groundwater.' (Eds A Suckow, PK Aggarwal, LJ Araguas-Araguas.) pp. 179-216. (International Atomic Energy Agency: Vienna)
Visser, A, Broers, HP, Bierkens, MFP (2007) Dating Degassed Groundwater with 3H/3He. *Water Resourources Research* **43**,
Weise, SM, Moser, H (1987) Groundwater dating with helium Isotopes. . In 'International Symposium on Isotope Techniques in Water Resources Development. Vienna'. Volume IAEA-SM-299/44 pp. 105-126.
Wilkes, P, Rachakonda, PK, Larcher, A, Woltering, M (2019) Baseline assessment of groundwater characteristics in the Beetaloo Sub-basin, NT. Geochemistry Analysis report to the Gas Industry Social and Environmental Research Alliance (GISERA). CSIRO, Canberra. CSIRO, Australia.
Wilske, C, Suckow, A, Mallast, U, Meier, C, Merchel, S, Merkel, B, Pavetich, S, Rödiger, T, Rugel, G, Sachse, A, Weise, SM, Siebert, C (2019) A multi-environmental tracer study to determine groundwater residence times and recharge in a structurally complex multi-aquifer system. *Hydrol. Earth Syst. Sci. Discuss.* **2019**, 1-30.
Winnick, MJ, Chamberlain, CP, Caves, JK, Welker, JM (2014) Quantifying the isotopic 'continental effect'. *Earth and Planetary Science Letters* **406**, 123-133.
Yapp, CJ, Epstein, S (1977) Climatic implications of D/H ratios of meteoric water over North America (9500–22,000 B.P.) as inferred from ancient wood cellulose CH hydrogen. *Earth and Planetary Science Letters* **34**, 333-350.
Yin-Foo, D, Matthews, I (2000) Water Resources Assessment of the Sturt Plateau. Techncal Data Report. Northern Territory Government, Department of Infrastructure, Planning and Environment.
Zimmermann, U, Münnich, KO, Roether, W (1967) Downward movement of soil moisture traced by means of hydrogen isotopes. *Geophys. Mono. Am. Geophys. Union.* **11**,

Appendix A Using environmental tracers to quantify groundwater time scales

Using environmental tracers as age indicators relies on time-dependent concentrations of trace substances in water. The trace substances have a known time-dependent input function as indicated on the left of Figure A.1. Tracers can be stable and conservative, like for example ^{18}O and ^{2}H, CFCs, H1301 and SF_6. Other trace substances can be radioactive, and in this case the natural radioactivity can provide time information also when the input function at recharge is constant, as for example, with ^{39}Ar, ^{14}C and ^{36}Cl. Also, a combination of time-dependent input and radioactive decay is possible such as with ^{3}H and ^{85}Kr, as long as the time-dependent input is quantified. Or, the concentration of the tracer can increase with time along the flow path, e.g. due to underground production, as is the case with ^{4}He. Any "age" deduced from the measured concentration of an environmental tracer, however, is never unique, no matter what tracer is used. Figure A.1 illustrates this.

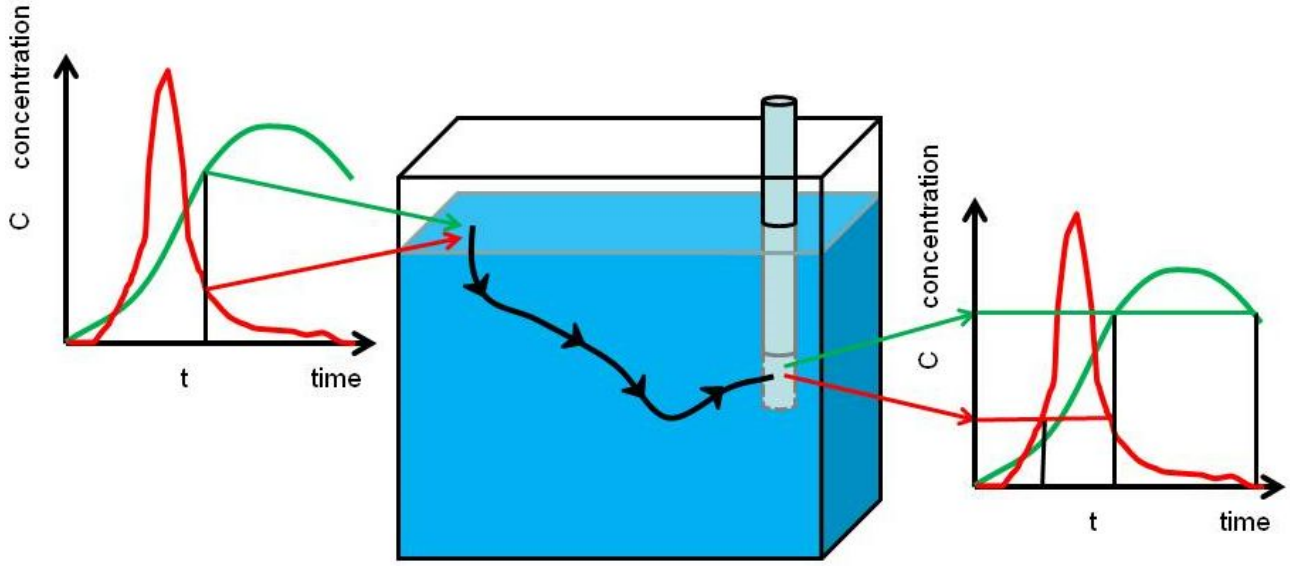

Figure A.1: Principle of the application of environmental tracers to deduce groundwater age (Suckow 2014a)

The tracer concentration always needs to be known at the recharge site ("input function", represented by the red and green curve on the left, indicating two different tracers). However, the measured concentration at the well screen allows for several moments in time to be deduced (horizontal red and green lines on the right, each giving two ages, represented as vertical black lines). Therefore, every application needs a combination of several tracers to derive a unique value on the time axis (middle black line agreeing both to the red and green concentrations on the input curve). Details of different age definitions and how they relate to common conceptions of human age can be found in Suckow (2014a). Only those tracers and their properties will be discussed in the following sections that are important in the context of the present project. It is, however, important to note that all tracer methods determine the distance velocity v within the aquifer (unit: m/year). This is related to the Darcy velocity q (volumetric groundwater flux in cubic meters per square meter aquifer cross section and year; also expressible with unit m/y) by the (effective) porosity n_e via $v=q/n_e$. Tracer derived velocities are therefore always larger than Darcy velocities and the factor n_e between v and q needs an independent assessment.

A.1 Tracers used

Tracers used in this report to interpret flow velocities were the stable isotopes of water (^{18}O and ^{2}H), CFCs, H1301, SF_6, tritium (^{3}H), ^{14}C, ^{36}Cl and ^{4}He. They will be introduced shortly in the following sections. The chemical compounds CFCs, H1301 and SF_6 are of anthropogenic origin, are dissolved in water and recharge times can be deduced from their known atmospheric concentration. The other tracers are radioactive (^{14}C, ^{36}Cl, ^{3}H) or stable isotopes (^{2}H, ^{18}O, ^{4}He) of elements. Isotopes (from the Greek word 'iso topos' for 'same place' – meaning the same place in the periodic table of the elements) are varieties of atoms of one element with identical chemical behaviour (since they belong to the same element) but slightly different mass, which can result in fractionation during physical or biological processes. This difference in mass is due to different number of neutrons. Since the chemical properties are determined by the number of electrons in the hull, which in a neutral atom equals the number of protons in the nucleus, all isotopes show the same chemical behaviour of the element. This makes isotopes ideal tracers. Too few or too many neutrons relative to protons renders a core unstable, which is why some isotopes are radioactive. Environmental tracers use all these properties to investigate natural processes – known concentration at the time of recharge, identical chemical behaviour since it is the same element, differences in mass that lead to fractionation, and radioactive decay that provides a natural 'clock' for natural processes.

A.1.1 Stable Isotopes of water

The water molecule H_2O is formed of the elements hydrogen and oxygen. While the most abundant isotopes of hydrogen and oxygen are ^{1}H and ^{16}O, respectively (forming $^{1}H_2{}^{16}O$), both elements have a stable and rare isotope, ^{2}H and ^{18}O. In the natural water cycle these isotopes behave as normal water. In fact they *are* water, forming molecules with slightly different masses (e.g. $^{2}H^{1}H^{16}O$ and $^{1}H_2{}^{18}O$). Nevertheless, the different isotopic species of water are slightly enriched during different natural processes, the most important being phase transitions (e.g. from liquid to gas phase). The heavier molecules, containing ^{2}H and ^{18}O, are slightly enriched (by a few ‰ only) in the less mobile phase. For example, the ocean will contain slightly more ^{2}H and ^{18}O per gram water than the water vapour formed from it, and the raindrop will contain slightly more ^{2}H and ^{18}O than the cloud it formed from. The magnitude of this isotopic difference depends on the temperature prevailing during the phase transition (evaporation or condensation). These slight differences in the isotopic ratio *R* are expressed as per mil deviation of a standard, called SMOW (Standard Mean Ocean Water) using the delta notation:

$$\delta \equiv \frac{R_{Sample} - R_{Standard}}{R_{Standard}} = \frac{R_{Sample}}{R_{Standard}} - 1 \quad [\cdot 1000‰] \tag{A1}$$

Since the standard is ocean water and since, as mentioned, the water vapour derived from it will have less of the heavy isotopic species, and since nearly the entire global water cycle happens after this phase transition, most isotopic values for $\delta^{18}O$ and $\delta^{2}H$ in water samples are negative. One has to keep in mind that the fractionation effects in stable isotopes are very small, per mil only, whereas the effects of radioactivity (^{3}H, ^{14}C, ^{36}Cl) or concentration (CFCs, SF_6) are comparably large: several percent or a factor of two to ten. As a consequence of natural isotopic enrichment processes, several effects can be observed.

Continental effect

Air masses losing water as rain when moving inland will gradually deplete in the heavy isotopes. This means that rain falling further inland will be more negative in $\delta^{18}O$ and $\delta^{2}H$ than close to the coast. The effect was first described for Europe (Sonntag and Schoch-Fischer 1985) and later verified all over the world, see http://www-naweb.iaea.org/napc/ih/documents/userupdate/Waterloo/. The magnitude of this effect is on the order of 0.2‰/100 km in $\delta^{18}O$ (Yapp and Epstein 1977; Sonntag *et al.* 1983) but needs to be quantified for any region of interest since the underlying physical processes are quite complex (Winnick *et al.* 2014).

Evaporation effect

If a water body evaporates, the water vapour will be isotopically lighter (more negative in δ values) than the remaining water body. As a consequence, the remaining water body will gradually develop more positive values in $\delta^{18}O$ and $\delta^{2}H$. This is a useful tool in water balance investigations of lake studies (Gonfiantini 1986) and allows determining the evaporated fraction of lakes, channels and rivers. Evaporation can be easily determined in a plot of $\delta^{2}H$ versus $\delta^{18}O$ because the slope of evaporating waters in this plot is characteristically smaller – around 4 to 6 – than the global meteoric water line GWML (Craig 1961) on which most other precipitation and groundwater values are situated and which has a slope of 8. The slope of the evaporation line depends on relative humidity, for tropical conditions with 100% relative humidity it approaches the slope of 8 of the GMWL (Gonfiantini 1986). For the present study the evaporative effect is only important in case groundwater infiltrates from rivers or lakes, which is not to be expected.

Rayleigh Fractionation during cloud rainout

Isotope enrichment during rainout of clouds is like the evaporation effect. The (invisible) water vapour forming the cloud will be isotopically lighter (more negative in δ values) than the droplets that are visible as clouds, and the raindrops falling as precipitation. Consequently, the remaining water vapour will gradually develop more positive values in $\delta^{18}O$ and $\delta^{2}H$. In clouds the isotopic separation between vapour and liquid often happens close to equilibrium conditions, which contrasts with lakes, ponds and rivers, where evaporation is driven by the deficiency of relative humidity and wind speed. On the other hand, heavy rain showers can remove water much faster from the atmosphere than a lake can evaporate. These two facts mean that the isotopic composition of rain is normally closer to the meteoric water line (slope of 8), but at the same time isotopic composition can vary strongly within one heavy rain event. Very positive isotope signatures of precipitation have been observed in the present study.

Temperature effect

The isotopic fractionation is temperature dependent, and at lower temperatures the heavy species will be even less mobile than at higher temperatures. Therefore, rain in winter will have a hydrogen and oxygen isotopic composition slightly lighter (less heavy isotopes, more negative delta values) than in summer. The magnitude of this effect is 0.5‰/°C in $\delta^{18}O$ as global average but can vary considerably on a local scale (Mook 2005). This seasonal effect is most pronounced in precipitation itself and meanwhile used to calibrate General Circulation Models (GCM) of the atmosphere (Hoffmann *et al.* 2000). The seasonal temperature effect in stable isotopes is also discernible in the runoff signal in rivers (Königer *et al.* 2009), and in the soil zone (Königer *et al.* 2010). In groundwater this seasonal signal in stable isotopes is only discernible for very young groundwater (typically <4years), which makes this seasonality a useful tool in Karst systems.

Another temperature effect is more important when studying old groundwater; Pleistocene precipitation was recharging groundwater under colder conditions than today and these colder temperatures are reflected by isotope values that are typically 20‰ more negative in $\delta^{2}H$ for Pleistocene palaeowaters than for modern waters in Europe (Rozanski 1985). This corresponds to ≈2.5‰ more negative values in $\delta^{18}O$ for Pleistocene palaeowaters. The reason for this variation between the last glaciations and today is, however, not only due to temperature. Since during the last glaciations 3% of the global water volume was stored in the ice caps and since this ice-stored water was depleted in ^{18}O and ^{2}H (had more negative isotope values) the remaining ocean water was roughly 1.2‰ more positive than today. The actual temperature effect in Europe therefore corresponds to 3.7‰ in ^{18}O. The global effect will vary from place to place and only few palaeoclimate records exist on the southern hemisphere (Stute *et al.* 1995; Stute and Talma 1997). Some of these show positive and some negative shifts in ^{18}O values during the last ice-age, with no reliable record published to date for Australia. In any case, stable isotope measurements may allow discerning water recharged 10 ky ago from those recharged today. This is a useful application to confirm other tracers, like ^{14}C and ^{36}Cl, used to derive flow velocities.

A.1.2 Anthropogenic decadal transient tracers (^{3}H, CFCs, H1301, SF_6, ^{85}Kr)

The transient tracers of anthropogenic origin can be used for timescales of years to a few decades. These comprise ^{3}H, CFCs, H1301 and SF_6 and are called transient because their input concentration changes with time.

Tritium

Tritium (^{3}H) is the radioactive isotope of hydrogen and as such is part of the water molecule. Tritium is commonly measured in Tritium Units (TU), where one tritium unit corresponds to a ratio of ^{3}H to normal hydrogen of 10^{-18}, or to a tritium related specific radioactivity of 0.119 Bq per kg water. The ^{3}H presently observed predominantly in shallow groundwater is largely a result of atmospheric hydrogen bomb tests carried out in the sixties. Natural background of tritium in Australia is below 5 TU. Figure A.12 shows the time series of ^{3}H content in precipitation in Kaitoke, New Zealand, where the longest record on the southern hemisphere is available. For comparison, this record is displayed together with some stations in Australia (IAEA/WMO 2015). Evidently, the tritium fallout in precipitation in Australian stations was slightly higher around the bomb era than it was in New Zealand, which is due to a higher continental effect in Australia equivalent to higher dilution of the tritium input by oceanic (tritium-free) moisture in New Zealand. While the highest measurement in NZ was 76 TU in September 1966, some results in Adelaide, Melbourne, Brisbane and Alice Springs have values between 100 and 300 TU until 1972, which corresponds to the last French nuclear tests in the 100kt range in Moruroa. Unfortunately, while there is a recent evaluation of ^{3}H data in precipitation (Tadros *et al.* 2014), these contain no numerical values and have not been uploaded to the GNIP record as of August 2015 (IAEA/WMO 2015). Therefore, no Australian values are available for precipitation later than 1990.

Since ^{3}H is radioactive, Figure A.2 also displays how radioactive decay from some dates onward decreases the ^{3}H signal (blue lines). These lines give evidence that tritium alone cannot distinguish different recharge years uniquely, since rain from many different rainfall events would have 3-6 TU today. Therefore, although ^{3}H is radioactive, the way to use it as a groundwater tracer is largely like a dye, that is like CFCs and SF_6 are used, and hardly as a radioactive substance, as is the case for ^{14}C and ^{36}Cl (see below). A groundwater sample containing ^{3}H of more than 0.2 TU is an indication that part of the water recharged later than 1963, which corresponds to the peak in ^{3}H in precipitation in Figure A.2. *How much* of such young water is in the sample or *when* it was infiltrated cannot be uniquely quantified from one tritium measurement alone.

Krypton-85 (^{85}Kr)

The radioactive krypton isotope krypton-85 (^{85}Kr) may be described as “ash of the nuclear fire”. When uranium is disintegrated by controlled fission in nuclear reactors ^{85}Kr is one of the produced end products. Natural cosmogenic and sub-surface production of ^{85}Kr is negligible (Andrews *et al.* 1989). While the nuclear fuel rods stay intact and, in the reactor, ^{85}Kr is only released in trace amounts. Release of ^{85}Kr happens when the spent nuclear fuel rods are cut into pieces and dissolved in acid, which happens in nuclear reprocessing plants. This implies that there are only few sources for ^{85}Kr around the world and these are nearly completely on the northern hemisphere. Atmospheric activities of ^{85}Kr on the northern hemisphere therefore show characteristic spikes related to specific reprocessing events (Roß 2010). Activities on the southern hemisphere are on average 12% lower and hardly show the release-related spikes anymore. This is due to transport from north to south involving crossing the Inner Tropical Convergence Zone (ITCZ) with exchange times of 1.1 years, a process that smoothed the signal (Kersting 2018). ^{85}Kr is not influenced by underground production, which is sometimes observed for SF_6. As a noble gas it is not influenced by chemical reactions which may degrade CFCs. It shows the same applicability on the northern and southern hemisphere, in contrast to tritium which has a much smaller input function on the southern hemisphere. And since only the isotopic ratio of ^{85}Kr/Kr is evaluated, it does not rely on absolute concentrations to be measured and is not influenced by gas loss during sampling, which destroys the “age” information for CFCs, SF_6 and ^{3}H/^{3}He dating. As such it is the most robust and reliable tracer available and applicable on a time scale of decades (0-50 years of age). The only problem, complicated sampling techniques involving large amounts of water (1000L) and field degassing and complex long-time

radioactivity measurements, will be obsolete using routine measurements involving Atom Trap Trace Analysis (ATTA) in future (Jiang *et al.* 2012).

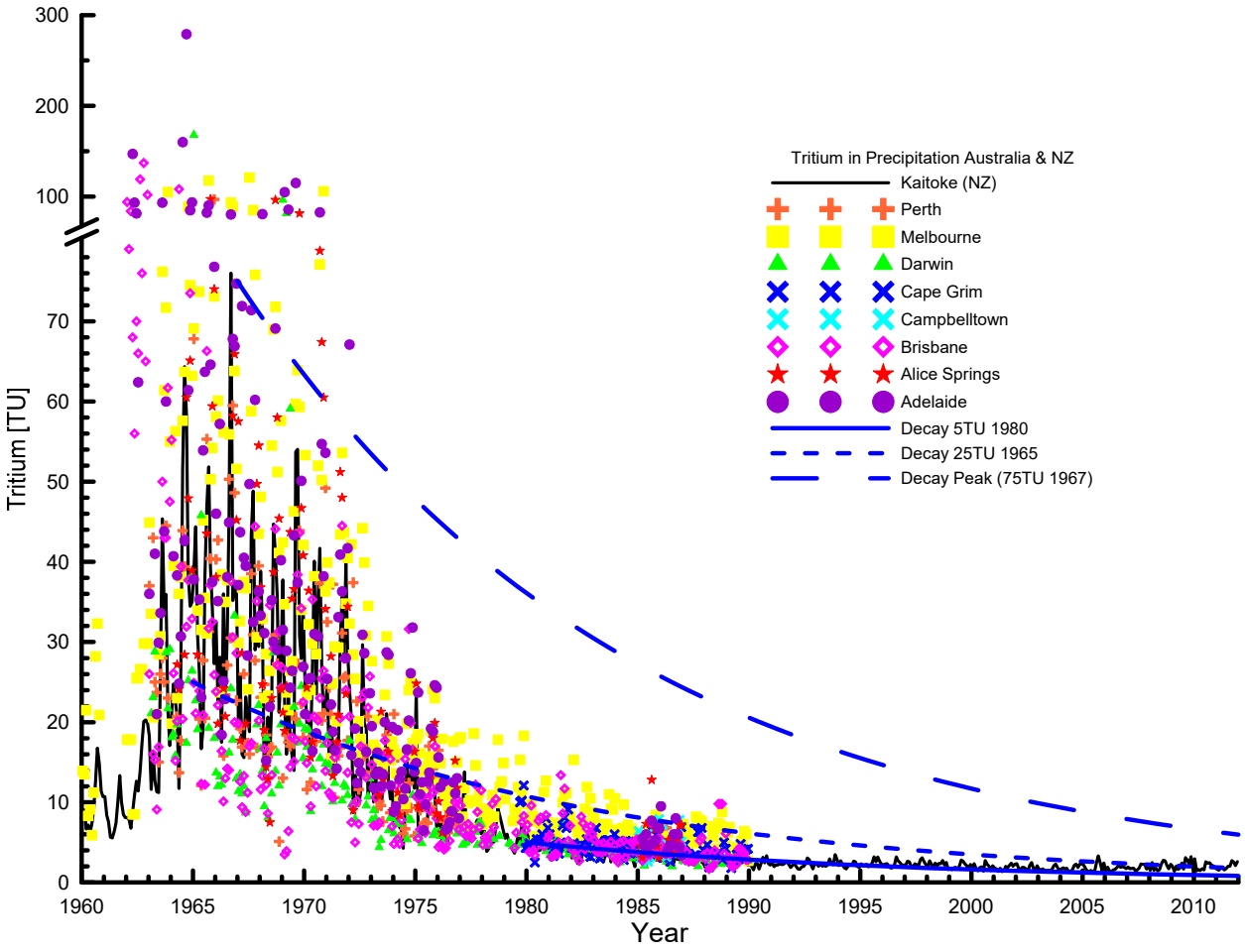

Figure A.2: Input function of tritium in Kaitoke and several Australian stations (IAEA/WMO 2015)

CFCs, H1301, SF_6

The environmental tracers Chlorofluorocarbons with the three species CFC-11, CFC-12 and CFC-113, as well as H1301 and sulphur hexafluoride (SF_6) are synthetic compounds, volatile at room temperature, that have been used for refrigeration, aerosols and electrical insulation since the 1940s. Their concentrations in the atmosphere increased steadily since then, reaching a peak in the late 1990s for CFCs and continuing to rise in the case of SF_6 (IAEA 2006). They can be measured down to levels of part per trillion using gas chromatography. During recharge the atmospheric concentration will be preserved in groundwater in accordance to their solubility (Henry's law). Figure A.3 illustrates this principle: known air concentrations (yellow panel left side) are converted with known infiltration temperatures to water concentrations (blue panel right side). Very simplified the infiltration year can then in principle be deduced from the measured concentrations: the horizontal lines in the right panel, symbolizing the measured concentrations, lead to a common infiltration year following the vertical line. In general terms, the mean residence time can be determined from the measured concentration, assuming an age distribution which needs assessment of the flow field and sampling condition (Suckow 2014a). If no information concerning the flow field is available, several model assumptions are tested against the measured values of different tracers in binary tracer plots.

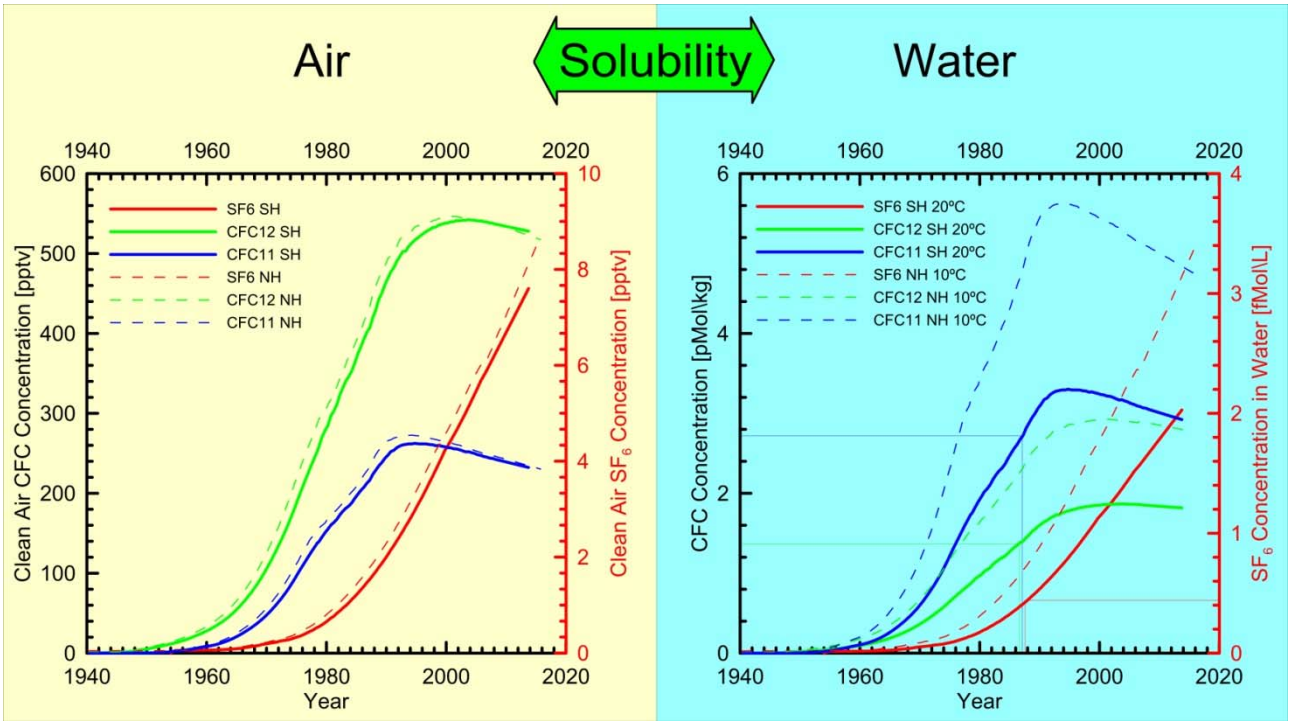

Figure A.3: The principle how CFCs and SF_6 are used to deduce time, SH and NH being 'southern' and 'northern' hemisphere respectively

In practice several processes can complicate the application of CFCs, H1301 and SF_6: the recharge temperature has to be deduced as soil temperature by adapting information from nearby meteorologic stations, or needs concentrations of all noble gases in another sample aliquot, which is not always possible. Sulphur hexafluoride is influenced strongly by excess air (Heaton and Vogel 1981), which can only be assessed by analysing concentrations of all noble gases in another sample aliquot. Furthermore, CFCs can be degraded in anaerobic groundwater and there is an ongoing discussion about natural underground production of SF_6 in the subsurface (Koh *et al.* 2007; Deeds *et al.* 2008; Rohden *et al.* 2010).

A.1.3 Radioactive tracers for old water (^{14}C, ^{36}Cl, ^{81}Kr)

Radioactive tracers used for the longer timescales are ^{14}C and ^{36}Cl. Both are cosmogenic nuclides, naturally produced in the upper atmosphere from cosmic radiation. For radioactive tracers with known or constant input function, an apparent age can be derived from concentrations using the equation of radioactive decay:

$$C(t) = C_0 \exp(-\lambda t) \Leftrightarrow t = \frac{1}{\lambda} \ln\left(\frac{C_0}{C(t)}\right) \qquad \text{(A2)}$$

Here t is the apparent age (Suckow 2014a), λ is the decay constant, corresponding to $\ln(2)/t_{1/2}$ and $t_{1/2}$ is the half-life. $C(t)$ is the measured concentration in the sample and C_0 the concentration at recharge. For most groundwater tracers C_0 is insufficiently known *a priori* and needs to be determined in the recharge area. Such an empirical determination involves a cross-plot with a tracer for the next younger timescale (Suckow 2013). For ^{14}C this may be ^{3}H, CFCs, H1301, SF_6 and ^{85}Kr. For the initial value of $^{36}Cl/Cl$, ^{14}C can be favourably used as young tracer. For ^{14}C in combination with CFCs or ^{3}H, input functions for both tracers can be compared with measured values on a dual tracer plot and a constant factor to the atmospheric ^{14}C ratio can be fitted, as successfully demonstrated in Lamontagne *et al.* (2015) or Taylor *et al.* (2015). For $^{36}Cl/Cl$ the initial value would be obtained from those samples that still contain radiocarbon, if mixtures between water of different age can be excluded. Typical applications allow the determination of timescales up to five half-lives, so how far a tracer can be used into the past strongly depends on the kind of tracer.

Radiocarbon

Radiocarbon or ^{14}C is probably the most used tracer for 'dating' groundwater in Australia. Radiocarbon has a half-life of 5730 years, which allows determining flow velocities and constraining timescales between some thousand and approximately 30,000 years. For ^{14}C, the actually measured value is not the absolute concentration of ^{14}C in water, but the isotopic ratio of $^{14}C/^{12}C$ in the Total Dissolved Inorganic Carbon (TDIC), which is the sum of dissolved CO_2, HCO_3^- and CO_3^{2-}. The unit for this ratio of $^{14}C/^{12}C$ was pMC (percent Modern Carbon, (Stuiver and Polach 1977)) or more recently %, where 100% corresponds to the atmospheric $^{14}C/^{12}C$ ratio in 1950 (Mook and Plicht 1999). The basic assumption is that the isotopic ratio of $^{14}C/^{12}C$ changes only by radioactive decay of ^{14}C. Radiocarbon can be measured very precisely (better 0.1%) and with a very low detection limit of less than 0.1% via Accelerator Mass Spectrometry (AMS). In practical groundwater studies, especially in deep aquifers, a few % of ^{14}C should be considered as practical detection limit, since leaky casings or small hydraulic connections in the bore annulus can never completely be excluded.

Very often however, radioactive decay is not the only process decreasing ^{14}C in groundwater. All geochemical changes increasing TDIC or alkalinity can potentially decrease $^{14}C/^{12}C$ (Plummer and Glynn 2013). This is of special importance when fossil sources of carbon are available, as is obviously the case in coal seam gas districts. Also for the GAB as a whole, an increase in alkalinity (and hence TDIC) is known with flow distance (Radke *et al.* 2000; Ransley and Smerdon 2012). A possibility to avoid this geochemical influence, which causes the water samples to look 'too old', is to consider only the concentration of ^{14}C (e.g. as ^{14}C atoms per litre water), in analogy to general practice for ^{36}Cl (see below). This case is easier than ^{36}Cl, because underground production of ^{14}C is negligible and therefore most underground sources of carbon can be considered ^{14}C-free and would not influence the ^{14}C concentration. If N_A is the Avogadro constant, TDIC is expressed as mmol/L carbon, $^{14}C/^{12}C$ in % and ^{14}C as atoms/L, then the recalculation of % into atoms/L ^{14}C is:

$$^{14}\mathrm{C}[atoms/L] = \frac{^{14}\mathrm{C}}{^{12}\mathrm{C}}[\%]\frac{1}{100}\frac{TDIC}{1000}N_A 1.175 \cdot 10^{-12} \qquad \text{(A3)}$$

The number $1.175 \cdot 10^{-12}$ corresponds to the isotope ratio $^{14}C/^{12}C$ of modern carbon, which can be calculated from the specific activity of 0.226 Bq/gC and its physical half-life of 5730 years (Mook and Plicht 1999).

There are many geochemical 'correction' models which all are designed to derive the initial 'no decay' concentration C_0 for Equation 3. Since they will not be applied in this report they are not discussed in detail, and the interested reader is referred to the detailed description by Plummer and Glynn (2013).

Chlorine-36

The application of ^{36}Cl is very analogous to ^{14}C and the basic idea also follows Equation 3, with the important difference that the half-life of ^{36}Cl is much longer (301,000±4,000 years) (Phillips 2013). The applicable time range therefore is between 50,000 and approximately one million years. This means ^{36}Cl behaves in comparison to ^{14}C similarly as ^{14}C behaves in comparison to ^{3}H. Also, in the case of ^{36}Cl, the actually measured value is the isotopic ratio of $^{36}Cl/Cl$. A general complication of ^{36}Cl is that it is produced in the subsurface (Andrews *et al.* 1989), mainly by neutron capture of ^{35}Cl and to a much smaller extent of potassium-39 (^{39}K). The thermal neutrons in both cases come from uranium (U) and thorium (Th) in the aquifer. As a result of this underground production, the $^{36}Cl/Cl$ ratio normally does not approach zero but a non-zero value that must be determined empirically in each aquifer. Chloride (Cl) as the carrier for the dating isotope has the advantage of being a much more conservative substance in groundwater than TDIC is for ^{14}C. Nevertheless, already in the first applications in the GAB the basic problems of dilution with 'dead' Cl and underground production of ^{36}Cl were discussed (Bentley *et al.* 1986). The Cl concentration along the flow path is necessary information for the interpretation of ^{36}Cl, as is the knowledge of the final value, to which the $^{36}Cl/Cl$ ratio develops for groundwater being much older than the dating range of ^{36}Cl. Data interpretation typically involves a discussion of plots of $^{36}Cl/Cl$ versus Cl concentration, $^{36}Cl/Cl$ versus ^{36}Cl concentration and ^{36}Cl concentration versus Cl concentration, as discussed in detail by Phillips (2013). In

this book chapter, also a sufficiently general model of ^{36}Cl evolution in groundwater is described, which will be summarized next.

The Phillips Model for ^{36}Cl

In Chapter 6 of IAEA (2013) Fred M. Phillips described an easy mass balance equation for the absolute ^{36}Cl concentration in an aquifer. The model incorporates radioactive decay of the recharged ^{36}Cl, underground production in the aquifer towards a secular equilibrium ratio of ^{36}Cl/Cl and an additional source of chloride, like e.g. diffusion from an adjacent aquitard, which may have another ^{36}Cl/Cl ratio in secular equilibrium. The formula for the ^{36}Cl evolution with time is:

$$^{36}\mathrm{Cl}(t) = R_m \mathrm{Cl}_m = R_r \mathrm{Cl}_r \exp(-\lambda t) + \left[R_1 \mathrm{Cl}_r + \frac{F_{\mathrm{Cl}}}{\lambda}(R_2 - R_1)\right]\left(1 - \exp(-\lambda t)\right) + R_2 F_{\mathrm{Cl}} t \quad \text{(A4)}$$

In this formula ^{36}Cl(t) is the absolute ^{36}Cl concentration [atoms/L], which corresponds to the measured ^{36}Cl/Cl ratio (R_m) multiplied with the measured chloride concentration Cl_m [atoms/L]. Further R_r, R_1 and R_2 are the isotopic ratios of ^{36}Cl/Cl in the recharge area (r), in secular equilibrium in the aquifer (1) and the adjacent aquitard (2) respectively. F_{Cl} is the flux of chloride from the aquitard to the aquifer [atoms/(L·year)], and λ is the decay constant of ^{36}Cl.

The model is general enough, that it can be applied to radiocarbon as well. In this case R_1 and R_2 are both zero, since no underground production takes place for ^{14}C, and it describes the dilution of the (measured) ^{14}C/C ratio with 'dead' TDIC.

Krypton-81 (^{81}Kr)

The application of ^{81}Kr is in complete analogy to ^{14}C and ^{36}Cl and the basic idea also follows Equation A2. Also, the time range of ^{81}Kr is nearly identical to ^{36}Cl, since it has a half-life of 229 000 y. However, ^{81}Kr does not show any of the problems in application. As a noble gas it is not influenced by any chemical reaction. The abundance of stable krypton in groundwater varies only due to infiltration conditions, unless one samples in very extreme brine environments (Suckow and Sonntag 1993), which means that "dilution" with "dead" Kr like in the case of ^{14}C with C and ^{36}Cl with Cl can be excluded. As far as known to present, also underground production is negligible (Andrews *et al.* 1989; Andrews *et al.* 1991), although most recent results indicate differently with underground production from spontaneous fission of uranium (Purtschert *et al.* 2017). This makes ^{81}Kr the most ideal and most robust tracer for old groundwater on time scales from 50ky to 1My. Nevertheless, to date there are less than 100 results of ^{81}Kr for groundwater applications published the literature, with only one study in Australia (Collon *et al.* 2000; Lehmann *et al.* 2003). The reason for this scarcity is that the routine measurement of ^{81}Kr is only possible for a few years now, with the event of the Atom Trap Trace Analysis technology (Lu *et al.* 2014), and to date only two laboratories world-wide can measure the samples. Sampling is still comparably complex, since it involves vacuum gas extraction in the field, collecting 40 L of gas from more than 1000 L of water. To date CSIRO Land and Water in Urrbrae is the only institution in Australia that can take the samples and process the gases to a pure krypton fraction for measurement. In any case it is necessary to support the findings from ^{14}C, ^{36}Cl and ^{81}Kr with other tracers such as helium.

A.1.4 Stable Noble gases

The five stable noble gases helium, neon, argon, krypton and xenon are the most versatile tracers available. Helium increases with time and allows to derive age estimates, to investigate aquifer inter-connectivity and to sensitively detect fluid flow from deeper layers and having a closer look on the origin of these fluids using the ^{3}He/^{4}He isotope ratio. The heavier noble gases characterize recharge conditions, such as infiltration temperature (mainly Ar, Kr, Xe) and excess air (mainly Ne). This is valuable information in itself to understand groundwater systems, but also is necessary information to interpret the results of other tracers, such as the CFCs, H1301 and SF6.

Helium as a tracer

The helium isotope ^{4}He is produced in the underground from the U/Th decay chains since these two elements are abundantly present at ppm concentration level in the rock matrix. Every alpha particle from the decay chains contributes a ^{4}He atom and most of these are released to the groundwater and pore water (Torgersen and Stute 2013). Figure A.4 displays the decay chain of ^{238}U (Suckow 2009) and each yellow arrow in it represents an alpha particle, corresponding to the creation of a helium atom. One atom of ^{238}U therefore will produce a total of eight ^{4}He atoms when decaying to ^{206}Pb. The analogue process happens with ^{232}Th, releasing six helium atoms during decay to ^{208}Pb.

The easiest, but seldom fulfilled assumption is that ^{4}He in groundwater increases constantly with time according to the formula (Andrews and Lee 1979):

$$\frac{dc(^4\mathrm{He})}{dt} = \frac{\rho_R}{\rho_W} \Lambda \frac{1-n_{tot}}{n_{eff}} (1.19 \cdot 10^{-13}[\mathrm{U}] + 2.88 \cdot 10^{-14}[\mathrm{Th}]) \quad \text{(A5)}$$

Here $c(^4\mathrm{He})$ is the measured concentration of ^{4}He in groundwater and $dc(^4\mathrm{He})/dt$ is its increase per year in [cc(STP)/(g·year)]. ρ_R and ρ_W are the rock and water densities, Λ is a release factor of helium from the rock which empirically is always 1, and n_{tot} and n_{eff} are the total and effective porosities valid for the groundwater flow. Uranium [U] and thorium [Th] concentrations in this formula are given as ppm. Typical uranium and thorium concentrations in aquifer rocks are in the range of fractions of a ppm to several ppm resulting in typical production rates of $1 \cdot 10^{-13}$ to $5 \cdot 10^{-11}$ cc(STP)/(g·year). Values for the Hutton and Precipice Sandstones in the Surat basin range from 3–6 ppm and 3–8 ppm for U and Th respectively and together with estimates of porosity and rock density (APLNG 2014; Smith 2015) result in an in situ production rate of $1 \cdot 10^{-11}$ cc(STP)/(g·year). The concentration of ^{4}He in solubility equilibrium is ca. $5 \cdot 10^{-8}$ cc(STP)/g and can be determined with an accuracy of better than 10%. The in situ produced helium component would therefore be distinguishable from solubility equilibrium earliest after 500-1000 years and then increase linearly with time. This makes helium a dating tracer that has no theoretical upper limit of application.

As outlined in Torgersen and Stute (2013) this linear increase is hardly ever fulfilled and influx of helium from aquitards and underlying formations as well as diffusive losses of helium from the aquifer to surrounding formations dominate the concentration behaviour with time. Therefore, any interpretation of helium must be treated at least with as much caution as for ^{14}C and all tracers have to be combined with each other to derive estimates of flow rates and direction.

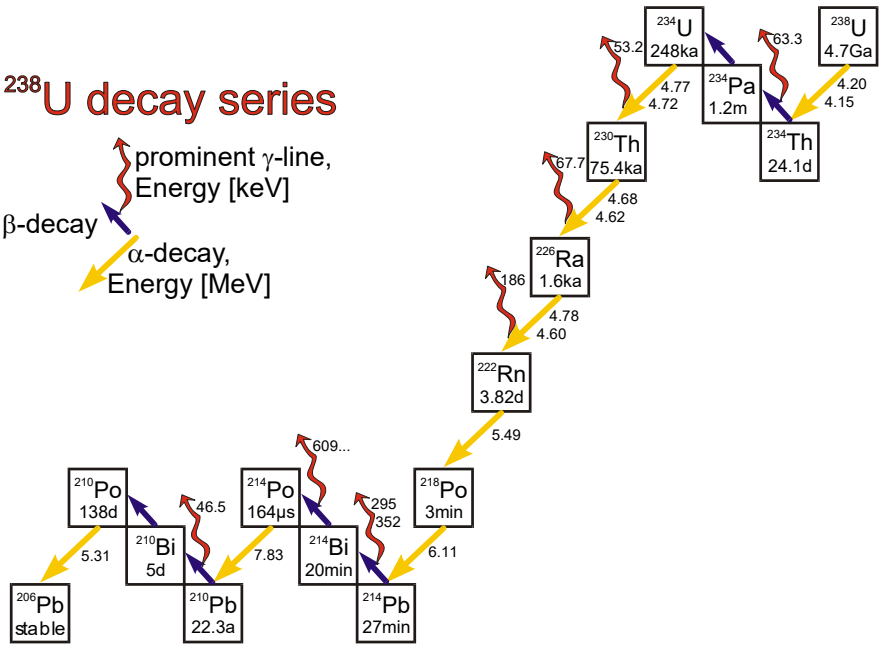

Figure A.4: Decay chain of ^{238}U (Suckow 2009), providing a total of 8 helium atoms per decaying ^{238}U (yellow arrows)

Helium isotopes in groundwater

Helium is the element with by far the largest natural variation in isotopic composition on earth (Figure A.5). Most of the isotope ^{3}He on earth is of primordial origin, that is: it originates from the accumulation of planet earth during formation of the solar system. From meteorite measurements it is known that this primordial helium of cosmic origin has a $^{3}He/^{4}He$ isotope ratio in the range of 10^{-4}. This primordial helium is stored in the deep earth and manifests itself as measurable $^{3}He/^{4}He$ ratio in Mid-Ocean Ridge basalt (MORB) or in hot spot volcanoes in the range of 10^{-5}. Earth's atmosphere has an isotope ration of $1.4 \cdot 10^{-6}$, which is also the primary reference material in all noble gas measurements. The prior discussed production of "crustal" helium creates a much higher content of ^{4}He and is in the range of 10^{-8}.

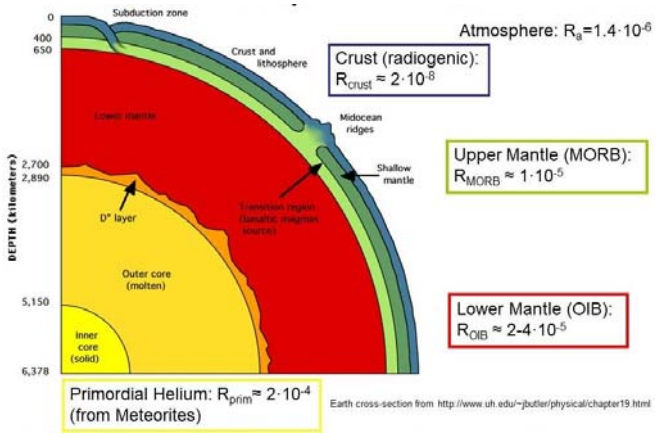

Figure A.5: Helium Isotope Ratios in Planet Earth.

The simplest classification of the origin of helium in groundwater is possible, if the measured helium isotope ratio is plotted against the ratio of neon/helium measured in the sample, which is a simplified version of the Weise plot (Weise and Moser 1987), as discussed in (Suckow 2013) and displayed in Figure A.6. Here the blue line corresponds to the different Ne/He ratios at different temperatures, which all have the same $^{3}He/^{4}He$ isotope ratio, since helium has no temperature dependent isotope fractionation. The

black line is the isotopic mixing line leading from solubility equilibrium to the crustal helium end-member. The violet line indicates a mixing line with one possible addition of primordial helium. The green line describes the addition of pure ^{3}He originating from the radioactive decay of tritium. This green line is important on the northern hemisphere where tritium input in precipitation was a factor of 50 more than on the southern hemisphere. However, all these lines are pure processes, which in nature are rarely visible this way but mostly characterized by areas. These more diffuse signals originate from mixing processes, as demonstrated by the coloured ellipses and the data displayed, which are from a real study in Hungary where all these processes were observable (Stute *et al.* 1992).

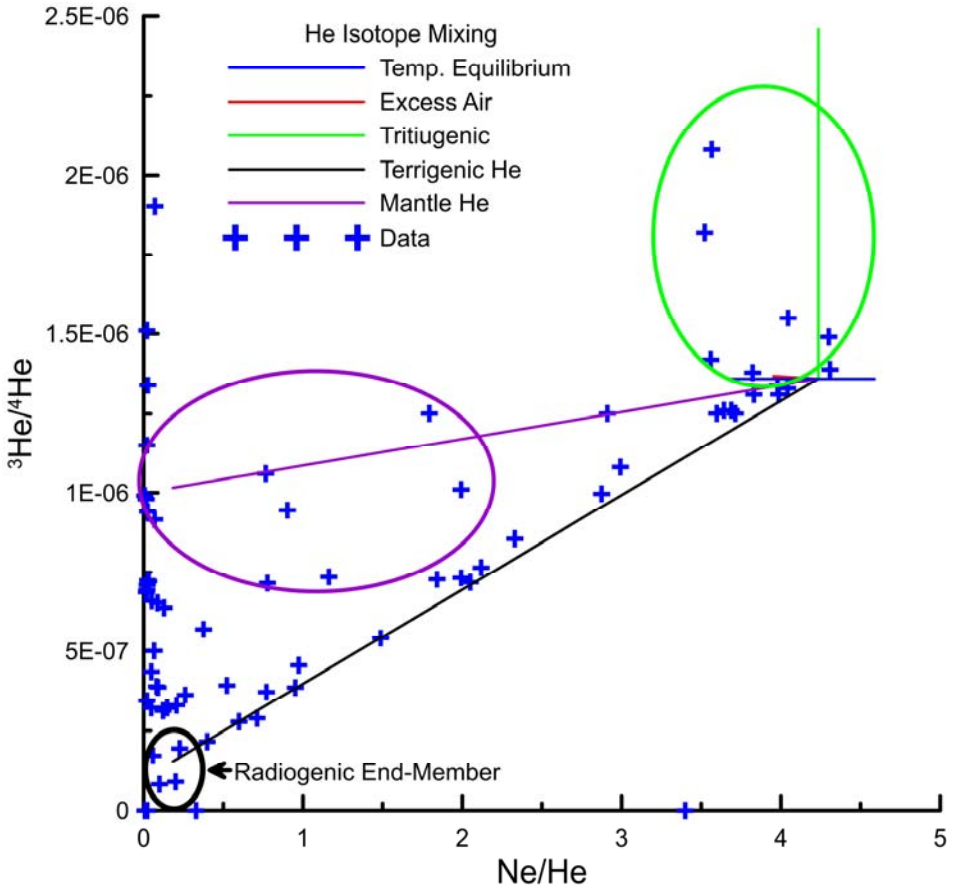

Figure A.6: Weise plot demonstrating the origin of helium in groundwater.
The coloured lines and ellipses characterize helium originating from solubility equilibrium (blue) from mantle (purple) or crustal sources (black) or from tritiugenic helium (green).

Heavy noble gases

The heavier noble gases Ne, Ar, Kr, and Xe have very different temperature dependency of their solubility in water (Figure A.7). The solubility here corresponds to concentrations in water when exposed to one atmosphere of the gas in question. While the concentration of neon varies only by 30% between 0°C and 50°C, the concentration of xenon in the same range varies by nearly a factor of four. In principle this allows to directly derive the infiltration temperature by measuring the noble gas concentrations (horizontal dashed lines) and deriving the infiltration temperature if the noble gases Ar, Kr and Xe agree. In practice there is an additional phenomenon at play which is called “excess air” (Heaton and Vogel 1981).

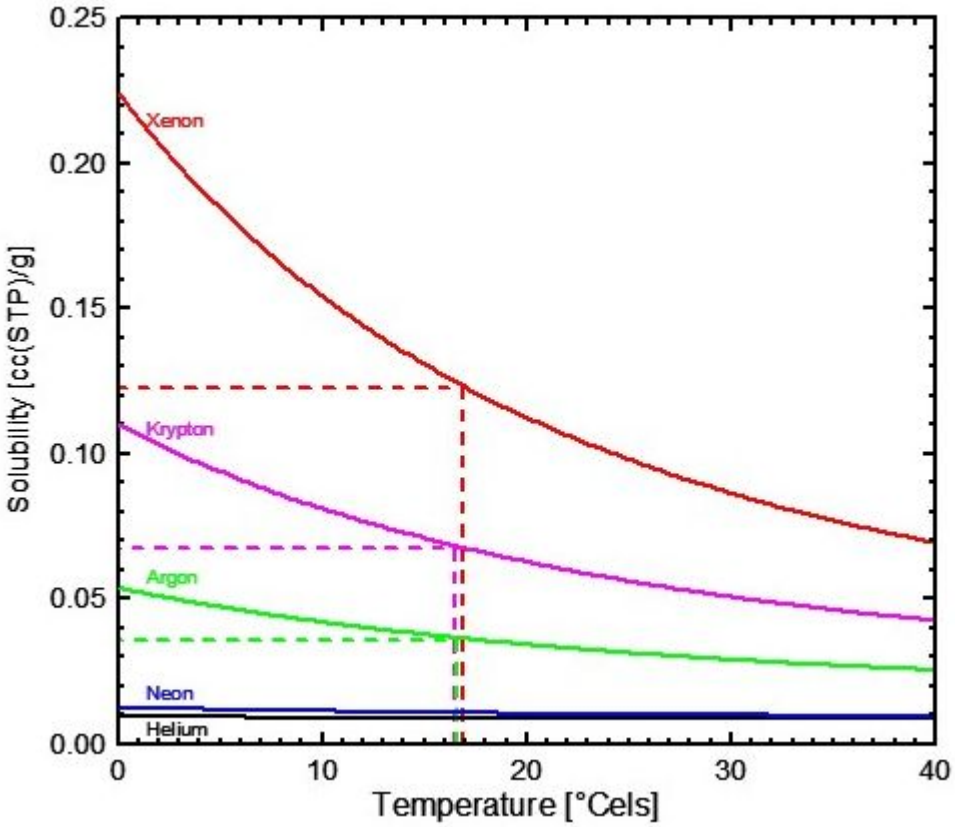

Figure A.7: Solubility of the noble gases as function of temperature in fresh water at sea level.

Whenever the water table rises in a porous medium, air bubbles will be trapped (Figure A.8). If these bubbles are small enough, they will implode under their own capillary force. In case they are larger, they will still be under pressure and partly dissolve. This creates a surplus of noble gases on top of the solubility equilibrium, which has the noble gas composition of air. Since the solubility of xenon is larger than that of neon, the effect of this surplus of air will be relatively larger on neon than on xenon. The amount of xenon measured in groundwater is therefore the best indicator for the infiltration temperature and the amount of neon the best indicator for excess air. In practice the amount of excess air is determined by a fitting algorithm with the infiltration temperature, excess air and sometimes also fractionation factors or infiltration parameters like altitude or salinity as fitting parameter (Jung and Aeschbach 2018).

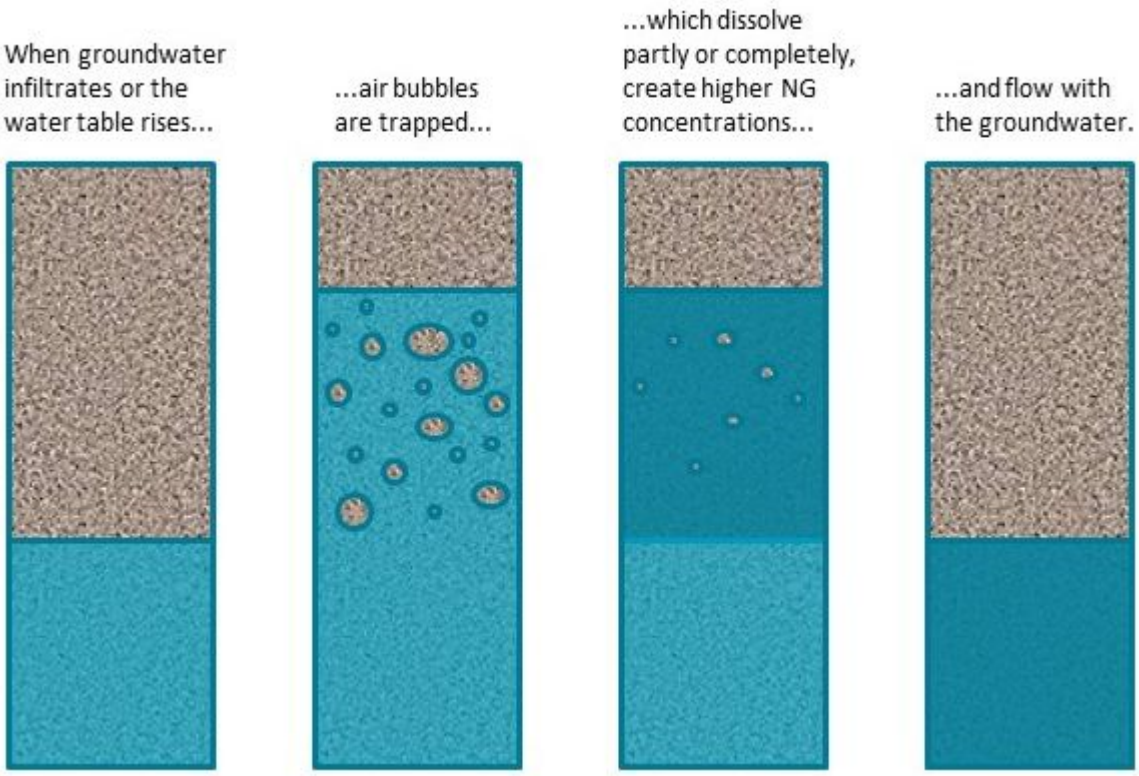

Figure A.8: The process of Excess Air formation.

Dissolved Nitrogen (N_2)

While nitrogen is not a noble gas, it is nevertheless determined in the raw gas fraction of a noble gas measurement. Nitrogen is often existing in groundwater in excess compared to the solubility concentration and excess air. The general assumption is that this additional nitrogen is a product of denitrification of nitrate. This nitrate can be a natural product (e.g. from acacia or termites) or an anthropogenic input (e.g. from fertilizer). Concentrations of dissolved nitrogen can therefore assess the degree of denitrification, and with this a useful tool to asses natural ecological parameters like the historical vegetation, or anthropogenic impact on environmental processes.

A.2 'Age' of groundwater is not a scalar but a distribution

Any groundwater sample contains not only one 'age', but many different ages (see Figure A.9 originating from (Torgersen *et al.* 2013)). The idea of an idealized age is displayed in Figure A.9 A. Wider age distributions are caused by diffusion and dispersion along a single flow path (Figure A.9 B). More realistically, flow paths from different parts of the recharge area start in the recharge area and meet in the well, causing a wider distribution than expected from diffusion and dispersion alone (Figure A.9 C). Furthermore, exchange with the aquitard matrix can strongly influence the age distribution (Figure A.9 D), which is discussed in more detail in the next paragraph. These processes together can create large discrepancies between apparent ages calculated for different tracers. This is since each tracer 'sees' only a small part of the whole age distribution. Any calculation according to formulas like Equation A3 therefore gives only an 'apparent age', and these apparent ages can differ easily by a factor of 2 or more for different tracers (Suckow 2013, 2014a). The magnitude of the discrepancy between these apparent ages depends on the flow regime and on the sampling conditions.

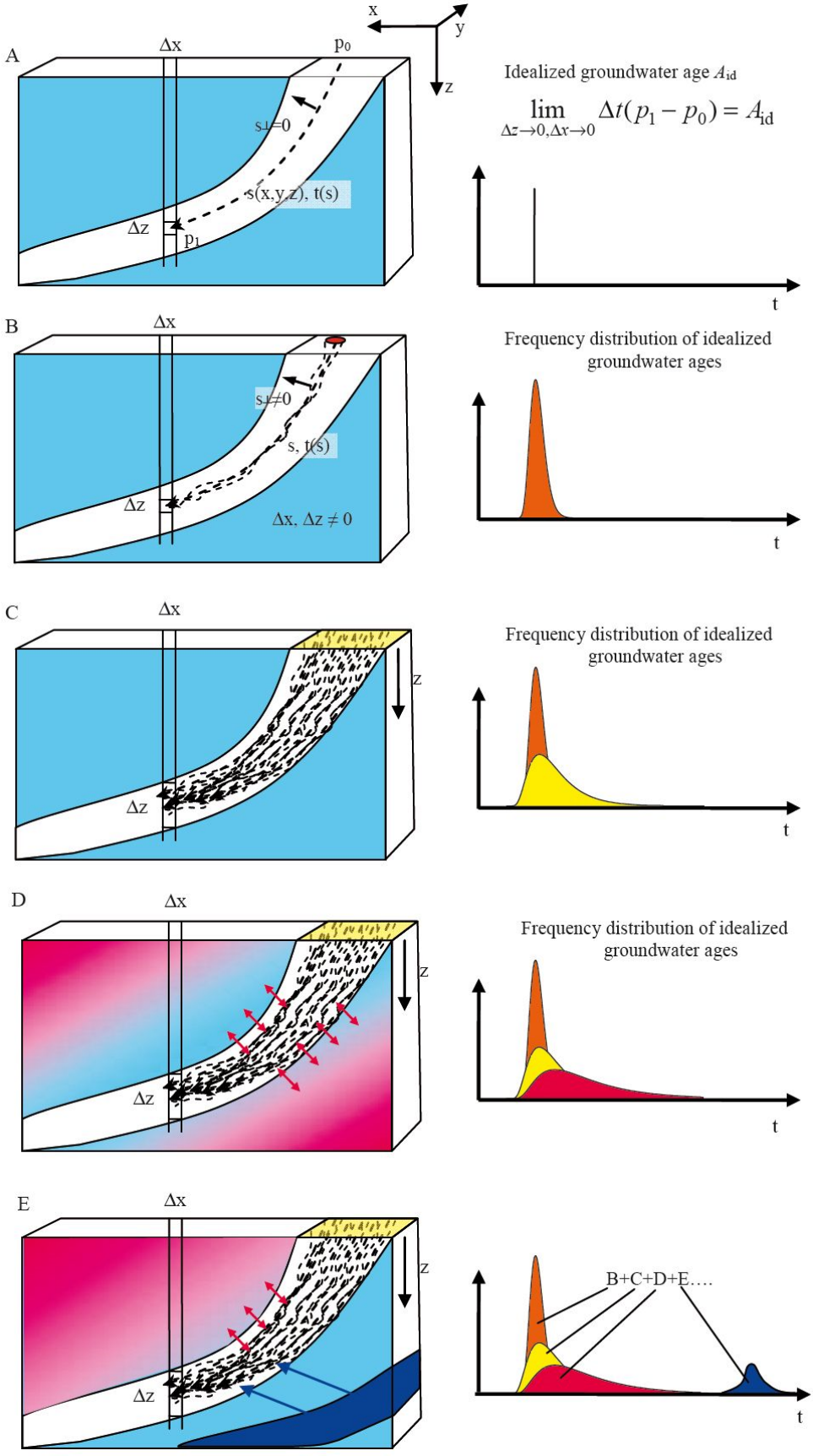

Figure A.9: Spreading of age distributions due to different processes relevant in groundwater (Torgersen et al. 2013)

However, all these processes A-D keep the age distribution in a uni-modal shape with only one maximum in the distribution. This is even too simplistic an assumption in reality. On long flow paths like several tens of kilometres, waters from different aquifers can mix, e.g. by the influence of faults or by windows in the aquitards separating the aquifers. This can cause bimodal or multimodal age distributions and render any

apparent age meaningless (Figure A.9 E). Further downstream of such a confluence, hydrodynamic dispersion can then again spread out the difference between the single peaks and the age distribution can be uni-modal again, but much wider. This illustrates why the calculation of apparent ages in most cases is not a very useful approach (Suckow 2014a) and is not followed in this report. Instead, different flow assumptions are tested against a multitude of tracers (Suckow 2013). Hereby it is necessary to always combine the tracers for 'old' groundwater (^{14}C, ^{4}He, ^{36}Cl) with those for young groundwater (CFCs, SF_6, ^{3}H) to de-convolute admixtures of young water in the sample (IAEA 2013).

A.3 Tracers in double porosity systems

Environmental tracers show special features in double porosity systems that may severely distort the derived flow velocity or apparent age. Double porosity here is defined as any situation in which the active flow system (the aquifer) can exchange any solutes (tracers) by diffusion with another stagnant part of the aquifer system. Such stagnant zones may exist in the aquifer itself (flow in fractures surrounding a stagnant matrix; preferential flow due to sedimentological differences), or these may be adjacent aquitards. In any case the flow in these zones is negligibly slow as compared to the aquifer. If the tracer concentration is lower in the stagnant zone as compared to the active flow zone, then the tracer is lost by diffusion into the stagnant zones. The length *L* is the distance how far the tracer can penetrate into the stagnant zone in a certain amount of time, and is only dependent on time *t* and the effective diffusion constant *D'* (Einstein 1905):

$$L(t) \cong \sqrt{D't} \qquad \text{(A6)}$$

Variations of *D'* between different tracers in free water are up to a factor of 7 (e.g. at 10°C: $5.7 \cdot 10^{-9}$ m^2/s for ^{4}He (Jähne *et al.* 1987) and $0.8 \cdot 10^{-9}$ m^2/s for SF_6 (King and Saltzman 1995)). Diffusion rates decrease within the pore space of sediments due to tortuosity and this factor depends on details of the sediment properties but is normally also in the range of a factor of 10 or less. Furthermore, this tortuosity factor applies to all tracers the same way. Therefore, the length *L(t)* is mainly a function of time, and the differences in diffusion coefficients between tracers are of minor importance. If one assumes an aquifer of thickness *a* separated by stagnant layers (aquitards) of thickness *b*, then Figure A.10 illustrates the principle of tracer diffusion into the pore space (Purtschert *et al.* 2013).

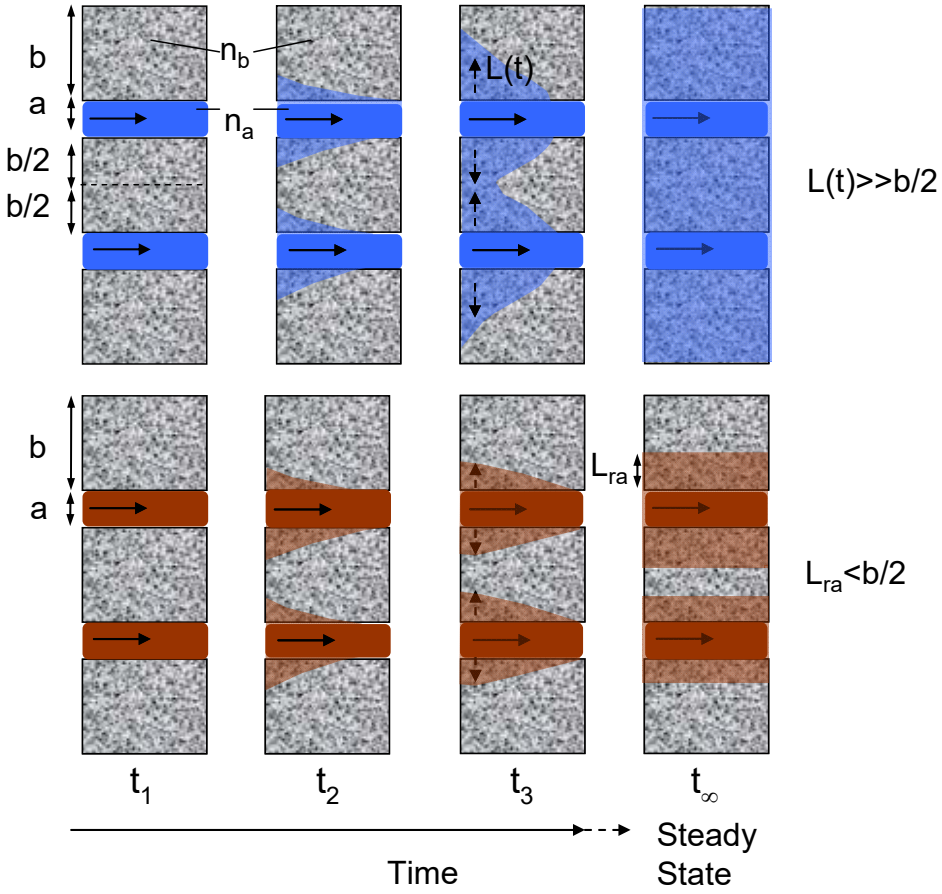

Figure A.10: Tracer retardation by matrix diffusive loss into stagnant zones (Purtschert *et al.* 2013)

Due to the diffusive loss into the aquitard, any environmental tracer that comes into the aquifer only with precipitation will result in a lower measured value if double porosity is important. This is true for ^{3}H, CFCs, SF_6, ^{14}C and ^{36}Cl and will result in a higher apparent age than the 'true' hydraulic age of the water. How much tracer is lost to the aquitard will depend on time (because *L(t)* depends on time, see Equation A6 and the left part of Figure A.10) and for long times on the ratio of water volume in the stagnant zone to water volume in the aquifer (right part of Figure A.10). Also, for a tracer produced in the underground, like ^{4}He, the groundwater will 'see' the much larger production volume of aquifer plus thickness $2 \cdot L(t)$ of the aquitard of which ^{4}He produced from uranium and thorium decay is released to the flowing groundwater. Again, this will result in a higher apparent age than the 'true' hydraulic age of the water.

For a simple one-dimensional system of one thin aquifer in an extended aquitard that observes no flow but only molecular diffusion, Sudicky and Frind (1981) gave an analytic solution for the relationship of steady-state tracer concentration in the aquifer with distance:

$$C(x) = C_0 \cdot \exp\left(x \cdot \left(\frac{v}{2D} - \sqrt{\left(\frac{v}{2D}\right)^2 + \frac{\lambda}{D} + \frac{\sqrt{\lambda D'}}{D} \cdot \frac{n_b}{a \cdot n_a}} \right) \right) \qquad \text{(A7)}$$

Here c_0 is the initial tracer concentration at $x=0$, v is the flow velocity in the aquifer, λ the decay constant of the tracer, a the thickness of the aquifer and n_a and n_b are the porosities of aquifer and stagnant phases, respectively. D is the sum of hydrodynamic dispersion and diffusion in the aquifer, $D=\alpha_L \cdot v + D'$, where α_L is the dispersivity and D' the molecular diffusion of the tracer. The net effect of tracer loss by diffusion from the aquifer into the surrounding aquitard is that the radioactive tracer decreases (much) faster than according to radioactive decay. The effect can be easily a factor of ten or more, depending on aquifer thickness and travel distance. The resulting distribution of tracer versus distance is still exponential, as

would be expected without the double-porosity effect. This makes it impossible to detect the importance of this effect from the tracer measurements alone if only *one* tracer is measured versus distance. Any apparent age as derived from a tracer like ^{14}C or ^{36}Cl would be larger than the flow time of water from the recharge to the sampling point.

This means, that the tracer loss manifests itself like a retardation factor *R*, in a similar manner as when chemical sorption occurs. This apparent retardation factor depends on the true hydraulic water age (represented as *t*), which in a steady state flow system is equivalent to flow distance *x* and on the ratio of available total volume to active flow volume (Maloszewski and Zuber 1985; Purtschert *et al.* 2013):

$$R(t) \cong \frac{a \cdot n_a + 2 \cdot L(t) \cdot n_b}{a \cdot n_a} \tag{A8}$$

Here n_a and n_b are the porosities of the aquifer and the stagnant zones respectively. Obviously, this retardation factor is time dependent; for very short times it is negligible ($L(t)$=0 in Equation 7, so R=1 at t=0) and increases with the square root of time. For a stable tracer the loss into the stagnant zones – and therefore the retardation factor – can be very large, because it can penetrate also into very thick stagnant zones. A radioactive tracer, however, may not have enough time to penetrate a thick stagnant zone *b*, because it decays earlier (lower part of Figure A.10). Therefore, for a radioactive tracer the maximum length L_{ra} to which it can penetrate a stagnant layer, is dependent on the decay constant λ:

$$L_{ra} \cong \sqrt{\frac{D'}{\lambda}} \tag{A9}$$

Obviously, this maximum distance L_{ra} is the larger, the longer the half-life of the tracer is. Therefore, in aquifer systems with very large stagnant layers like the Hutton Sandstone in the Surat Basin, also the *maximum* possible retardation factor increases with half live according to the following sequence:

$$R(t) \cong \frac{a \cdot n_a + 2 \cdot L_{ra} \cdot n_b}{a \cdot n_a}; \qquad R_{^3H} << R_{^{14}C} << R_{^{36}Cl} \tag{A10}$$

One has to be aware that this sequence describes only the *maximum* retardation factor – after a flow distance *x* when the most short lived tracer (usually ^3H) reaches its L_{ra}, the retardation factors of the longer lived tracers (^{14}C and ^{36}Cl) will be nearly identical (distinguishable only due to the different diffusion constants in Equation A9), because for them $L(t)$ is still much smaller than L_{ra}. As a further consequence, this retardation factor is only constant at one point along the flow path in a system in steady state towards flow and transport. In any transient or stationary system, the retardation factor will increase along the flow path until either L_{ra} is reached or until tracer diffusion created a homogeneous concentration in aquifer and pore space (right state in Figure A.10). After this point in time and space no further net tracer loss from the aquifer will occur for a stable tracer, but still for a radioactive tracer.

The Sudicky model of Equation A7 fitted with two tracers for the same flow velocity allows deriving the total amount of water flowing within a deeper aquifer formation. This can be understood when re-arranging Equation 8 to the following form:

$$C(x) = C_0 \cdot \exp\left(\frac{x \cdot v}{2D}\left(1 - \sqrt{1 + \frac{4D}{v} \cdot \left(\frac{\lambda}{v} + \sqrt{\lambda D'} \cdot \frac{n_b}{a \cdot v \cdot n_a}\right)}\right)\right) \tag{A11}$$

Here the terms in the exponential function have the following meaning: The term xv/D corresponds to the longitudinal Peclet number within the aquifer and describes how the tracer is spread within the aquifer in

flow direction by dispersion. As mentioned earlier, dispersion is the product of dispersivity and flow velocity plus diffusion: $D=\alpha_L \cdot v+D'$. Since on the scales in discussion x is on the order of many 10,000 m and α_L is on the order of many meter, D' can be neglected and the term $xv/2D$ decomposes to $x/2\alpha_L$. The same holds true for the term $4D/v$ which decomposes to $4\alpha_L$. This allows for a Taylor development of the root in the exponential:

$$\sqrt{1+x} \approx 1+\frac{1}{2}x-\frac{1}{8}x^2+\cdots \qquad \text{(A12)}$$

Which, together with the transformations of dispersion above allows us to transform the formula further:

$$C(x) \approx C_0 \cdot \exp\left(-x \cdot \frac{\lambda}{v}-x \cdot \sqrt{\lambda D'} \cdot \frac{n_b}{a \cdot v \cdot n_a}\right) \qquad \text{(A13)}$$

Note that this is independent of longitudinal dispersivity α_L, which explains the insensitivity of the Sudicky formula towards this parameter. As a result, in the case where the second porosity can be neglected (n_b=0) the whole exponential can be very well approximated by $\exp(-x\lambda/v)$ which corresponds to the transport of a radioactive tracer in a long tube. In cases where diffusion into the matrix is dominant for tracer loss, only the last term in the exponential becomes important. Here $\lambda D'$ is a measure of the length of matrix diffusion that is important for the tracer. This is largest for ^{36}Cl and is composed of physical constants and therefore not part of the fitting process and independent of the flow velocity or aquifer geometry. The term $n_b/(a \cdot v \cdot n_a)$ dominates the exponential decrease of tracer along the flow path and the fitting. The term $a \cdot v \cdot n_a$ is the amount of groundwater (in cubic meters per year) that is flowing through the aquifer in a vertical cross section per meter of aquifer length (thickness perpendicular to the cross section). Therefore, if diffusion into the matrix dominates the transport process, fitting of two independent tracer profiles like ^{14}C and ^{36}Cl to the Sudicky model gives an independent and comparably robust estimate of the amount of water flowing in the deeper parts of a thin confined aquifer.

CONTACT US

t 1300 363 400
+61 3 9545 2176
e csiroenquiries@csiro.au
w www.csiro.au

AT CSIRO, WE DO THE EXTRAORDINARY EVERY DAY

We innovate for tomorrow and help improve today – for our customers, all Australians and the world.

Our innovations contribute billions of dollars to the Australian economy every year. As the largest patent holder in the nation, our vast wealth of intellectual property has led to more than 150 spin-off companies.

With more than 5,000 experts and a burning desire to get things done, we are Australia's catalyst for innovation.

CSIRO. WE IMAGINE. WE COLLABORATE. WE INNOVATE.

FOR FURTHER INFORMATION

CSIRO Land and Water
Environmental Tracer Laboratory (ETL)
Dr. Axel Suckow
t +61 8 8303 8744
e **Axel.Suckow**@csiro.au
w www.csiro.au/en/Research/LWF

CSIRO Land and Water
Environmental Tracer Laboratory (ETL)
Dr. Alec Deslandes
t +61 8 8303 8447
e first.last@csiro.au
w www.csiro.au/en/Research/LWF

CSIRO Land and Water
Environmental Tracer Applications (ETA)
Dr. Dirk Mallants
t +61 8 8303 8595
e first.last@csiro.au
w www.csiro.au/en/Research/LWF